

© 2018 Dipobrato Sarbapalli

NUCLEATION SEEDING IN METAKAOLIN GEOPOLYMERS

BY

DIPOBRATO SARBAPALLI

THESIS

Submitted in partial fulfillment of the requirements  
for the degree of Master of Science in Civil Engineering  
in the Graduate College of the  
University of Illinois at Urbana-Champaign, 2018

Urbana, Illinois

Adviser:

Associate Professor Paramita Mondal

## ABSTRACT

Geopolymers are a class of amorphous, aluminosilicate-based binders proposed as an alternative to the cement binders used commonly in the construction industry. One of the main advantages of using geopolymer concrete is the fact that waste materials like fly ash are used as precursors for its production. Therefore, minimal CO<sub>2</sub> emissions (a greenhouse gas) are associated with the preparation of geopolymer precursors. In comparison, cement production is accompanied with CO<sub>2</sub> formation as a by-product, and therefore, geopolymers are believed to be more environment-friendly than cement binders. Despite such benefits, the use of geopolymers in the construction industry is limited due to reasons such as a lack of understanding of geopolymer chemistry. In addition, chemical admixtures used in conventional concrete are not applicable to geopolymers due to differences in chemistry of the two binder materials. Understanding nucleation kinetics in cement binders have led to the development of different admixtures such as accelerators and retarders and it is believed that a clear picture of the nucleation step in geopolymer formation will aid the development of admixtures. Consequently, an increased application of geopolymers in the industry is expected.

Therefore, the objective of this research was to prove and study the nucleation step in metakaolin-sodium hydroxide (MK-NaOH) geopolymer formation. The objective was accomplished by adding silica, titania, synthesized zeolite A and zeolite X nanopowders as external seeds in MK-NaOH geopolymers. Isothermal calorimetry revealed that the addition of these nanoparticles accelerated the rate of heat evolution from metakaolin-sodium hydroxide (MK-NaOH) geopolymers at early age ( $\leq 24\text{h}$ ). This observation provided indirect evidence of a nucleation step existing in geopolymer formation. This hypothesis

was subsequently validated by studying the effects of external seeding on a synthesized aluminosilicate-sodium hydroxide (AlSi-NaOH) geopolymer. Fourier transform infrared spectroscopy (FTIR) revealed that the AlSi-NaOH geopolymer forms two products - one similar to MK-NaOH geopolymer product and the other being a silica rich geopolymer product. Adding zeolite X to the AlSi-NaOH binders promoted formation of the MK-NaOH geopolymer product over the silica-rich geopolymer, which proved that zeolite X serves as a nucleation seed for MK-NaOH binders. External seeding in MK-NaOH geopolymer was observed to decrease porosity at early age ( $\leq 7$ d) and consequently, improvements in compressive strength were noted upto 28d for zeolite X seeded mixes, and upto 70d for  $\text{SiO}_2$  seeded mixes. These observations suggests that external nucleation seeding is a promising method to control and improve the hardened properties of geopolymers.

A secondary objective was to understand the dissolution of aluminosilicates in salicylic acid-methanol (SAM) solution. The SAM dissolution is a selective dissolution technique which has been used previously in our laboratory to remove calcium silicate hydrates from sodium aluminosilicate geopolymer product. This approach was taken while assuming that geopolymer-like aluminosilicates are immune to SAM solution, as stated in literature. However, it was revealed that SAM indeed dissolves sodium aluminosilicates. The mechanism of dissolution was revealed to be an acid attack on the oxygen atom in bridged hydroxyl  $\text{Si}-\text{O}-\text{Al}^-$  groups. The acidity of these groups were observed to be controlled by aluminum in the next nearest neighbor positions, with  $\text{Q}^4(4\text{Al})$  Si associated bridged hydroxyl groups being the least acidic. Therefore, salicylic acid selectively attacks and removes aluminum associated with these sites by forming chelates. Since SAM solution can dissolve aluminosilicates based on their structure, it should be used with caution as a selective dissolution technique.

**Keywords:** Metakaolin-sodium hydroxide, geopolymers, salicylic acid methanol extraction, nucleation seeding, zeolite X, nano-silica

## **ACKNOWLEDGEMENTS**

Three years in graduate school has been a life-changing experience for me. It has helped me grow and develop in ways that I had never imagined. Reaching this stage would not have been possible without the support of many people throughout the journey, and each of them deserves recognition. However, two people are probably the cornerstones of this journey: First, my adviser, Professor Mondal, who has been a strong source of support and has helped me to new heights as a researcher. I would like to thank her for never losing patience during tough times, without which this journey would not have been as enjoyable as it was. Her decision to accept me as her student, given that I was relatively new to the field of cement chemistry and characterization represents a show of tremendous faith, and I will always be grateful for that. I thank her for proofreading this thesis and her suggestions which helped me improve my writing in several places. Second, I would like to thank Dr. Sravanthi Puligilla. She has, and continues to serve as a mentor to me and has taught me the fundamentals of every single thing I know about geopolymers. In addition, she has helped me realize my professional interests, especially in materials characterization. She has inspired me to persevere in research, and to not give up, no matter how frustrating it may get. Without her guidance and advice, this thesis research would not have been possible and neither would I be in the place where I am currently.

I would like to thank Professor Struble for being the instructor for an independent study on Materials Characterization and for being an adviser for the salicylic acid-methanol work performed in this thesis. I have taken back a lot of lessons from her, especially with regards to rigor in research, and the clarity of thought associated with technical writing and oral presentations. While I may not be perfect in these attributes, her advice and suggestions

have only helped me grow further, and has helped me build up an identity as a researcher. Dr. Xu Chen has been an invaluable source of support for my thesis research. His NMR data has helped me build up several conclusions to my work and my discussions with him have usually provided a way out of many research problems. His optimism and cheery attitude has always raised my spirits and I will miss working with him. Professor Walter Klemperer has also provided invaluable support in the SAM research work, and has provided theoretical insights which I could not have obtained with my level of knowledge. I thank him for his patience in hearing out the research problem and for spending several hours while explaining the possible solutions to me.

My sincerest thanks go to Professor Popovics for being an amazing course instructor, and for teaching me the fundamentals of NDT and assisting me with my UWR experiments. The amount of work that he puts into research and courses is clearly visible and that has always motivated me to keep working and pushing my limits. He has been a strong source of support throughout my three years for all questions related to my research and professional career and I will forever miss his advice and his classes.

Special thanks goes to Professor Shoemaker and Ankita Bhutani for their assistance with XRD measurements and Rietveld refinement. Professor Shoemaker's class on microstructure characterization strengthened my knowledge of diffraction beyond expectations, and he has been another source of support in my endeavors to move into contemporary Materials Science research. My decision to apply to Materials Science arises from a single conversation with him, and I would like to thank him for providing much needed, confidence boosting conversations whenever I have been a bit low. I would also like to thank him for his advice on the Ph.D. application process. Ankita has taken out a lot of time from her research and has taught me the ins and outs of TOPAS for Rietveld refinements. I have faced hurdle after hurdle in almost all of my Rietveld refinement calculations, and every single time she has developed a simple and elegant solution towards it. The amount of specialized knowledge that I have obtained from her has been invaluable and I cannot thank

her enough for it.

Bhavesh Shrimali is probably the only person who has been a strong support for my research and professional career and has been a good friend over my stay at Urbana-Champaign. His assistance with my trials on the boundary-nucleation modeling has been invaluable, and I will be grateful forever, for introducing me to L<sup>A</sup>T<sub>E</sub>X. I have always been learning a lot of side coding skills, which has been instrumental in many aspects of research. I also cannot thank him enough for taking out the time to review every single document of my Ph.D. application materials, and for being a strong, constant source of support throughout my journey in graduate school.

Professor Prannoy Suraneni has been an invaluable source of assistance for the micro-reactor research described in this thesis. Without his assistance, fast progress in those experiments would have been impossible, and I thank him for his prompt, continuous support. The experiments in this thesis were carried out in part in the Frederick Seitz Materials Research Laboratory Central Facilities, University of Illinois. I would like to thank MRL staff, especially Natalie, Brad, Dr. Honghui Zhou, Dr. Jade Wang, Dr. Lou Ann Miller, Dr. Mauro Sardela for their support, advice, and training on MRL instruments. I thank Dr. Shaoying Qi of CEE for his assistance with the nitrogen adsorption-desorption measurements and for providing access to 4<sup>th</sup> floor labs. I thank Professor Jeremy Guest for letting me use the probe sonicator in his laboratory. Professor Lange's support through CEE401 Teaching Assistantship is much appreciated. I thank Dr. Leilei Yin at Beckman for a  $\mu$ CT measurement. I would like to thank Dr. David Farrow for his support while serving as a TA for CEE300. I thank Morgan King for supporting my work as an undergraduate; her experimental results directed me into the work presented in this thesis.

The administrative staff at CEE have always provided me with excellent support to all my questions and requirements, and I would like to thank Sue Lowry and Joan Christian for their support. Sue has been invaluable in helping me procure all the materials related to my thesis research. Joan has always provided prompt answers to all graduate program

related queries and has helped me manage all administrative matters related to my graduate program. I also thank her for checking the thesis format on a short notice.

I would like to thank Deutscher Akademischer Austauschdienst (DAAD) for providing me with a Fellowship to intern with BASF Chemicals in Germany. The experience gained has helped me identify my professional interests, and has given an unparalleled experience in Materials Science research. I would like to thank Annkristin Ermel for her continuous support throughout the duration of the fellowship. Dr. Tobias Umbach, Dr. Matthias Kellermeier, and Dr. Stephan Becker have encouraged me to make the transition to Materials Science and have provided valuable exposure into the life as a scientist in the industry. I would like to acknowledge Herr Bernd Kümmerling and Frau Elizabeth Wagner for their assistance and training on Atomic Force Microscopes. I would like to thank Lukas Römmeling for his friendship and company, which made my stay in Germany an amazing experience.

I would like to thank the students in UIUC's construction materials group, Will, Palash, Robbie, Ardavan, Bartik, James, Yu, Homin, Sai, Chi-Luen for their friendship and assistance with lab experiments and materials. I thank Palash, Ivana, Shailee, Kamalendu, Nikhil, Chinmayee, Gaurav, Richa, Karthik, Gowthami, Sulagna, Olivier, and Tristan for their friendship which has provided a much-needed balance in my life. My friends from Calcutta and over my undergraduate years: Shiladitya, Sabyasachi, Aslam, Aditya, Bharadwaj, Sidchan, Madhurima, Taurja, and Parikshit, I thank you all for your continuous support and friendship over the years. It has always provided an outlet to vent all the frustration and ease the rigors of graduate life. Special thanks are reserved for Kate for helping me become familiar with the American lifestyle (and cooking), Abhishek for being an extremely reliable friend (and companion for eating food), and Oola for being the most amazing roommate that one can ask for. The time spent with you all will remain an unforgettable phase in my life.

I would like to thank Professor Bishwajit Bhattacharjee and Professor Kaustav Sarkar for being a strong influence in my decision to pursue cement chemistry research. The

knowledge they imparted went a long way in helping me adjust to new avenues of research. My teachers from childhood, Anirban Sir, and Subhashish Sir have provided me a strong base due to which I have never had problems in taking a jump into unknowns within academia. Their mentorship has made me into who I am today.

I would like to thank Shradha for being the sweetest and the most caring girlfriend anyone can ask for. Her support over the past year has been priceless and I am amazed that I found such a beautiful person to share my life with. She makes life wonderful with her cheer and support, and I am really excited about the future that lies in store for us. I also thank her for proof-reading several portions of this thesis. My family, especially my mother and elder brother are equally amazing and have made my life extremely easy with their countless untold sacrifices. Without their love and support, I would not have been able to focus on the harsh, demanding lifestyle of graduate school. I thank them from the bottom of my heart for being this amazing and I count myself to be extremely lucky to have such a supportive family and friends.

As a final note, I would like to thank the National Science Foundation and the Department of Civil and Environmental Engineering, University of Illinois, who have provided financial support throughout my Masters in form of assistantships. Also, I would like to thank Professor Joaquín Rodríguez López for agreeing to be my Ph.D. adviser. His decision removed the stress and uncertainty accumulated over two years, and I look forward to my time working with him.

# TABLE OF CONTENTS

<b>Chapter 1 Introduction . . . . .</b>	<b>1</b>
1.1 Objectives . . . . .	2
1.2 Motivation . . . . .	4
1.3 Organization of thesis . . . . .	5
1.4 Terminology . . . . .	6
<b>Chapter 2 Literature Review . . . . .</b>	<b>8</b>
2.1 Silica polymerization and growth . . . . .	9
2.2 Mechanism of metakaolin geopolymers formation . . . . .	13
2.3 Kinetics of metakaolin geopolymers . . . . .	16
2.4 Role of silica and alumina species in geopolymers . . . . .	22
2.5 Nucleation seeding in cement binders . . . . .	26
2.6 Nucleation seeding in geopolymers . . . . .	29
2.7 Conclusions . . . . .	33
<b>Chapter 3 Synthesis and characterization of seeding agents . . . . .</b>	<b>35</b>
3.1 Introduction . . . . .	35
3.2 Commercial nanopowders . . . . .	35
3.3 Synthesis of nano-zeolite X and A . . . . .	36
3.4 Characterization . . . . .	38
3.5 Results . . . . .	40
<b>Chapter 4 Identifying nucleation seeds . . . . .</b>	<b>54</b>
4.1 Introduction . . . . .	54
4.2 Experimental Methods . . . . .	56
4.3 Results and Discussion . . . . .	59
4.4 Conclusions . . . . .	73
<b>Chapter 5 Proof of external nucleation seeding . . . . .</b>	<b>76</b>
5.1 Introduction . . . . .	76
5.2 Synthesis of aluminosilicate precursor . . . . .	77
5.3 Experimental methods . . . . .	78
5.4 Characterization of synthesized aluminosilicate . . . . .	79
5.5 AlSi-NaOH geopolymers: Results and Discussion . . . . .	83
5.6 Conclusions . . . . .	89

<b>Chapter 6</b>	<b>Consequences of external seeding . . . . .</b>	<b>91</b>
6.1	Introduction . . . . .	91
6.2	Materials and methods . . . . .	93
6.3	Results and Discussion . . . . .	99
6.4	Conclusions . . . . .	107
<b>Chapter 7</b>	<b>Salicylic acid extraction of aluminosilicates . . . . .</b>	<b>109</b>
7.1	Introduction . . . . .	109
7.2	Experimental Methods . . . . .	111
7.3	Results . . . . .	113
7.4	Summary and Discussion . . . . .	123
7.5	Conclusions . . . . .	127
<b>Chapter 8</b>	<b>Summary and Conclusions . . . . .</b>	<b>129</b>
<b>Appendix A</b>	<b>Micro-reactors in synthesized aluminosilicate . . . . .</b>	<b>133</b>
<b>Appendix B</b>	<b>Rietveld refinement procedures . . . . .</b>	<b>140</b>
<b>Appendix C</b>	<b>Alternate porosity measurements . . . . .</b>	<b>143</b>
<b>Appendix D</b>	<b>Ultrasonic wave reflection measurements . . . . .</b>	<b>146</b>
<b>Appendix E</b>	<b>Research Output . . . . .</b>	<b>151</b>
<b>References</b>		<b>152</b>

# Chapter 1

## Introduction

Geopolymers, a subset of alkali-activated binders, are typically defined as x-ray amorphous aluminosilicates containing little or no calcium [1]. These binders are typically obtained by alkali hydroxide or alkali silicate activation of powdered aluminosilicates such as Class F (low calcium) fly ash and metakaolin (obtained by calcining kaolinite clay, typically a pure aluminosilicate material) [1]. Of late, alkali-activated binders have received a lot of attention from the research community, and the driver behind such interests is primarily centered around the fact that the cement industry generates carbon dioxide as byproducts during portland cement production [2]. The problem is exacerbated due to the massive amounts of cement produced in the world, leading to concrete being ranked as the second most consumed commodity, only after water [3].

Other drivers for research on alternative binder include different environmental factors such as natural resource depletion (natural minerals such as limestone and clay are required for cement production [4]). Such issues are observed especially in small developing countries with high cement consumption. Likewise, rising costs associated with CO<sub>2</sub> release by industries are imposing economic drivers to establish alkali-activated binder technology.[2] In addition, attempts to reduce cement consumption through replacement of cement with supplementary cementitious materials (SCM) may not be a feasible solution for the long run. Macphee et al., [5] have predicted that if the cement industry wants to reduce the CO<sub>2</sub> emissions to 1990 global levels, concrete production will require a disproportionately high proportion of SCM over cement (Figure 1.1). Thus, there will not be enough cement to activate SCM's and therefore, the use of low CO<sub>2</sub> alternative binders are of paramount importance.

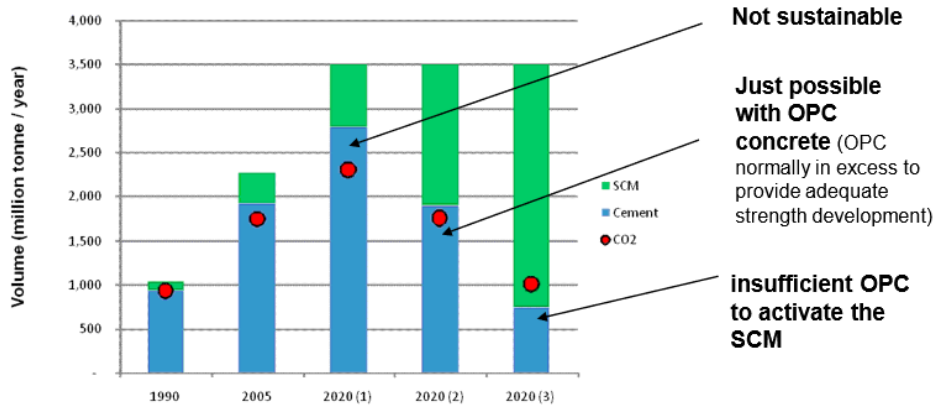


Figure 1.1: CO<sub>2</sub> emissions as a function of SCM and Cement requirements predicted for 2020 while (1) continuing construction trends, (2) allowing for enough SCM to activate all cement, (3) bringing CO<sub>2</sub> levels back to 1990 (adapted from [5])

Similarly, technical studies in alkali-activated binder technology have demonstrated that this class of materials can favorably compete with, and exceed the performance of Portland cement concrete in many scenarios (such studies have been reviewed in [6, 7]). Additional factors in the motivation behind geopolymers research have been well summarized by Provis et al. [2]. Owing to such drivers, there has been a significant development in geopolymers technology, as reported from multiple reviews on the subject over time [8–10].

## 1.1 Objectives

The primary objective of this thesis is the experimental characterization of a hypothesized nucleation step in low calcium alkali-activated binders (geopolymers). Realizing this objective would contribute towards understanding the specific mechanisms controlling the rate of geopolymers product formation. An external nucleation seeding approach similar to the work by Puligilla [11] on potassium hydroxide and silicate activated Class F fly ash-slag, was utilized to meet the objective.

Descriptions that exist on the nucleation process mainly identify inert nanomaterials such as Al<sub>2</sub>O<sub>3</sub>, ZnO, ZrO<sub>2</sub> as a site on which geopolymers products can form [12, 13]. However,

no clear description exists on the nuclei which cause the growth of geopolymer products in un-seeded samples. For example, in tricalcium silicate ( $C_3S$ ) hydration, it has been proven experimentally that calcium-silicate-hydrate (C-S-H) nuclei need to form for the growth of C-S-H gel [14]. Therefore, the hydration reaction of cement is an autocatalytic process.

Literature reveals that the growth of geopolymer product is also believed to be autocatalytic [15, 16]. Rahier et al., [15] conducted experiments using Modulated differential scanning calorimetry (MDSC) and Dynamic mechanical analysis (DMA) and observed the reaction rate to increase after the geopolymer pastes started gaining stiffness (higher elastic modulus values). An increase in the elastic modulus of the geopolymer paste implies that the liquid phase is solidifying and porosity is decreasing. Therefore, as the porosity keeps on decreasing it is expected that the species dissolved from metakaolin will face hindrance to mass transport within the microstructure. Consequently, the reaction rate is expected to decrease. On the contrary, the reaction rate was observed to increase, and therefore, an autocatalytic growth mechanism was believed to be a part of geopolymerization.

In another study by Provis and van Deventer, a numerical model containing an autocatalytic step was used to describe geopolymerization kinetics. A successful fit of their model to geopolymerization kinetics data provides additional evidence of the presence of such a step in the geopolymer reaction mechanism. Both these studies are discussed in detail, within Chapter 2 of this thesis. However, it should be noted that a strong evidence for an autocatalytic step would be to use the reaction products obtained from geopolymers as a seed, in the same way as Thomas et al. have demonstrated in their study [14] on  $C_3S$  hydration.

Therefore, for the first time, nucleation seeds based on reaction products have been used in geopolymers (low calcium alkali-activated binders). The geopolymer binder used for this study was prepared with metakaolin and sodium hydroxide. While low-calcium geopolymers can be obtained from Class F Fly Ash, metakaolin was chosen for this study since this yields a geopolymer free of impurities. Metakaolin-alkali hydroxide/silicate

geopolymers are therefore regarded as one of the simplest chemical systems [17], within the vast domain of alkali-activated binders. The purity of metakaolin also ensures that results from characterization techniques can be interpreted relatively easily and any impact of external nucleation seeds on geopolymers should be evident.

For this study, three types of seeding agents were used: product based, reactant based and inert seeds. The product based seeds were synthesized zeolites A and X nanopowders, both of which have been observed to form in the aged metakaolin-sodium hydroxide geopolymers prepared in this study. Commercial silicon and aluminum oxide nanoparticles were also used, since silica and alumina species are known reactants in geopolymer formation. High surface area titanium oxide (obtained commercially) falls in the category of an inert seed, as observed from the study by Jayapalan et al. [18]

## 1.2 Motivation

The use of product and reactant based seeds provides an opportunity to obtain a better understanding of any nucleation step in geopolymer formation. As mentioned earlier, such an understanding will add to the current knowledge on geopolymer reaction mechanism; and this serves as the prime motivation behind this study. Experimental evidence exists in literature confirming the presence of a nucleation step in geopolymer formation [12, 13], but only Rees et al., has provided a complete experimental picture of the nucleation step existing in geopolymers.

The external seeding approach has also been utilized by Puligilla in medium calcium, fly ash-slag binders, to explain the effects of silicates in activator solution [11]. While the effects of silica species in activator solution have been well studied [19–22]), there is a lack of understanding as to why these effects are taking place. Therefore, the external seeding approach used in this study, has the potential to shed new insight about such factors.

User-friendly, practical alkali-activated binders (for large scale field applications)

involve a precursor based on a combination of class F fly ash and slag [11]. The presence of slag along with fly ash leads to higher development rates [23], and these binders have been well studied [11, 24]. Reaction products of these user-friendly binders are known to be a combination of both calcium silicate/calcium aluminate hydrates ( $\text{C-S-H}/\text{C-A-S-H}$ )<sup>1</sup> and sodium/potassium aluminosilicate hydrates ( $\text{N/K-A-S-H}$ ) [24, 25]. Given the fact that low calcium three-dimensional aluminosilicate gels exist in user friendly binder systems [26] any improvement in the understanding of geopolymer mechanisms would enable further advancements in sub-domains such as admixture design, all of which plays a role in bringing these alternative binders into practice.

### 1.3 Organization of thesis

The literature reviewed in this thesis (Chapter 2) centers on reaction mechanisms in geopolymers. Specifically, articles describing the role of silica and alumina in geopolymerization have been reviewed. Information about nucleation seeding in geopolymers have been critically reviewed. Data on geopolymerization kinetics as measured through techniques such as isothermal calorimetry have been included in this chapter. To understand and explain the consequences of nucleation seeding in binders, external nucleation seeding in cement binders have been reviewed as well.

Chapter 3 focuses on synthesis and characterization of zeolite nanopowders through techniques such as x-ray diffraction, rietveld refinement, nuclear magnetic resonance, x-ray fluorescence and infrared spectroscopy. Other nanopowders, procured commercially, were characterized as well. Materials and methods are reiterated for every chapter to aid the reader. Synthesis procedure and subsequent characterization of a powdered aluminosilicate similar to metakaolin has been described as well. The material was used as a precursor to the geopolymers synthesized in Chapter 6.

---

<sup>1</sup>Cement chemistry notation is used in this thesis;  $\text{CaO} \equiv \text{C}$ ,  $\text{A} \equiv \text{Al}_2\text{O}_3$ ,  $\text{S} \equiv \text{SiO}_2$ ,  $\text{H} \equiv \text{H}_2\text{O}$ ,  $\text{N} \equiv \text{Na}_2\text{O}$ ,  $\text{K} \equiv \text{K}_2\text{O}$

Chapter 4 deals with identifying nucleation seeds for the metakaolin-sodium hydroxide geopolymer. Calorimetry data is presented, and percentages of unreacted metakaolin was obtained through HCl dissolution for different ages. This chapter utilizes all three types of seeds (product based, reactant based, and inert), in an attempt to evaluate their potential as seeding agents for geopolymers. Subsequently, two seeds, zeolite X and nanosilica are chosen for further study.

Chapter 6 characterizes the consequences of nucleation on kinetics through numerical models on the calorimetry data obtained in Chapter 4. Backscattered electron microscopy data is used to quantify porosity in the metakaolin geopolymer samples at 1d and 7d. Compressive strength measurements have been presented for ages up to 70d, to characterize any effect of nucleation seeds. X-ray diffraction data is shown (at 28d, 56d and 70d), which illustrates the effects of seed on zeolite crystallization observed in the metakaolin-sodium hydroxide geopolymers.

While working on characterizing the geopolymer through selective dissolution studies performed previously at our laboratory by Puligilla et al. [26], it was discovered that the salicylic acid-methanol (SAM) dissolution technique affects sodium aluminosilicate geopolymers, whereas literature reports that SAM solution does not affect aluminosilicates. Chapter 7 describes the work done to understand the dissolution mechanism of amorphous and crystalline sodium aluminosilicates in SAM solution.

Chapter 8 sums up the conclusions obtained from this study. Appendices are provided which describes other experimental attempts in investigating the metakaolin-sodium hydroxide geopolymerization.

## 1.4 Terminology

Literature has abundant references to alkali-activated binders, with commonly used terminologies such as inorganic polymers, alkali-activated binders and geopolymers [27]. As

mentioned by Provis [27], such wide variations in terminology creates ambiguity in the minds of new researchers. In addition, key findings related to the study do not come out of a simple keyword search on search engines. Therefore, the terminologies used to describe the binder system, have been chosen carefully. For example, metakaolin-sodium hydroxide binders are used as a description, instead of alkali-activated metakaolin. In addition, the term “geopolymer(s)” are used to refer to low Ca binder systems, which are considered to be a subset to alkali-activated binders, as shown in Figure 1.2. The metakaolin-sodium hydroxide binder utilized in this study, is therefore, described as a geopolymer as and when required.

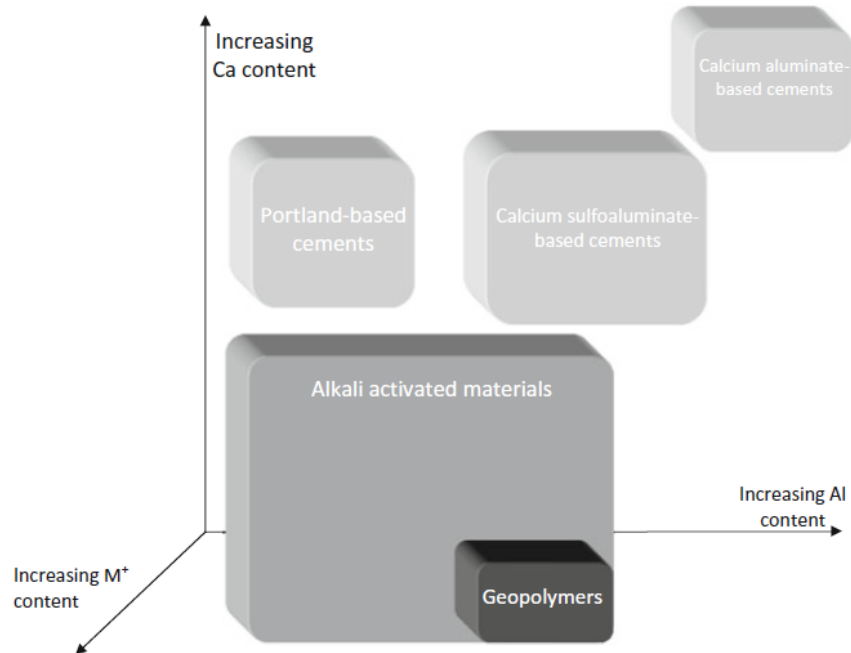


Figure 1.2: Classification of alkali-activated binders, with increasing gray value denoting increasing M<sup>+</sup> content (adapted from [27])

# Chapter 2

## Literature Review

There is no paucity of information with regards to geopolymers mechanisms in literature, and it is not possible to review everything in detail. Therefore, this review only provides a brief description of the main processes in geopolymers formation, which are considered to be dissolution and polycondensation [8, 16, 28, 29]. Topics such as silica polymerization have been used to interpret the results obtained in this study, and therefore, they are described in this chapter. A brief review of nucleation seeding in cement binders is included to understand the consequences of external seeding in binder materials.

While alkali-activated binder technology has been established from the 1940's (as reviewed by Roy [30]), the use of metakaolin as a precursor for alkali-activated binder has been described by the French scientist Joseph Davidovits within a US Patent [31] in 1982. Subsequently, further research has been carried out on the structure-property relations in metakaolin geopolymers by Rahier et al., [15, 32–34]. Basic findings that are well known to the research community have been described in these articles. It was established that the geopolymers reaction between metakaolin and alkali-silicate solutions is exothermic through DSC (Differential Scanning Calorimetry). NMR (Nuclear Magnetic Resonance) spectroscopy demonstrated that the aluminum and silicon were present in tetrahedral coordination within the alkali-activated binder. XRD (X-Ray Diffraction) revealed that the aluminosilicate formed was amorphous.

Currently, there are multiple descriptions of mechanisms involved in geopolymers [8, 12, 16]. A summary of the overall processes (Figure 2.1) for silicate-activated metakaolin has been recently proposed by Chen et al., [28] based on NMR (Nuclear Magnetic Resonance spectroscopy) studies. The model highlighted in Figure 2.1 is

based on the mechanism described by Duxson et al. [8]

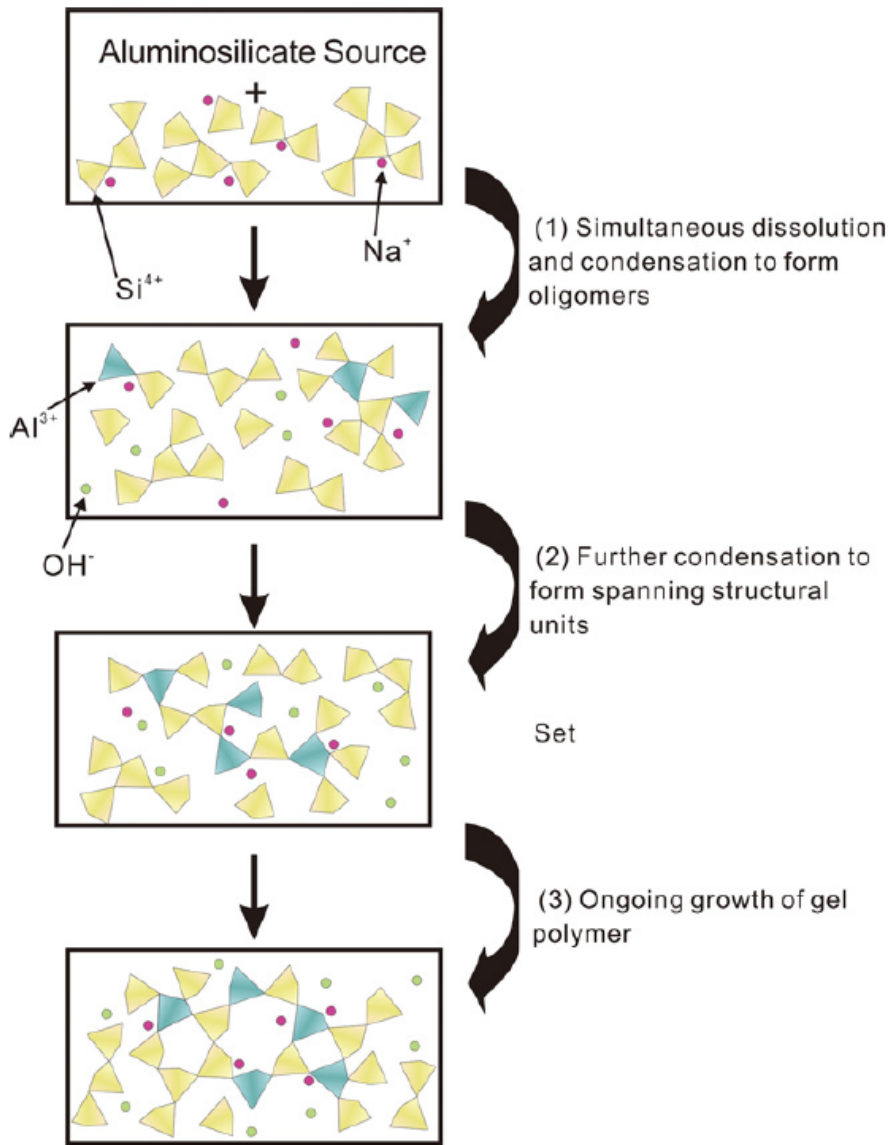


Figure 2.1: Mechanism of metakaolin geopolymization, adapted from [28]

## 2.1 Silica polymerization and growth

Before delving into geopolymers mechanisms, a brief review is presented on silica polymerization and distribution of silicate species in alkaline solutions. A detailed description of silica polymerization presented by Iler [35] is reviewed here. In alkaline aqueous solutions,

dissolved monomeric silica species polymerizes to a gel in a three step process, with monosilicic acid ( $\text{Si(OH)}_4$ ) initially condensing to form colloidal particles (1 $\mu\text{m}$  to 1nm in size [36]). Subsequently, these particles grow and form three-dimensional silica gel networks or large sols. The process is described in the following steps [35], and is summed up in Figure 2.2.

- Upon exceeding solubility limit of silica in solution (100-200ppm), monosilicic acid condenses in the absence of solid phase (solid phases can lead to silica precipitation) to form dimers and oligomers.
- Silicic acid polymerizes to form a maximum of siloxane bonds ( $\text{Si}-\text{O}-\text{Si}$ ) over terminal silanol bonds ( $\text{Si}-\text{OH}$ ). This preference leads to the formation of cyclic spherical species, which serve as nuclei for gel growth.
- The smaller cyclic silica species are more soluble than their larger counterparts. Hence the smaller species preferentially dissolve in solution, and deposit on the larger silica species (Ostwald Ripening). Therefore, the average size of particles increases with time, and large sols are formed. Once the average particle size exceeds 5-10nm (for solutions with  $\text{pH} > 7$ ), the growth of silica sols slow down because the sols exceeding this size range dissolve slowly.
- Since silica particles are negatively charged in basic media, they do not agglomerate. The presence of a salt can neutralize the surface charge, causing aggregation and three-dimensional network formation, as shown in Figure 2.2.

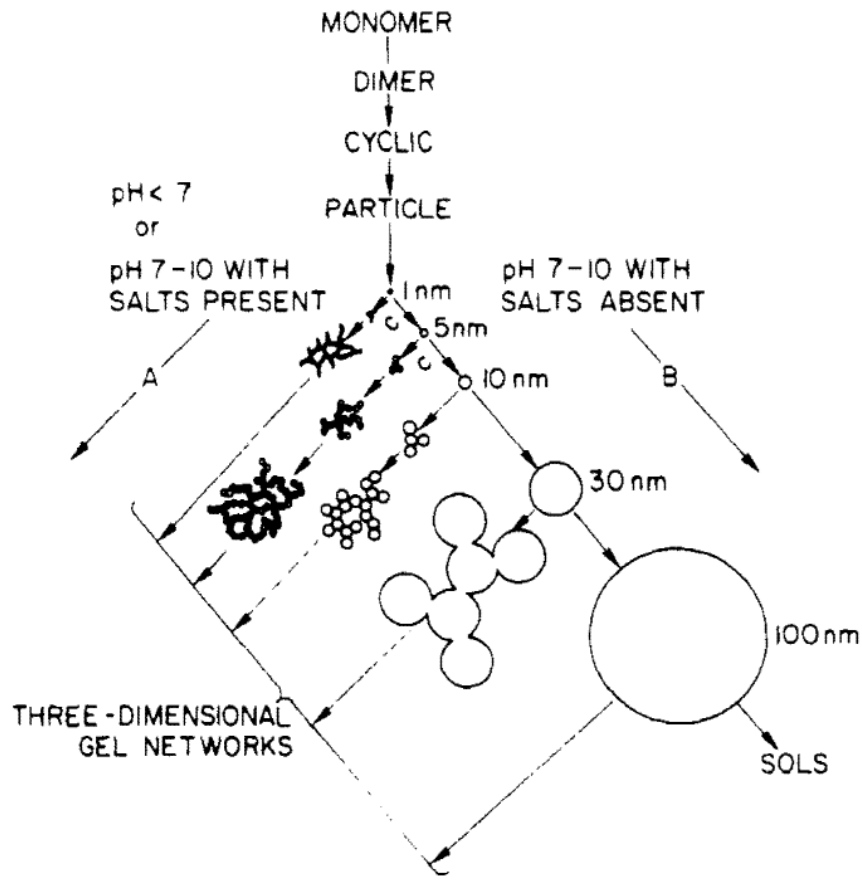


Figure 2.2: Mechanism of silica polymerization and gelling, adapted from [35]

### 2.1.1 Silicate speciation in alkaline media

Metakaolin geopolymers can be achieved through a hydroxide-activated or silicate-activated route [1]. For silicate-activated geopolymers, it is necessary to obtain an understanding of silicate species in solution since it has a key impact on geopolymers, as discussed in subsequent sections. To describe polymerization of silicate species, Engelhardt's Q notation is used throughout this thesis, wherein a  $Q^n$  silicon center means that it is connected to "n" silicon atoms through oxygen linkages ( $4 \geq n \geq 0$ ) [37].  $Q^n(mAl)$  is used to denote aluminum substitution, wherein m denotes the number of silicon sites substituted by aluminum ( $4 \geq n \geq m < 0$ ) [37]. It should be noted that aluminum exists primarily in tetrahedrally coordinated  $Al(OH)_4^-$  at high pH values [29, 38] (solutions with  $pH > 12$  are

typical in geopolymmerization).

Compositions of any silicate solution can be described through the stoichiometry notation  $\text{Na}_2\text{O} : \text{xSiO}_2 : \text{yH}_2\text{O}$ .  $x$  is termed as the silicate modulus, and  $y$  controls the pH of the solution, and both of these parameters control the speciation of silica species in aqueous solutions. With decreasing silicate modulus (and constant pH), the polymerization of silica reduces, which means that silicon centers are found with lower Q numbers. In addition, with increase in pH (constant silica modulus), silica is depolymerized and found with lower Q numbers [38, 39]. Provis et al., [40] has provided a detailed account of Na and K-silicate species in aqueous solutions through NMR experiments and modeling work. NMR spectra of K-silicate solutions with a stoichiometry of 1:x:11 is shown in Figure 2.3a. The distribution of silica centers in Na-silicates with changing modulus (while  $\text{H}_2\text{O}/\text{Na}_2\text{O} = 11$ ) is shown in Figure 2.3b.

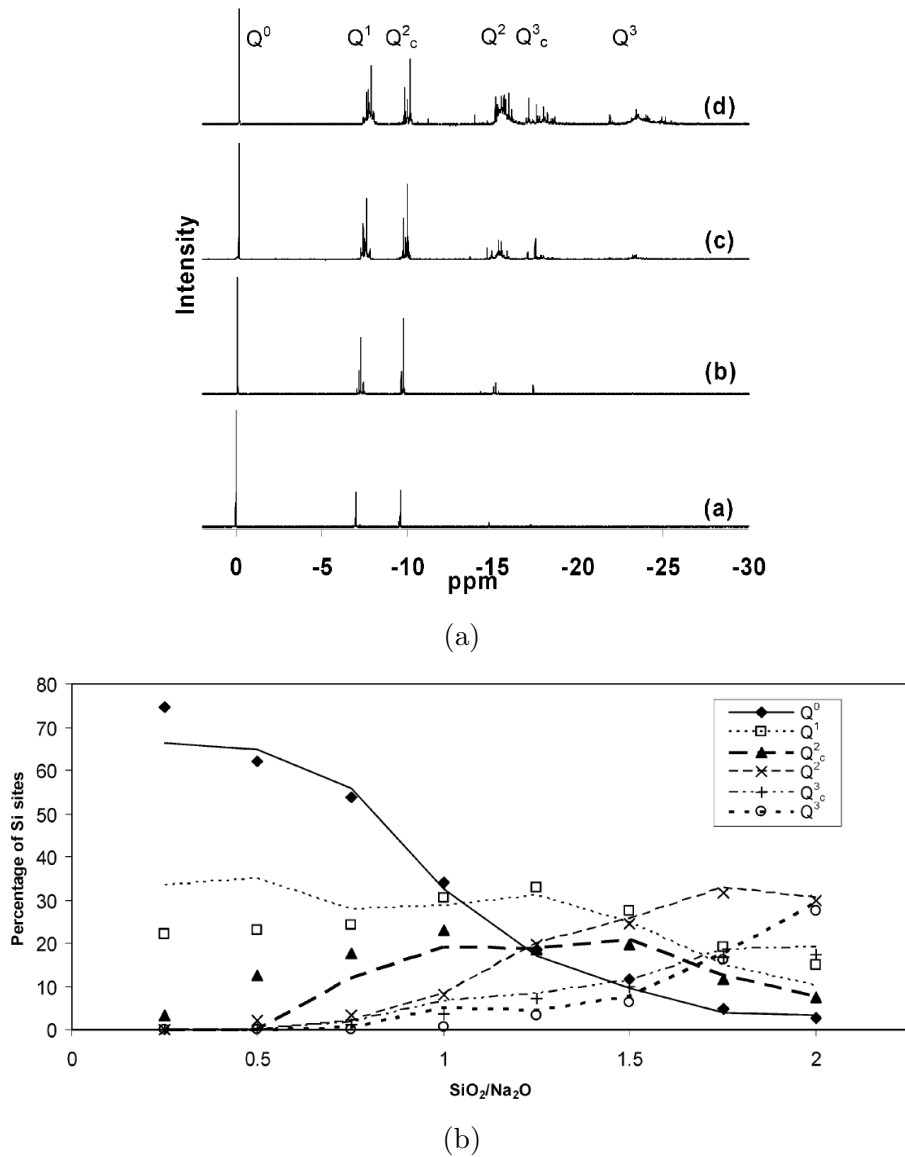


Figure 2.3: Silica species in aqueous silicates (a) NMR spectra for K-silicates; (b) Silicate speciation in Na-silicates

## 2.2 Mechanism of metakaolin geopolymers formation

As mentioned earlier, the mechanism of metakaolin geopolymers consists of two major processes (which occur concurrently) - dissolution and polycondensation (polymerization). The dissolution step has been identified through analogies to dissolution of aluminosilicate precursors in zeolite synthesis. Fly ash dissolves in alkaline solutions to yield

zeolite products, which means that three-dimensional aluminosilicate networks can arise out of a dissolution process [41, 42]. The mechanism behind dissolution of such materials has also been studied extensively [41]. Duxson et al., [8] derived additional evidence of a dissolution step drawing analogies to dissolution steps in aluminosilicate weathering. These observations provide strong evidence that a dissolution step is involved in the mechanism of geopolymers formation.

Experimental evidence in geopolymers has been obtained from the DSC studies by Rahier et al., [15]. It was observed initial rates of reaction (upto  $\approx$ 25 min) to increase in metakaolin-sodium silicate geopolymers, when the surface area of metakaolin precursor increases. This dependence of reaction kinetics on the surface area indicates that reactions take place on the surface of the metakaolin, and proves the involvement of a dissolution step in geopolimerization mechanisms. Other studies have also demonstrated the dissolution of metakaolin and class F fly ash in alkaline media through leaching studies and SEM (Scanning Electron Microscopy) [29, 43–45]. These studies have established that an increase in alkalinity of activator solution accelerates the dissolution rate of aluminosilicate precursor.

Silicate and aluminate species in alkaline solution are well known to polymerize and form amorphous aluminosilicate gels [38, 46]. Such gels are often precursors to the hydrothermal synthesis of zeolites (crystalline aluminosilicates) [38]. The polymerization step was validated through solid state  $^{29}\text{Si}$  NMR studies on metakaolin geopolymers [32, 47], which showed the presence of three-dimensional Q<sup>4</sup> silicon sites in hardened geopolymers pastes. Recent ex-situ NMR data by Chen et al. [28] shows a clear picture of dissolution and polymerization step in metakaolin-sodium silicate geopolymers. Conclusions from such NMR data can also be supported through alternative experimental studies utilizing in-situ ATR-FTIR [12, 13].

A mechanistic model was subsequently proposed for geopolymers (Figure 2.4), based off Faimon's model [48] for weathering of aluminosilicates [16]. Faimon's model involves identifying reservoirs of species and the fluxes between the reservoirs, with the assumption

being that flux of matter out of a reservoir is a function (linear/non-linear) of the quantity of matter present in the reservoir. This approach was deemed to be suitable when considering complex chemical processes, as seen in the case of aluminosilicate weathering which consists of dissolution-polycondensation steps similar to geopolymers [48]. Another reason for choosing the Faimon model to simulate geopolymers kinetics was the presence of an autocatalytic step, when aluminosilicate oligomers condense to an amorphous polymer [16]. Such an autocatalytic step is also believed to exist in the metakaolin geopolymers process [15], during polycondensation of silicate and aluminate species. Provis and Deventer altered Faimon's model to accommodate geopolymers precursors such as fly ash and metakaolin and considered a higher solution pH in the dissolution of precursors, compared to the solutions used to study aluminosilicate weathering. A decent fit of the model to the kinetic data generated through EDXRD [49] demonstrated the suitability of the model in predicting geopolymers kinetics (Figure 2.5).

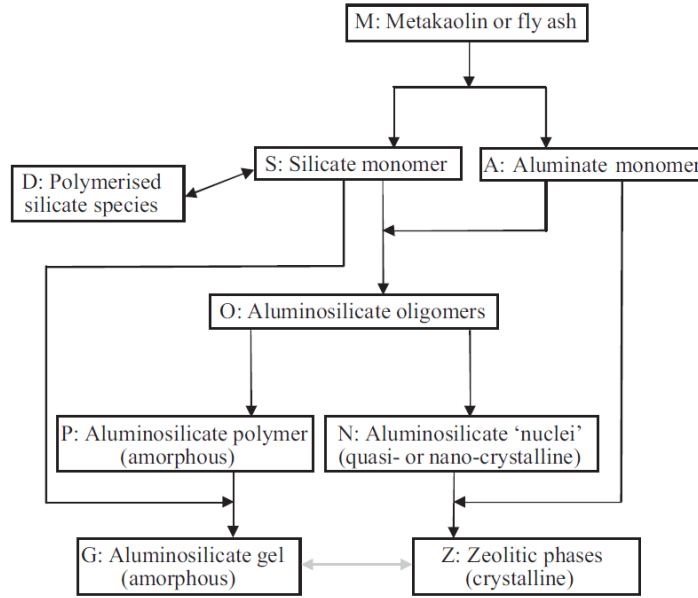


Figure 2.4: Proposed geopolymization mechanism, modified from Faimon [48], adapted from [16]

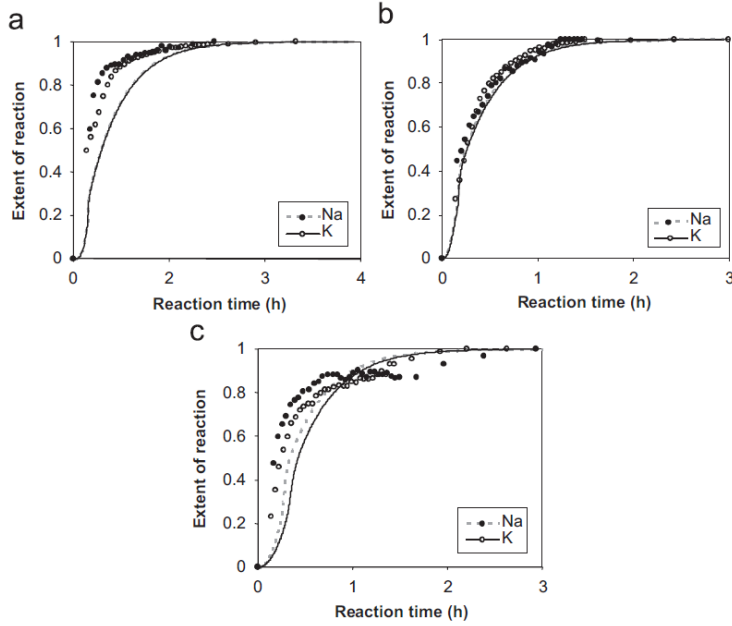


Figure 2.5: Modified Faimon model fits on EDXRD reaction extent data, for metakaolin geopolymers with (a)  $\text{Si}/\text{Al} = 1$ , (b)  $\text{Si}/\text{Al} = 1.5$  and (c)  $\text{Si}/\text{Al} = 2$ , adapted from [16, 49]

## 2.3 Kinetics of metakaolin geopolymORIZATION

### 2.3.1 Isothermal and differential scanning calorimetry

Calorimetry techniques have been widely used to quantify reaction kinetics in metakaolin geopolymers [15, 32, 34, 50–53] since the dissolution and polymerization reaction have been observed to be exothermic [32, 53]. Studies by Rahier et al. [15] used MDSC (Modulated Differential Scanning Calorimetry) and DMA (Dynamic Mechanical Analyzer) simultaneously to correlate changing mechanical properties to chemical reaction rate. Figure 2.6 shows the correlation between storage modulus, and heat released during geopolymORIZATION. Setting was characterized by the term “vitrification” which refers to the start of solid network formation in the geopolymer pastes. The initial rapid reaction rate (before onset of vitrification) was interpreted as heat released due to metakaolin dissolution [15]. The peak heat evolution after onset of vitrification was described to be arising from the polymerization of aluminosilicate species [15, 33].

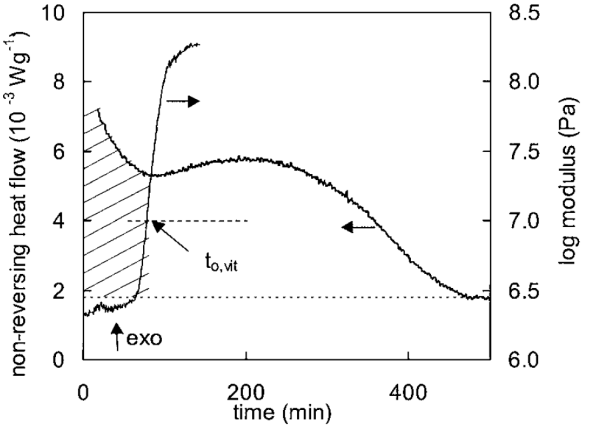


Figure 2.6: Correlation between rate of heat evolution vs. storage modulus at 35°C in sodium silicate-activated metakaolin geopolymers (adapted from [15]).  $t_{0,vit}$  denotes the onset of vitrification, characterized by increasing modulus

Since then, multiple studies have confirmed that isothermal rate of heat evolution in metakaolin geopolymers possess atleast two peak values, correlating to dissolution and polymerization respectively.  $^{29}\text{Si}$ -NMR measurements of T2 relaxation (or spin-spin relaxation) time in sodium hydroxide-metakaolin geopolymers have shown that the values decrease drastically till  $\approx 1$  hr and then increase with time [29]. This result was interpreted qualitatively in terms of changes in free water content. A higher free water content would enable the molecules to have a lower relaxation time. Therefore, the decrease in water content proves that dissolution process is dominating, followed by polycondensation, which releases free water. This observation has also been validated in silicate activated metakaolin, through EPR (Electron Paramagnetic Resonance) spectroscopy [54]. Based on such experimental evidence and the numerical model presented in Section 2.2, the different steps of metakaolin geopolymers have been described in on the basis of rate of heat evolution in isothermal calorimetry, as shown in Figure 2.7. The assignment of unique regions in Figure 2.7 to dissolution and polymerization does not imply that the processes occur separately; the processes dominating within the geopolymerization reaction are marked in the respective stages I, II and III. Dissolution and polymerization are known to occur simultaneously in geopolymers.

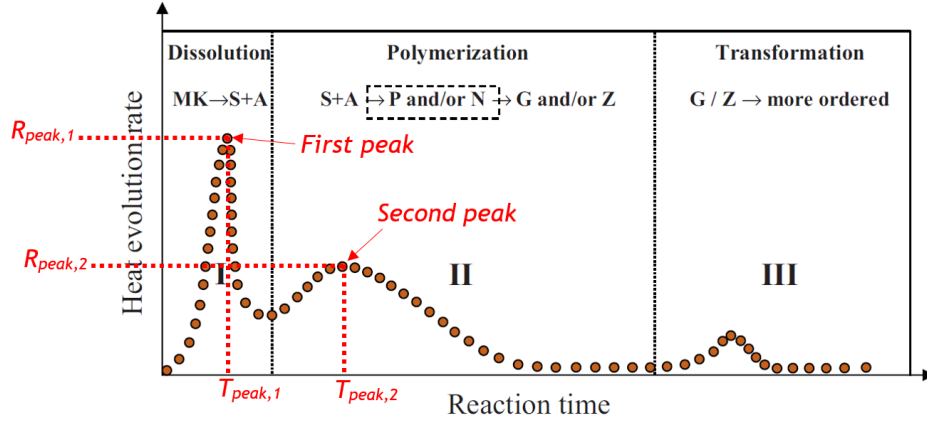


Figure 2.7: Different stages of geopolymers in metakaolin-sodium hydroxide geopolymers (adapted from [50]). References to notations used in the figure are derived from Figure 2.4. The additional notations  $R_{peak,1}$ ,  $R_{peak,2}$ ,  $T_{peak,1}$ ,  $T_{peak,2}$  will be used to describe changes to rate of heat evolution upon the addition of seeds in the remainder of this thesis

### 2.3.2 Energy Dispersive X-Ray Diffraction (EDXRD)

Provis and van Deventer [49] have studied the early age reaction (till  $\approx 3\text{h}$ ) in metakaolin geopolymers with varying Si/Al ratios through synchrotron EDXRD (Energy Dispersive X-Ray Diffraction). The reaction progress was quantified with the EDXRD spectra taken at the beginning and end of the test run. A reaction extent parameter was defined ( $x$ ) assuming that each spectrum can be obtained through a linear interpolation of the first and last spectra, using Eq. 2.1. The estimation of the reaction parameter is shown through Figure 2.8, and the temporal resolution obtained from this analysis allows for plotting reaction extent against time, shown in Figure 2.9.

The results from this study demonstrated that increasing the Si/Al ratio in the geopolymers decrease the extent of reaction. The study hypothesized that pastes with high Si/Al ratio solidify, therefore reducing the mobility of dissolved species in solution. Subsequently, a reduced rate of reaction is observed. However, it should be noted that the study provides no quantification of the “solidification” that has occurred in the binder. It should be noted that a major drawback of the EDXRD analysis is the fact that reaction

extent has been quantified relative to the final EDXRD pattern (taken at around 3 hours, as shown in Figure 2.8a). Therefore, it any changes in kinetics post  $\approx 3\text{h}$  cannot be observed or inferred from this study.

$$\text{Spectrum}(t) = (x)(\text{final spectrum}) + (1 - x)(\text{initial spectrum}) \quad (2.1)$$

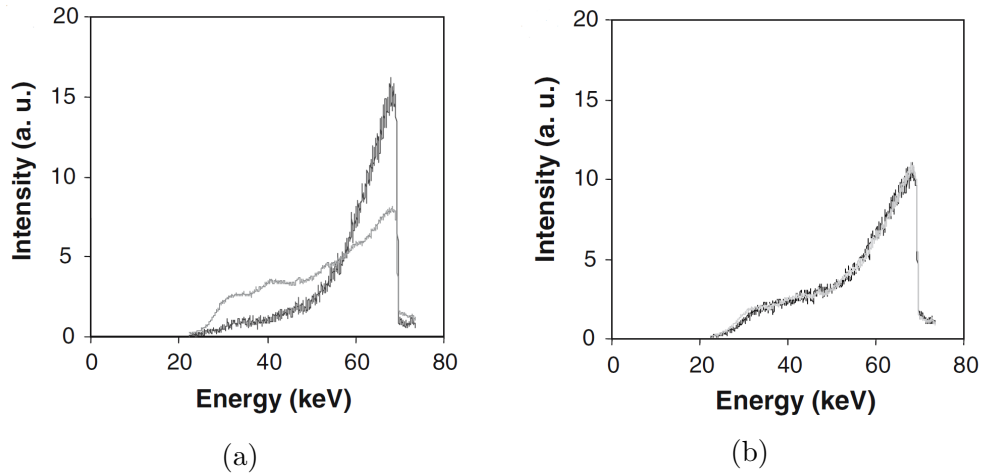


Figure 2.8: Estimating reaction extent ( $x$ ) from EDXRD data (adapted from [49]). (a) shows the initial and final EDXRD spectra; (b) shows the fit obtained on an intermediate spectrum, using Eq. 2.1. “ $x$ ”, i.e. the relative reaction extent is estimated to be 0.628

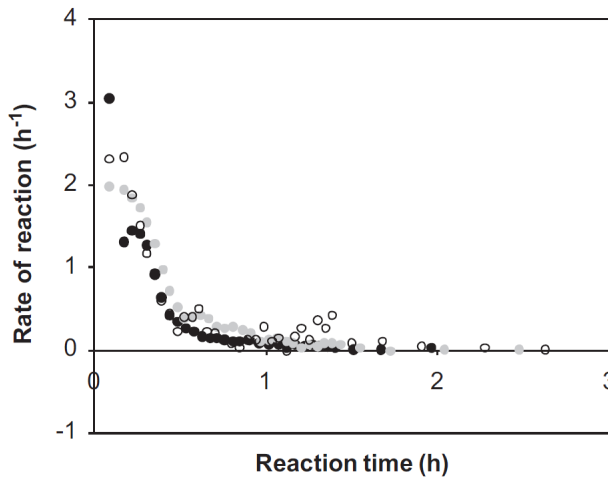


Figure 2.9: Reaction extent vs. time for K-metakaolin geopolymers, with  $\text{Si}/\text{Al}=1$  (filled circles),  $\text{Si}/\text{Al}=1.5$  (gray circles) and  $\text{Si}/\text{Al}=2$  (hollow circles); Plot adapted from [49]

### **2.3.3 Effect of soluble silica on geopolymmerization kinetics**

It has also been well established that a silicate-activated metakaolin geopolymers (with Si/Al ratio between 1.7-2.2) provides an optimum mechanical performance [19–21]. Significant improvement in microstructural homogeneity has been noted (illustrated in Figure 2.10), which explains the increase in compressive strength of geopolymers with Si/Al ratio > 1.0. This increase in homogeneity has been explained by the “syneresis” or breakdown of aluminosilicate structures due to reorganization or transformation processes in the structure. It has been observed that aluminosilicate grouts with lesser  $\text{SiO}_2/\text{Na}_2\text{O}$  ratios exhibit higher syneresis [55] which explains why the microstructures in low-silica geopolymers exhibit discrete regions of less porous gel [20]. It should be noted that the aluminosilicate grouts are dissimilar to geopolymers in the sense that they are diluted with water, and possess a pH of 12.2. Hence, there is no knowledge or evidence of such a syneresis mechanism existing in metakaolin geopolymers, especially in the time-scale of a few hours by which the binder hardens. In addition, the syneresis of aluminosilicate grouts appear to be very low at 1 week, when compared to 5 years [55]. Therefore, it is hard to be convinced that syneresis is the reason behind drastic microstructural differences observed in Figure 2.10.

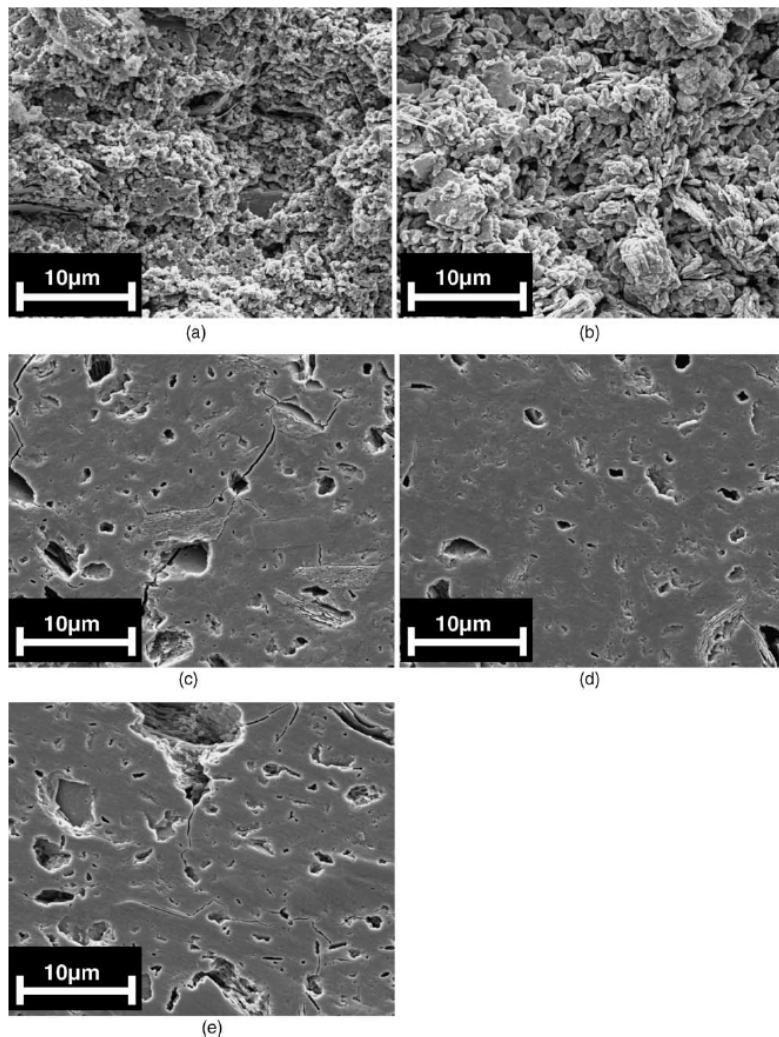


Figure 2.10: Increase in microstructural homogeneity observed in Na-geopolymers with increasing Si/Al ratio of a) 1.15, b) 1.4, c) 1.65, d) 1.90, e) 2.15 (adapted from [20])

In terms of kinetics, DSC data has shown that sodium hydroxide activated metakaolin has a much higher enthalpy of reaction compared to sodium silicate activated metakaolin [34]. Isothermal calorimetry data has shown that the addition of soluble silica (from an activator solution modulus of 1.0-1.6) affects the second calorimetry peak<sup>1</sup> strongly. The peak rate of heat evolution ( $R_{peak,2}$ ) is seen to decrease, and the time at which it takes place ( $t_{peak,2}$ ) increases, with increase in silica modulus in activator solution [51]. Both studies did not provide any explanation for this decrease in reaction rate (or enthalpy) [51]. This

---

<sup>1</sup>with reference to Figure 2.7

reduction in rate of reaction with increasing amounts of silica in activator solution has also been observed in the EDXRD data collected by Provis and van Deventer [49], and has been attributed to a reduced mobility of dissolved species in solution. A reduced mobility of species in silicate activated metakaolin (after hardening) has also been claimed to be the reason due to which metakaolin geopolymers slow down [15], but no direct experimental proof has been presented.

Duxson et al., [20] have provided an explanation of the slow reactivity in silicate activated binders through the concept of lability (interpreted as mixture of mobility and reactivity) of aluminosilicate species in solution. In activator solutions with low silica modulus, most species are silica and alumina monomers, along with a few aluminosilicate dimers and cyclic species [20, 40]. These species have been observed to be more labile than larger cyclic aluminosilicate species [56] that are expected to form in geopolymers prepared from an activator solution with higher silica modulus [20, 40]. Therefore, geopolymers activated with high silica modulus activators should have a slow reaction rate.

## 2.4 Role of silica and alumina species in geopolymers

Key insights about the role of silica and alumina species in the kinetics of geopolymers were obtained through Partial Charge Model (PCM) simulations [57]. The model builds on the concept that metal cations (aluminum and silicon in the case of geopolymers) in aqueous solutions are solvated with water, due to the dipolar nature of water molecules. Consequently, in high pH solutions, the H-OH bond is weakened, and the metal gets hydrolyzed, as shown in Eq. 2.2 [57].



where,  $h$  is the hydrolysis ratio,  $z$  is charge and  $N$  is the coordination number of the cation. PCM can be used to calculate the hydrolysis ratio for Eq. 2.2 for any given pH. If the

hydrolysis ratio is calculated, the species involved in geopolymmerization can be identified. The results from the model [57] indicated that the hydrolysis ratio increases with pH for both silica and aluminate species, and are summarized in Table 2.1. It should be noted that Faimon's model, which has been used to model geopolymmerization kinetics, also predicts the release of monomeric alumina and silica species after dissolution [16, 48].

Table 2.1: Silicate and aluminate species predicted from PCM in geopolymers dissolution  
(Adapted from [57])

pH range	Hydrolysis Ratio (h)	Al species
12-14	$\approx 4$	$[\text{Al}(\text{OH})_4]^-$
10-12	3.6-3.9	$[\text{Al}(\text{OH})_4]^-$ and $[\text{Al}(\text{OH})_3(\text{OH}_2)]$

pH range	Hydrolysis Ratio (h)	Si species
11-14	5-5.5	$[\text{SiO}(\text{OH})_3]^-$ and $[\text{SiO}_2(\text{OH})_2]^{2-}$
10-11	$\approx 5$	$[\text{SiO}(\text{OH})_3]^-$

PCM models were also used to predict the polymerization route preferred by the aforementioned species in Table 2.1. In the alkaline activation of metakaolin, high pH levels ( $\geq 12$ ) are commonplace. Therefore, monomeric  $[\text{Al}(\text{OH})_4]^-$ ,  $[\text{SiO}(\text{OH})_3]^-$  and  $[\text{SiO}_2(\text{OH})_2]^{2-}$  are the species expected to form from dissolution of aluminosilicate precursors. The possible stable products from the polymerization step [29] are summarized in Table 2.2.

Table 2.2: Stable polymerization products from monomeric species (adapted from [29])

Reactants	Product
$[\text{Al}(\text{OH})_4]^- + [\text{SiO}_2(\text{OH})_2]^{2-}$	$[(\text{OH})_3\text{Al}-\text{O}-\text{SiO}_2(\text{OH})]^{3-}$
$[(\text{OH})_3\text{Al}-\text{O}-\text{SiO}_2(\text{OH})]^{3-} + [\text{Al}(\text{OH})_4]^-$	$[\text{Al}_2(\text{OH})_6\text{SiO}_4]^{4-}$
$[\text{Al}(\text{OH})_4]^- + [\text{SiO}(\text{OH})_3]^-$	$[(\text{OH})_3\text{Al}-\text{O}-\text{SiO}(\text{OH})_2]^{2-}$
$[\text{SiO}(\text{OH})_3] + [(\text{OH})_3\text{Al}-\text{O}-\text{SiO}(\text{OH})_2]^{2-}$	$[\text{Al}(\text{OH})_2\text{Si}_2\text{O}_4(\text{OH})_4]^{3-}$
$[\text{SiO}(\text{OH})_3] + [\text{Al}(\text{OH})_2\text{Si}_2\text{O}_4(\text{OH})_4]^{3-}$	$[\text{Al}(\text{OH})\text{Si}_3\text{O}_6(\text{OH})_6]^{4-}$
$[\text{SiO}(\text{OH})_3] + [\text{Al}(\text{OH})\text{Si}_3\text{O}_6(\text{OH})_6]^{4-}$	$[\text{AlO}_4\text{Si}_4\text{O}_4(\text{OH})_8]^{5-}$

The results from the model provide vital information for the geopolymmerization

mechanism. The reactants and products in Table 2.2 within rows 2-6 demonstrate that 3-D network formation can take place unhindered upon reaction of  $[\text{SiO}(\text{OH})_3]^-$ , with monomeric alumina. However, the product  $[(\text{OH})_3\text{Al}-\text{O}-\text{SiO}_2(\text{OH})]^{3-}$  (from the reaction of  $[\text{SiO}_2(\text{OH})_2]^{2-}$  and alumina, Row 1, Table 2.2) can participate in the polymerization only through a nucleophilic attack by alumina on the silicon site. The product from silica species ( $[\text{SiO}_2(\text{OH})_2]^{2-}$ ) attacking the Al site is not stable. Therefore, 3-D network formation cannot take place in through this reaction. This information has important consequences on geopolymmerization; due to this phenomenon, geopolymmerization cannot occur at all ranges of pH. An optimum pH exists, described as follows:

1. Dissolution processes are driven by the pH, with low pH leading to low concentrations of silica and alumina in solution [29]. Therefore, condensation processes, and subsequently the geopolymmerization reaction is hindered.
2. The initial PCM calculations by Weng et al., [57] demonstrate that high pH leads to a higher hydrolysis ratio (Table 2.1). Therefore, with increasing pH, ( $[\text{SiO}_2(\text{OH})_2]^{2-}$ ) formation is preferred over  $[\text{SiO}(\text{OH})_3]^-$ . The discussion based on Table 2.2 shows that ( $[\text{SiO}_2(\text{OH})_2]^{2-}$ ) will not form a 3-D network, and therefore, condensation processes are hindered again.

Calorimetry data presented by Weng et al., [29] demonstrates this trend (Figure 2.11), which strengthens the results from the PCM model. Furthermore, NMR data indicated the presence of free  $[\text{Al}(\text{OH})_4]^-$  till 24h after mixing metakaolin with NaOH solutions. NMR data also proved that free water was consumed initially, and released as the geopolymmerization reaction proceeds, therefore confirming proving the presence of dissolution step and condensation-polymerization step.

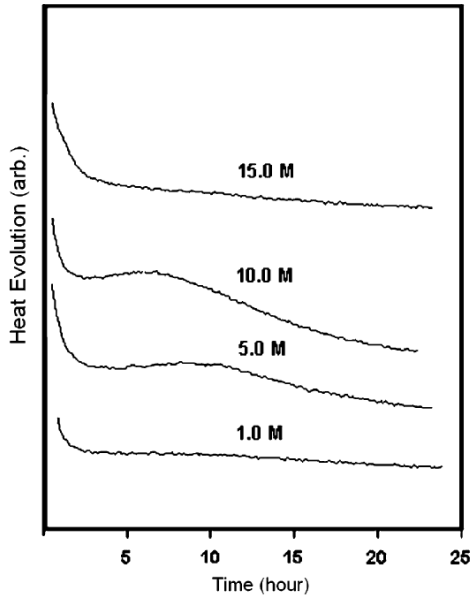


Figure 2.11: Calorimetry data demonstrating the presence of an optimum pH for geopolymmerization, adapted from [29]

The release rate of alumina and silica also have consequences in geopolymmerization. Leaching studies have indicated that the dissolution of metakaolin in sodium hydroxide solutions leads to rapid release of alumina over silica species [29, 45]. The difference in rate of dissolution is probably because alumina species in aqueous solution impede dissolution of silica [35] by forming aluminosilicates on silica surfaces. In-situ ATR-FTIR studies have demonstrated a similar trend, wherein the dissolution of geothermal silica was observed to slow down upto a period of 16 hours in the presence of soluble alumina over solid amorphous alumina [58].

The presence of soluble silica on the reaction kinetics of geopolymmerization has been studied extensively in a geothermal silica-sodium silicate-sodium aluminate binder. The silica availability was changed by adjusting the relative proportions of geothermal silica and sodium silicate. The presence of soluble silica in solution was hypothesized to form aluminosilicate nuclei for product growth away from geothermal silica particles. Spatially resolved FTIR analysis supported the analysis by proving higher dissolution of geothermal silica in samples with soluble silica [59].

## 2.5 Nucleation seeding in cement binders

Similar to the case of geopolymers, the specific mechanisms controlling the rate of portland cement hydration remain unresolved [14]. However, external nucleation seeding has offered crucial insights in the kinetics of portland cement hydration, as demonstrated by the addition of C-S-H gel as an external seed for  $\text{C}_3\text{S}$  hydration by Thomas et al [14]. The addition of C-S-H seed eliminated the early induction period observed in cement hydration (illustrated in Figure 2.12), and the total heat of hydration increased substantially in the first 24h. This observation clearly proved that C-S-H acts as nuclei for further growth of C-S-H; and therefore, the formation of C-S-H products during cement hydration was concluded to be autocatalytic. The autocatalytic effect of C-S-H has been applied in the development of accelerators [60] and understanding different retardation mechanisms in cement hydration [14, 61]. This study clearly shows the potential of using product based seeds to understand the complex nucleation-growth processes in  $\text{C}_3\text{S}$  hydration.

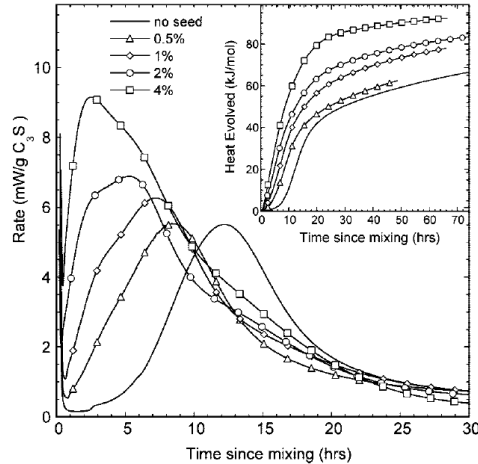


Figure 2.12: Reaction kinetics of  $\text{C}_3\text{S}$  hydration upon external seeding with C-S-H gel  
(adapted from [14])

The consequences of nucleation seeding of cement/ $\text{C}_3\text{S}$  binders with C-S-H are summed up in the following points [14]. These outcomes therefore can serve as a useful point of reference when considering nucleation seeding in alternative binder materials such

as geopolymers.

- The presence of C-S-H nuclei was observed to be crucial for gel growth. Therefore, external seeding would reduce or eliminate the induction period due to the presence of nuclei available for growth
- Reaction kinetics were accelerated at the early age (within the first 12 hours, with reference to Figure 2.12). This result is well in line with the concept of heterogeneous nucleation, wherein the energy barrier for the forward reaction is reduced due to the presence of external surfaces or nuclei for reactions to proceed [62]
- C-S-H formation is greater since the hydration product nucleates at the pore space, and product growth does not form a diffusion barrier on the surface of  $\text{C}_3\text{S}$  grains. This consequently implies that microstructure is refined, as shown in Figure 2.13.

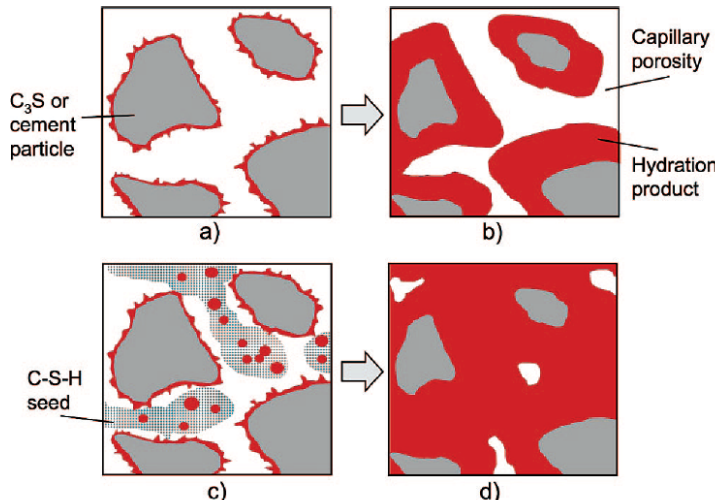


Figure 2.13: Microstructure refinement due to external nucleation seeding (adapted from [14])

Based on the insights into  $\text{C}_3\text{S}$  hydration by C-S-H addition, the acceleration observed in the case of silica based additives such as silica fume was also explained. It was observed that nano  $\text{SiO}_2$  (or colloidal silica) accelerates the hydration reaction significantly, while silica fume (with a larger silica particle size) has a slight accelerating effect, as shown in Figure

2.14 [14]. These observations led to the conclusion that the nucleating surface is not  $\text{SiO}_2$ , but rather C-S-H forming on the reactive silica surfaces. Therefore, colloidal silica, which is more reactive and forms more C-S-H, accelerates the  $\text{C}_3\text{S}$  hydration more when compared to silica fume. The explanation of nucleation seeding in the case of  $\text{SiO}_2$  serves as a useful case in understanding the effects of adding nanoparticles which can chemically react in a binder material system having an autocatalytic growth of reaction products.

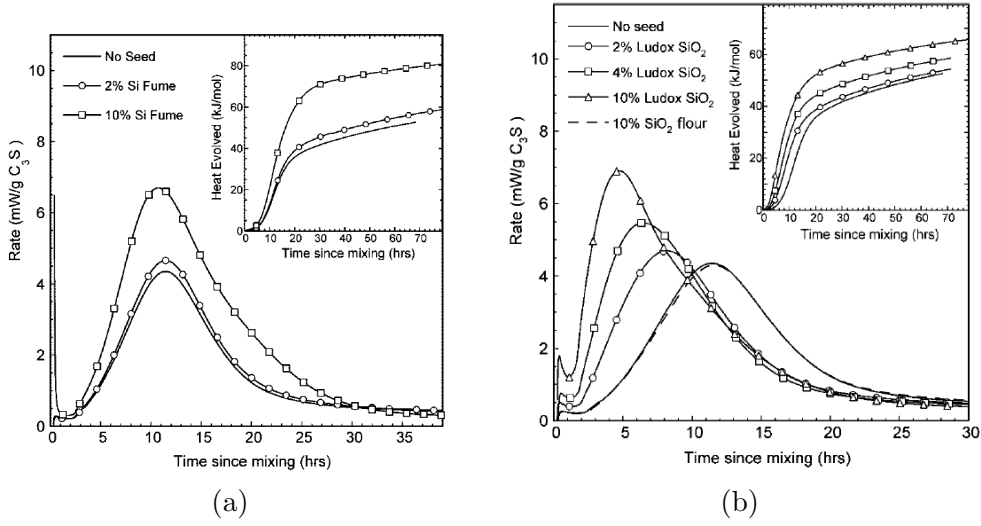


Figure 2.14: (a) Effect of silica fume on  $\text{C}_3\text{S}$  hydration; (b) Effect of colloidal silica on  $\text{C}_3\text{S}$  hydration; Note:  $\text{SiO}_2$  flour (crystalline quartz) has no effect on the reaction (Figures adapted from [14])

Besides product based seeds, inert external seeds such as  $\text{CaCO}_3$  [63] and  $\text{TiO}_2$  [18] have also been observed to act as nucleation seeds in portland cement/ $\text{C}_3\text{S}$  binders. Jayapalan et al. [18] have used  $\text{TiO}_2$  as a seed and observed an increase in the hydration rate for portland cement pastes. Figure 2.15 illustrates this acceleration and also shows the induction period was reduced slightly, unlike the case where C-S-H seeding eliminated the induction period completely (Figure 2.12). The accelerating effect due to seeding subsequently quantified through numerical modeling (Boundary-Nucleation (BN) model and the Avrami model) for nucleation processes [18, 64].

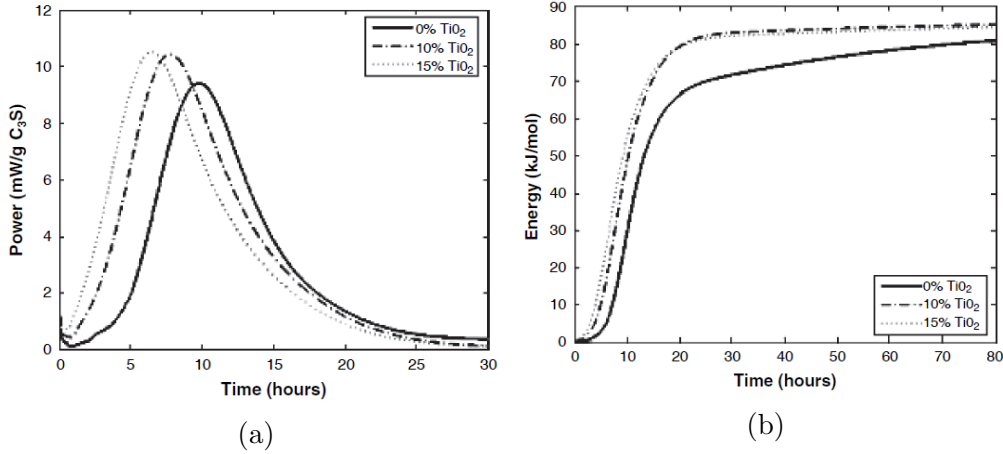


Figure 2.15: (a) rate of heat evolution with TiO<sub>2</sub> addition, reduction in induction period clearly observed; (b) total heat evolution plots demonstrating increase in the total heat evolution upon TiO<sub>2</sub> seeding, implying more hydration products have formed  
(Figures adapted from [18])

Besides TiO<sub>2</sub> and CaCO<sub>3</sub> nanoparticles, crystalline analogues of C-S-H, tobermorite and jennite have also been observed to accelerate cement hydration [65]. The minerals were added in increasing doses from 0.5% - 10% (by wt. of cement); however, at low dosages (<4%), the seeding agents were seen to be ineffective. The authors did not provide any explanation to this observed inefficiency, and has cited the high surface areas of the crystalline materials ( $\approx 200\text{-}280 \text{ m}^2/\text{g}$ ) to be the reason behind the observed acceleration at high dosages. Other studies also exist in cement literature pertaining to nucleation seeding, and effects of adding nanoparticles to cement hydration [66–68] but these studies do not add any new information to interpreting the effects of nucleation seeding on cement hydration kinetics.

## 2.6 Nucleation seeding in geopolymers

There exists limited information on external seeding in geopolymers. As described earlier, the evidence of a nucleation step in the geopolymer mechanism is scarce. Most of the proof is based on analogies to zeolite material systems and aluminosilicate weathering processes [12, 16]. However, two experimental reports exist for external nucleation seeding

in geopolymer binders.

Rees et al., [12] utilized high surface area nano-alumina (BET surface area of  $275\text{m}^2/\text{g}$ ) as a seed in a Class F fly ash-NaOH geopolymer. The addition of a small quantity of alumina (0.01g, to 80g paste mixture) was seen to accelerate the formation of geopolymer gel. This acceleration was characterized through in-situ ATR-FTIR, wherein the geopolymer gel asymmetric stretching band (around  $1100\text{cm}^{-1}$ ) was seen to form 42h earlier than the un-seeded sample, as shown in Figure 2.16. Such an acceleration was attributed to nucleation, since the small amount of added alumina is not going to affect the reaction chemically or through other mechanisms like sorption of dissolved species from fly ash on the alumina seeds. Dissolution of alumina was also ruled out, since adding soluble aluminates in similar quantities did not result in any acceleration. The authors therefore concluded that a nucleation step is the only possible explanation for the phenomenon observed. In addition to differences in reaction rate, seeding also promoted the formation of Zeolite F over Zeolite X, which was seen to form in aged unseeded samples.

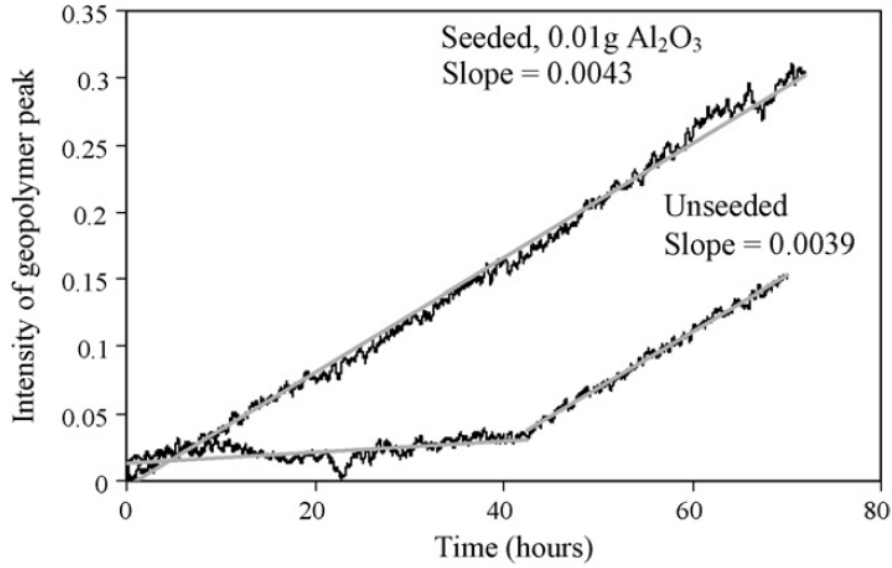


Figure 2.16: Elimination of lag period upon seeding Class F Fly ash-NaOH geopolymers with nano-alumina (adapted from [12])

However, the addition of 0.1g (10 times original amount) of alumina did not lead to

any further increases in reaction rate, which led to the conclusion that nuclei formation is not a rate limiting step in the reaction mechanism. This observation, therefore, raises the question: if nucleation is not a rate limiting step, then why would there be an acceleration in the first place? In addition, the surface area of seed and particle size of seed was described in a powder form. There is no mention of the particle size or surface area of nano-alumina in NaOH solution, where it may form small agglomerates, leading to changes in surface area. The in-situ FTIR technique, while appearing to be successful, is also slightly questionable. ATR-FTIR is extremely sensitive owing to the interaction depth being less than  $10\mu\text{m}$  [69] and therefore, it is not a good descriptor of overall reaction rate. Bulk techniques like isothermal calorimetry would yield clear confirmation of any acceleration that is observed in the reaction rate. Lastly, it should be mentioned that there is no direct evidence of nucleation taking place in fly ash-NaOH binder. Anyhow, the study demonstrates that external seeding of geopolymers shows promise in understanding the mechanism of geopolymerization, and that nano-alumina appears to be effective as a nucleation seed.

Another study on external nucleation seeding was carried out on a two-part geopolymer prepared from geothermal silica and sodium aluminate [13]. Nano ZnO, ZrO<sub>2</sub> and Al<sub>2</sub>O<sub>3</sub> were added as external seeds and in-situ ATR-FTIR was utilized to track differences in reaction rate. The dosage of seed added was 0.5% wt. of solids, which was higher compared to the study by Rees et al. [12]. Once again, monitoring peak intensities of the Si-O-T asymmetric stretching bands demonstrated that the seeds affected the reaction slightly; dissolution of geothermal silica and geopolymer product growth was seen to be accelerated through FTIR peak intensity changes with time. No induction period was observed in these reactions. In addition, a silicon rich phase separated gel was concluded to form upon seeding with nano ZnO and ZrO<sub>2</sub> (indicated by a peak at  $1020\text{cm}^{-1}$  in Figure 2.17).

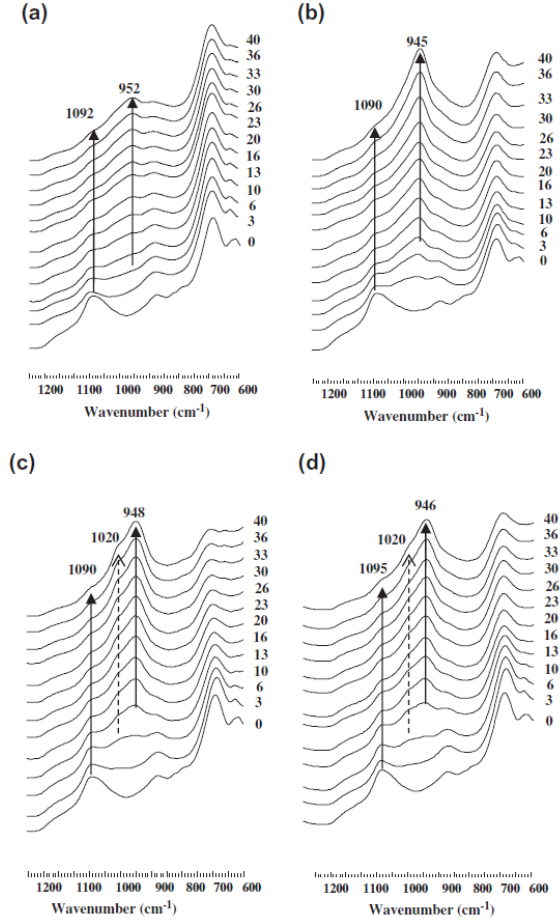


Figure 2.17: In-situ ATR-FTIR data for Geothermal silica-Sodium aluminate geopolymers (a) unseeded, (b) seeded with  $\text{Al}_2\text{O}_3$ , (c) seeded with  $\text{ZnO}$ , (d) seeded with  $\text{ZrO}_2$  (adapted from [13])

The addition of seeds also led to microstructural refinement, and consequently, higher values of compressive strength. EDX analysis indicated that the Si/Al and Na/Al ratios were significantly different in between seeded and unseeded samples. However, the samples were not polished flat, and it appeared that a standardless elemental analysis was carried out. Such analysis can have large errors associated with it, up to the order of 50% [70]. Likewise, the study shares the same drawbacks of utilizing ATR-FTIR only to characterize reaction kinetics, as discussed earlier. It was also unclear as to whether the seeds increased nucleation or growth since the ATR-FTIR method provides no means to distinguish between the two. The presence of a phase separated gel is also hard to confirm through ATR-FTIR

spectra alone. While the authors utilized EDX on 28 days aged samples, it would have been helpful if a similar characterization was done on early age samples to confirm the presence of the phase separated gels claimed from the early age ATR-FTIR spectra. The spatially resolved IR spectroscopy does not aid in this providing this information either, since they were performed at 2 month old samples. In addition, there was no attempt to analyze the stability of nano-Al<sub>2</sub>O<sub>3</sub> particles in solution by adding equal amounts of soluble aluminate species. While Rees's observations were cited for explaining the stability of alumina in alkaline media, it should be noted that Pourbaix diagrams (pH. vs. Potential) of alumina clearly demonstrates that alumina has a thermodynamic preference to dissolve at higher pH values [71].

Besides these two studies on geopolymers, external seeding has also been demonstrated in alkali-activated slag [72]. Synthesized C-S-H gels were utilized for as a seeding agent, and isothermal calorimetry results demonstrated significant acceleration upon addition of 1% C-S-H seed by weight of the slag. The precipitation of C-S-H is well known to be an autocatalytic process [14], and C-S-H/C-A-S-H is also the main product upon the reaction of slag with alkaline activators [26, 73]. External nucleation seeding has also provided key insights into the role of calcium in fly ash-slag-potassium hydroxide binders [11]. However, no further discussion is made on this topic since these binders are a high calcium binders, whereas the main focus of this study is on low-calcium geopolymer binders.

## 2.7 Conclusions

The literature review extensively describes several phenomenon observed in geopolymerization and cement hydration, and all the information presented is used in some form or another in this thesis. However, some of the key points concerning the idea of nucleation in geopolymers that can be concluded from the review are described as follows.

- It is clear that a general agreement exists in understanding the overall mechanism

of metakaolin geopolymers. A two step, solution mediated, dissolution and condensation process takes place which ultimately leads to the formation of geopolymer products. The presence of a nucleation step has been indicated through analogies of zeolite crystallization mechanisms.

- Experimental evidence from in-situ ATR-FTIR and numerical models by Provis have indicated that there is a nucleation and growth process in the transition of a geopolymer from a liquid to solid phase. In comparison to cement hydration processes, where C-S-H has been identified as the nuclei for C-S-H growth, no clear picture of the nucleation step exists in geopolymer binders. In addition, dissolved silica has been claimed to provide nucleation sites for geopolymer growth but no explanation has been provided to the slowdown observed in rate of reaction, upon increased addition of soluble silica in the activator solution.
- Potential seeds in geopolymer binders include high surface area  $\text{Al}_2\text{O}_3$ ,  $\text{ZnO}$  and  $\text{ZrO}_2$  nanoparticles.  $\text{SiO}_2$  nanopowders has been observed to provide sites for C-S-H product nucleation in cement binders, which in turn catalyzes the cement hydration reaction.  $\text{TiO}_2$  nanopowders have also demonstrated the ability to act as nucleation seeds. All these nanoparticles (with the exception of  $\text{ZrO}_2$ ) have been investigated in this study.
- The importance of studying and understanding nucleation processes can be observed from the developments in cement binders after C-S-H was revealed as a nucleation seed. This understanding has been utilized to understand mechanisms of cement hydration and effects of silica based additives on hydration kinetics. In addition, commercial accelerators have been developed for concrete construction based on synthesized C-S-H. Similar progress have been made in understanding the reaction mechanisms of medium calcium alkali-activated binders through external nucleation seeding.

# **Chapter 3**

## **Synthesis and characterization of seeding agents**

### **3.1 Introduction**

The purpose of this chapter is to provide the necessary information pertaining to the synthesis and characterization of the seeding agents used in this study. The zeolite A and X nanopowders used as seeds were synthesized hydrothermally. Subsequently, they were characterized through XRD, XRD-Rietveld, FTIR, SEM, DLS, XRF and Nitrogen adsorption. In addition to these tests, NMR was carried out on Zeolite A, and ESEM was performed on Zeolite X. Commercial TiO<sub>2</sub>, SiO<sub>2</sub>, ZnO and Al<sub>2</sub>O<sub>3</sub> nanopowders (US Research Nanomaterials) were procured and characterized through DLS and SEM.

### **3.2 Commercial nanopowders**

TiO<sub>2</sub>, SiO<sub>2</sub> and ZnO nanopowders were procured from US Research Nanomaterials. Particle size and surface area of the nanopowders as provided by the manufacturer (particle size measured through transmission electron microscopy; surface area was calculated by using size and density of the powders) is presented in Table 3.1.

Table 3.1: Properties of TiO<sub>2</sub>, SiO<sub>2</sub> and ZnO nanopowders (as specified by manufacturer)

Nanopowder	Average Particle Size (nm)	Specific surface area (m <sup>2</sup> /g)
TiO <sub>2</sub>	5	289
SiO <sub>2</sub>	15-20	170 to 200
ZnO	18	40 to 70

### 3.3 Synthesis of nano-zeolite X and A

The procedures for synthesizing nano-zeolite X [74, 75] and Zeolite A [76] were adopted from literature. For both the zeolite synthesis procedures, two solutions were prepared, with one providing silica and the other providing alumina. Fumed silica (Sigma Aldrich) and sodium aluminate (Sigma Aldrich) were used as sources for silica and alumina, respectively.

#### 3.3.1 Structure of zeolite A and zeolite X

The structure of Zeolite A has been described in terms of a truncated octahedra of 24  $\text{SiO}_2$  and  $\text{AlO}_4$  tetrahedra, termed as  $\beta$ -sodalite, which is connected octahedrally by double 4-membered rings (D4R) [37]. Owing to this arrangement, only  $\text{Q}^4(4\text{Al})^1$  Si sites are present in the structure. Based on an XRD powder diffraction card of zeolite A (PDF #97-008-8329), the crystal structure is shown in Figure 3.1.

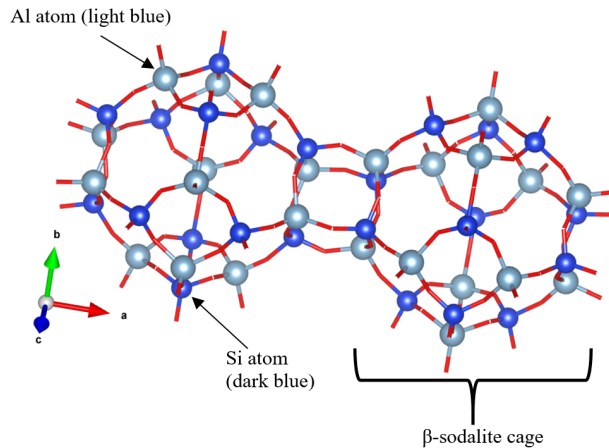


Figure 3.1: Ball and stick model of synthesized zeolite A, with two  $\beta$ -sodalite cages connected three dimensionally through the double 4 membered rings

Zeolite X possesses a structure similar to that of Zeolite A, consisting of  $\beta$ -sodalite cages bound together through double 6-membered rings (D6R), instead of the 4-membered

<sup>1</sup>Q notation by Engelhardt et al. [37] has been used in this study

rings. The Si/Al ratio is variable though, ranging between 1.18 and 1.5 [77], which leads to variability in the distribution of Q<sup>4</sup> silicon sites in the zeolite. Ball and stick structure of Zeolite X (PDF #97-006-5500) is shown in Figure 3.2.

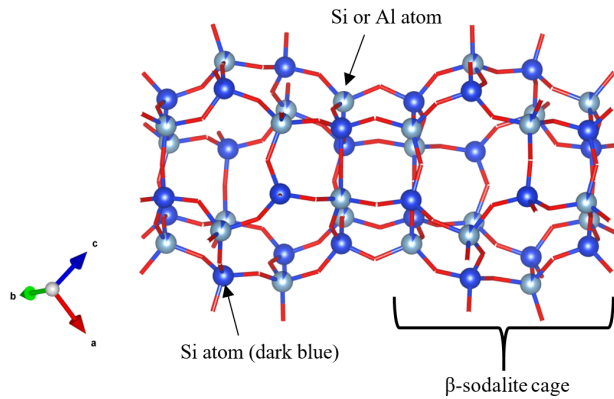


Figure 3.2: Ball and stick model of zeolite X, with two  $\beta$ -sodalite cages connected three dimensionally through the double 6 membered rings

### 3.3.2 Synthesis of zeolite X

For the synthesis of Zeolite X, a net solution stoichiometry of 5.5 Na<sub>2</sub>O:1.0 Al<sub>2</sub>O<sub>3</sub>:4.0 SiO<sub>2</sub>:190 H<sub>2</sub>O has been used. A silicate solution was prepared by stirring 4.96g of fumed silica and 52.5g nanopure water at 600RPM on an orbital shaker for  $\approx$ 30min. A sodium aluminate solution was prepared by stirring 3.28g sodium aluminate, 7.2g NaOH pellets (Fisher,  $\geq$ 97% purity) and 14.47g nanopure water with a magnetic stirrer for 30min. Besides ensuring uniform dissolution, the stirring time of 30min ensures the aluminate solution cools down to room temperature (reaction of sodium hydroxide pellets with water generates heat). Both solutions were prepared in polyethylene bottles. After stirring, the silicate solution was transferred to the aluminate solution, and stirring was continued for 24h as per the procedure in [75]. After 24h, the bottle was transferred to a water bath maintained at a temperature of  $\approx$ 70°C for 48h. This step is a deviation from the reported synthesis procedure [75], which calls for heating the solution at 60°C for 96h. However, XRD indicated that the Zeolite X synthesized through these two procedures were very similar, and the method used

in this study generates the product faster. After the 48h heating process, the resultant aluminosilicate liquid (in the form of a viscous white gel) was vacuum filtered through a Grade 1 Whatman filter paper. The resultant gel on the filter paper is referred to as “wet seed”. The wet seed was dried at 105°C to yield Zeolite X powder, which was used for further characterization tests. The wet seed was characterized through ESEM and FTIR.

### 3.3.3 Synthesis of zeolite A

For the synthesis of Zeolite A, a net solution stoichiometry of 6.0 Na<sub>2</sub>O:0.55 Al<sub>2</sub>O<sub>3</sub>:1.0 SiO<sub>2</sub>:150 H<sub>2</sub>O has been used. A silicate solution was prepared by stirring 4.96g of fumed silica and 100g nanopure water at 600RPM on an orbital shaker for ≈30min. A sodium aluminate solution was prepared by stirring 7.21g sodium aluminate, 34.88g NaOH pellets and 108.74g nanopure water with a magnetic stirrer for 30min. Both solutions were prepared in polyethylene bottles. After stirring, the silicate solution was transferred to the aluminate solution, and stirring was continued for 3h as per the procedure in [76]. After 3h, the bottle was transferred to a water bath maintained at a temperature of ≈50°C for 48h. After the 48h heating process, the resultant aluminosilicate liquid (in the form of a viscous gel, similar to that of Zeolite X) was vacuum filtered through a Grade 1 Whatman filter paper. The resultant gel on the filter paper was dried at 105°C to yield Zeolite A powder, which was then used for further characterization tests.

## 3.4 Characterization

A Siemens D5000 diffractometer was used in the Bragg-Brentano configuration to collect powder XRD patterns. The electron gun voltage was maintained at 40kV and emission current set at 30mA. A single crystal silicon holder was used as it does not contribute to the background in the XRD patterns. Phase matching for the zeolites was carried out using MDI Jade Version 9.6. Rietveld refinement for zeolite X was carried out on TOPAS Version

## 5.

XRF for the synthesized zeolites and aluminosilicate was carried out on a Shimadzu EDX-7000 instrument using a Rhodium X-ray source. All samples were measured in a helium atmosphere, and a fundamental parameter method was used to generate quantitative values for the elemental composition of samples.

A cold field emission SEM (Hitachi S4700) was used in the secondary electron mode, to characterize the particle size and morphology of the nanopowders and zeolites. 0.1g of powders/zeolites was dispersed in 30ml of ethanol, in an ultrasonic bath, and one drop of the dispersion was placed on a pure carbon film mounted on a 200-mesh TEM Grid (Ted Pella). Ethanol was allowed to evaporate at room temperature, leaving dispersed nanopowders on the TEM grid. This method allows for imaging the morphology and size of individual nanoparticles without any sputter coating. An Environmental SEM (ESEM), FEI Quanta 450, with a field emission source was used to image Zeolite X in the form of wet-seed.

A Malvern Zetasizer Nano ZS was used in this study to determine the particle size distribution of nanopowders after dispersion in NaOH solution. Particle size detection range for the instrument lies between 0.3nm and 6 $\mu$ m. The light source was a laser operating at 632.8 nm and scattered light was collected in the backscatter mode, at an angle of 173° to the incident light. Laser position was automatically detected based on trials carried out by the instrument before measurement. Intensity of light was also adjusted automatically by an attenuator during these trials, ensuring that the detector is neither under-saturated or over-saturated. Prior to DLS measurements, the seed was dispersed in sodium hydroxide solution using a Probe sonicator. The proportion of nanopowder-sodium hydroxide was the same as that used for preparing seeded MK-NaOH samples. Hydroxide solution was taken in the mixing cup, with appropriate amount of seed, and sonicated for 10 minutes. To allow for heat dissipation, the sonicator was operated in a pulsed mode while the sample container was kept in an ice-water bath. Amplitude of sonication was kept at 30% of the maximum rated amplitude for the tip used (manufacturer recommends that the level should be kept

below 40%). Post probe sonication, the solution was equilibrated to 22°C. The solution was agitated on a benchtop vortex stirrer for 1 minute. Subsequently, around 2-3 ml of solution was transferred to a disposable plastic cuvette for DLS measurements. The efficacy of the Zetasizer measurements were first verified on a polystyrene latex standard of known particle size distribution. Viscosity of the sodium hydroxide solution was taken to be 21.95 mPa-s, based on technical data available [78].

Infrared spectra of the zeolites and aluminosilicates were collected on a Perkin Elmer Frontier Spectrometer. An Attenuated Total Reflectance (ATR) attachment with a diamond crystal was used for the measurements. An average of 8 scans were taken for each spectra, with a resolution of  $4\text{cm}^{-1}$ .

Nitrogen adsorption was carried out on a Micromeritics ASAP2020 instrument to measure the BET surface area of zeolites. The samples were pre-degassed at 150°C for 24h and at 300°C for 3h, both under a vacuum pressure of 30mm Hg.

$^{29}\text{Si}$  NMR spectra<sup>2</sup> were collected on Zeolite A using a Varian Inova Spectrometer operating at 7.04T. A 90° pulse, with a width of 2.5μs was used. Recycle delay was kept at 30s and 2048 scans were measured for each spectrum. Peak deconvolution was carried out using MNova v11.0.1 (Mestrelab Research S.L.).

## 3.5 Results

### 3.5.1 Characterization of commerical nanopowders

SEM images of TiO<sub>2</sub>, SiO<sub>2</sub> and ZnO nano-powders are shown in Figure 3.3. TiO<sub>2</sub> particles were observed for agglomerates around 500nm in size. Smaller TiO<sub>2</sub> particles below 100nm are barely discernible from the micrograph in Figure 3.3a. ZnO nanopowders were also observed to form agglomerates around 500nm in size, although smaller particles

---

<sup>2</sup>All NMR spectra in this thesis were collected by Dr. Xu Chen at the University of Illinois Urbana Champaign and University of Delaware. The data was included for the sake of completeness

below 100nm were clearly discernible in Figure 3.3c. Figure 3.3a showed  $\text{SiO}_2$  nanoparticles possessing a size between 100-200nm. All the commercial nanopowders possessed an irregular morphology. The manufacturer reports a much smaller particle size (Table 3.1), imaged through TEM. Particle size ranges mentioned in Table 3.1 are close to the resolution of the field emission SEM, and thus was not observed in the micrographs.

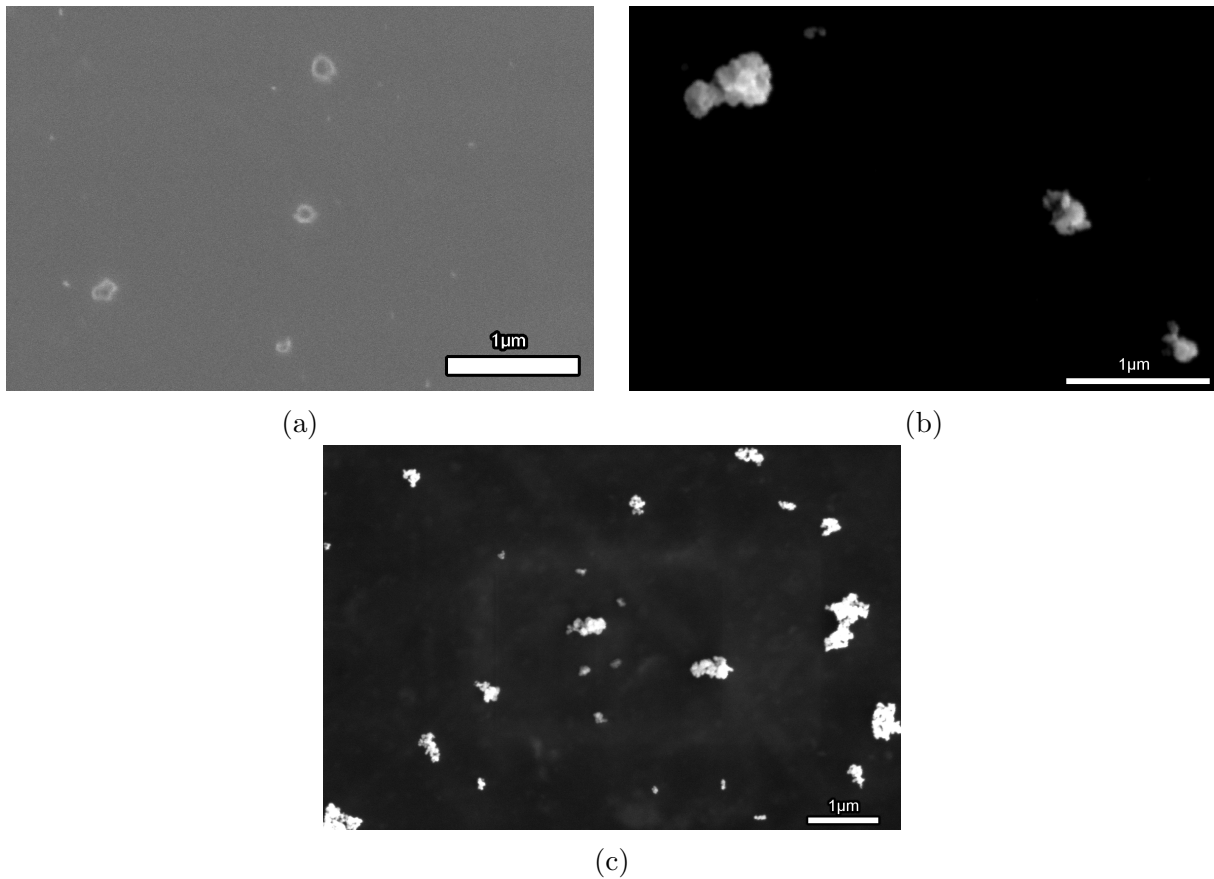


Figure 3.3: SEM micrographs of (a)  $\text{SiO}_2$ , (b)  $\text{TiO}_2$  and (c)  $\text{ZnO}$  nanopowders

The dispersion of 1% $\text{TiO}_2$  in NaOH results in an opaque white solution. DLS experiments on this sample failed because the opaque solution led to issues with absorbance of light and the detector was always undersaturated. Subsequently, the concentration was lowered to 0.1%  $\text{TiO}_2$ . Since the particle concentration usually does not affect the hydrodynamic diameter, this measurement is assumed to yield a similar PSD to 1.0%  $\text{TiO}_2$  in NaOH. On the other hand, 1%  $\text{ZnO}$  was also tested on DLS; the dispersion of  $\text{ZnO}$  in NaOH yielded a more or less clear liquid and no dilution was required for the measurements.

Particle size distribution for nano-silica was measured through a 5% $\text{SiO}_2$  solution in NaOH. However, nano-silica dissolves in NaOH solutions to yield silica species [39]. Therefore, the size of silica particles should be treated with caution, since DLS is reporting the particle size distribution of polymerized silica species. No references to this particle size is used in the discussion section. Z-avg and PDI measurements for the three nanopowders are shown in Table 3.2. Particle size distribution of the nanopowders are presented in Figure 3.4.

Table 3.2: Average particle size and poly-dispersity index of the nanopowders

Sample	Average particle diameter (nm)	Polydispersity Index (PDI)
$\text{TiO}_2$	1233	0.080
$\text{ZnO}$	189	0.378
$\text{SiO}_2$	252	0.169

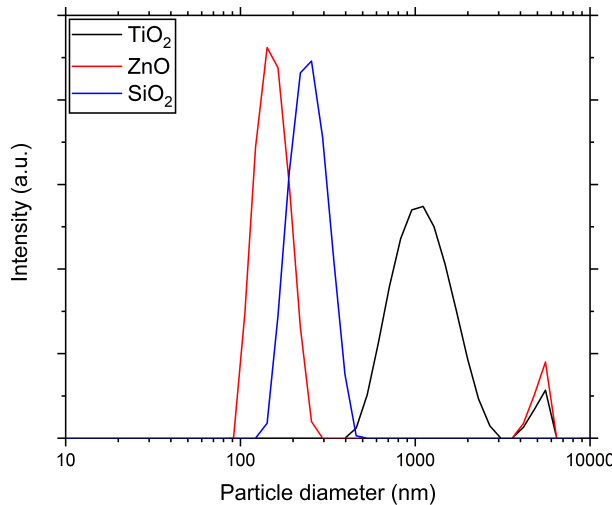


Figure 3.4: Particle size distribution of nanopowders in NaOH solution

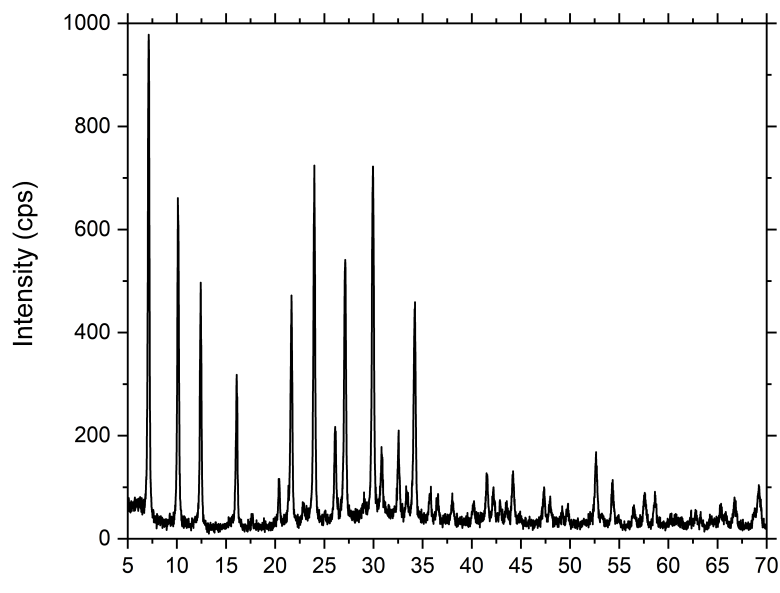
Test results indicate that the  $\text{TiO}_2$  is not stable in NaOH since the reported Z-avg comes out to be exceeds 1 $\mu\text{m}$ , whereas the SEM micrograph in Figure 3.3b shows particles in the  $\approx 50\text{nm}$  range. The light scattering test also detected the presence of flocculating particles, which corroborates with the tendency of  $\text{TiO}_2$  to flocculate in NaOH solutions. Z-avg reported matches closely with the peak size reported through particle size distribution

which demonstrates the accuracy of the experiment. On the contrary, ZnO appears to be in a well dispersed state, with Z-avg being measured as 189nm, against a reported 18nm. The primary particles as measured by the manufacturer through TEM appears to aggregate to form these small flocs, based on the DLS results. The polydispersity index was high, but it is probably attributed to the formation of small micron sized flocs which is seen from the particle size distribution of the sample. Once again, the agreement of Z-avg with the peak position in particle size distribution indicates a good measurement. Additionally, particle size of ZnO observed in the SEM images corroborates well with what is observed from DLS measurements. This indicates that the dispersed solution is stable. TiO<sub>2</sub> is clearly forming a flocculated system in NaOH since the particle size of the material through SEM can be seen to be much lesser than what is reported through DLS measurements. There is no evidence presented which shows that the aggregates break down during the geopolymmerization process.

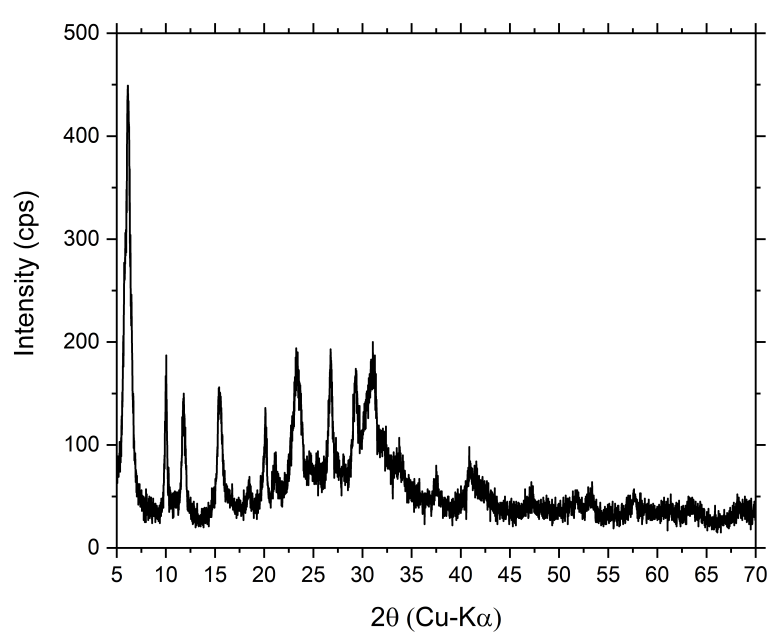
### 3.5.2 Characterization of nanozeolites

#### Validating synthesis

XRD analysis of the zeolite nanopowders revealed no crystalline impurities through the synthesis. The phase match process led to the identification of zeolite A (PDF# 97-008-8329) and zeolite X (PDF# 97-006-5500). The patterns are presented in Figure 3.5, and all crystalline peaks were confirmed to be coming from the respective zeolites. Zeolite A was observed to have narrow, sharp peaks, and the baseline was almost horizontal. This indicated that zeolite A was almost 100% crystalline. A hump was observed in the XRD pattern of zeolite X, from a  $2\theta$  value of  $\approx 20^\circ$  to  $35^\circ$ , which is indicative of an amorphous phase present. The lower peak intensities and larger peak half-widths of zeolite X compared to zeolite A also suggests that the zeolite x is not completely crystalline.



(a)



(b)

Figure 3.5: XRD patterns of (a) Zeolite A and (b) Zeolite X

Subsequently, Rietveld refinement was adopted to characterize the percentage

crystallinity in zeolite X. Crystalline ZnO (Acros Organics) was used as an internal standard to quantify the % crystallinity, and a powder sample was prepared by lightly grinding zeolite X and ZnO for 5 minutes in a 3:1 ratio (by wt.). The refinement was carried out using the crystallographic information file associated with PDF #97-020-0522 and the refined powder diffraction pattern is shown in Figure 3.6). The plausibility of the refined structure was confirmed in the same way as described in Appendix B. The lattice parameter in the refined structure changed by 0.03Å, and all the atomic sites were displaced by  $\leq 0.1\text{\AA}$ . Given that the Si/Al ratio is typical to zeolite X, the refined structure was deemed to be acceptable. The percentages of ZnO (internal standard) and zeolite X from the refinement was used to estimate the amount of crystalline zeolite X, using Equation 3.1 [79].

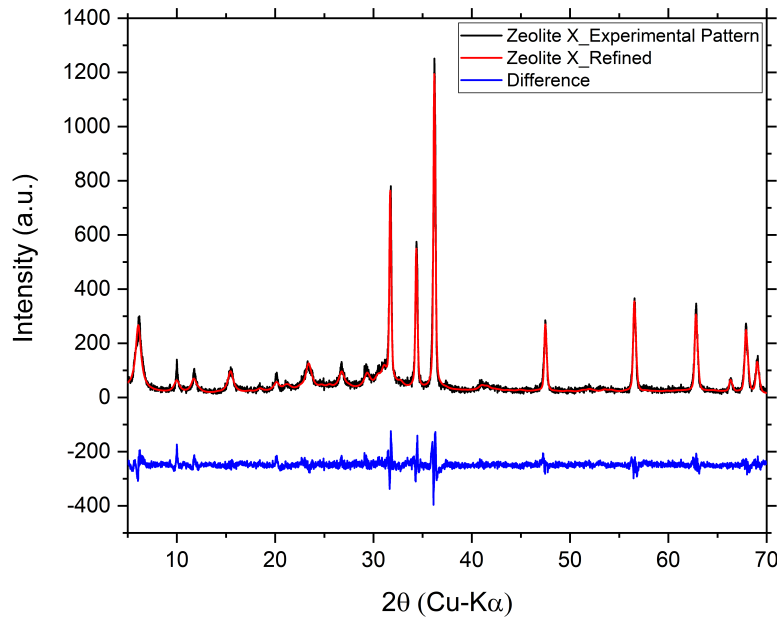


Figure 3.6: Rietveld refinement of synthesized zeolite X with ZnO internal standard

$$\text{Percent amorphous phase} = \frac{1 - \frac{W_{IS}}{W_{RIT}}}{100 - W_{IS}} \times 10^4 \quad (3.1)$$

where,  $W_{IT}$  is the % wt. of internal standard mixed with sample, and  $W_{RIT}$  is the % wt. of

internal standard as calculated by rietveld refinement.

The calculations indicated that the zeolite X was 14% crystalline (with Si/Al ratio of 1.1), with the remainder being an amorphous aluminosilicate. Percentage crystallinity was also estimated by comparing the ratio of Bragg diffraction peak areas of the synthesized zeolite X with those of a commerical molecular sieve (Type 13X, Alfa Aesar), assuming that the molecular sieve is 100% crystalline. Peak areas at  $6^\circ$ ,  $10^\circ$  and  $11.5^\circ$   $2\theta$  were calculated for the synthesized and commercial zeolite X. Subsequently, the ratio between the area under a particular peak for the synthesized and commerical zeolite X was used as a measure of percent crystallinity. The average( $\pm$ standard deviation) of this ratio from three peaks was calculated to be  $33 \pm 11\%$ . While this estimation using areas under the peak is highly approximate (the intensity of XRD patterns depend on many different factors besides percent crystallinity, which may not be same for the two samples tested here [80]), it is close to the percent crystallinity reported from Rietveld refinement. Therefore, the results from the Rietveld refinement is judged to be accurate.

FTIR spectra for the zeolites are presented in Figure 3.7a. The asymmetric Si—O—T stretching peak for zeolite A at  $983\text{cm}^{-1}$  is symmetric, indicating a single silicon environment. The sharp peak at  $552\text{cm}^{-1}$  is assigned to D4R ring vibrations in the zeolite [81], and the intensity of the peak relative to the asymmetric stretching peak shows that the sodalite cages are well connected. On the other hand, the asymmetric stretching peak for zeolite X is not symmetric and there is a shoulder at  $1065\text{cm}^{-1}$ . This is indicative of multiple silicon environments present in the structure. The D6R ring vibration at  $563\text{cm}^{-1}$  has low intensity indicating that the rings are not well formed. Therefore, FTIR results corroborate well with XRD on the fact that zeolite X is not fully crystalline. Some water is always bound to zeolites, and was observed through the peak at  $1653\text{cm}^{-1}$ .

The precursor to zeolite X (obtained by drying the aluminosilicate gel formed after 24h stirring at room temperature) was also introduced as a seed in certain experiments. FTIR data for the amorphous precursor is compared to the semi-crystalline zeolite X, in

Figure 3.7b. It is clear that the precursor is amorphous, since it does not exhibit any of the D6R peaks, characteristic of crystalline zeolite structure, at  $563\text{cm}^{-1}$ . The peak width for the main asymmetric Si–O–T bond is higher in the case of the amorphous precursor, as observed from the normalized spectra in Figure 3.7b. This observation indicates that aluminum substitution in the amorphous zeolite X precursor is lesser or the silica species are more polymerized. Presence of silanol groups in the zeolite X precursor are indicated from the shoulder at  $\approx 900\text{cm}^{-1}$ . IR spectrum of the wet zeolite X seed is shown in Figure 3.7c.

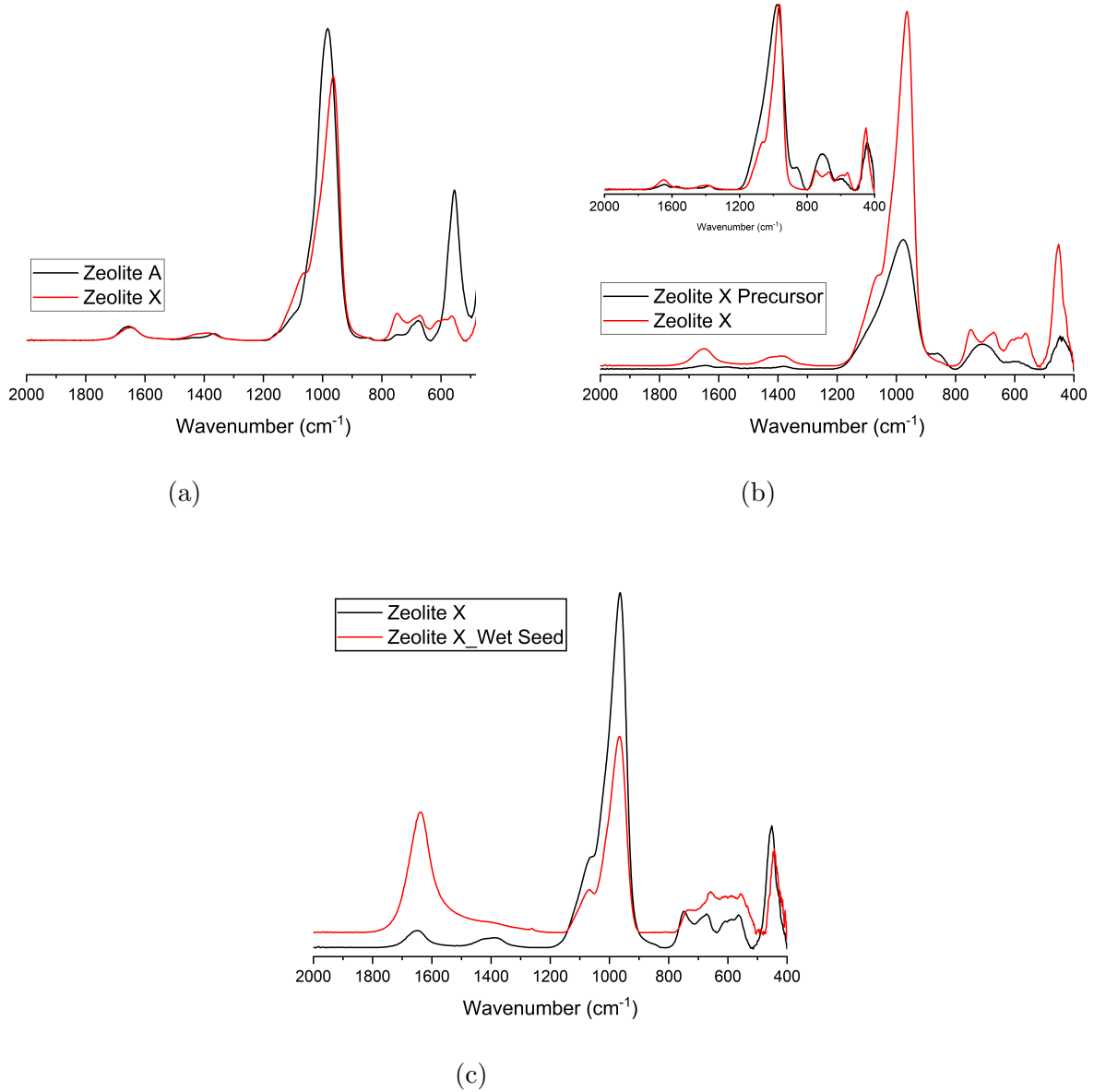


Figure 3.7: FTIR spectra of (a) synthesized Zeolite A and Zeolite X, (b) semi-crystalline Zeolite X and its precursor (normalized spectra are shown inset) and (c) Dry and wet zeolite X seed

XRF results for the two zeolites are presented in Table 3.3. The Si/Al ratio for zeolite A was 1.0 and 1.3 for Zeolite X. As described in Section 3.3.1, zeolite A is expected to have a Si/Al ratio of 1.0. Thus, the XRF, FTIR and XRD results provide substantial proof of the synthesized zeolite A being phase pure. In addition, <sup>29</sup>Si NMR spectrum of the

zeolite A is shown in Figure 3.8, and single peak centered at -89.15 ppm was noted, which corresponds well with Q<sup>4</sup>(4Al) sites [82]. Therefore, it is concluded that zeolite A was phase pure. Zeolite X can have variable Si/Al ratio between 1.18 and 1.5 [77] and the measured Si/Al ratio falls within this range.

Table 3.3: Elemental composition of Zeolite A and X

	SiO <sub>2</sub>	Al <sub>2</sub> O <sub>3</sub>	Na <sub>2</sub> O
Zeolite A	42.4	35.0	22.5
Zeolite X	48.8	31.2	19.9

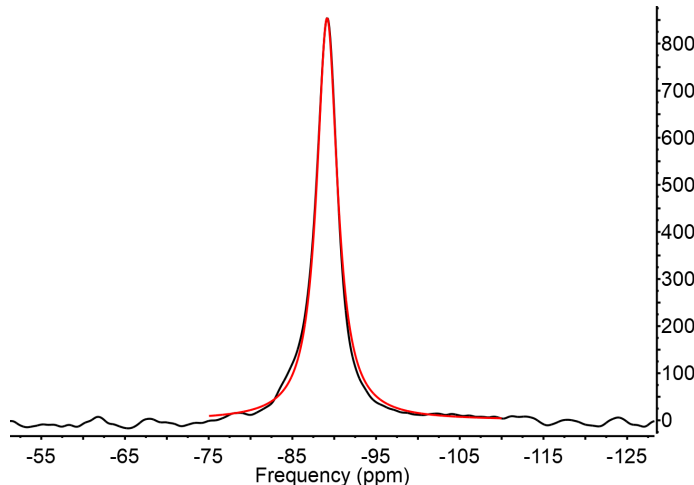


Figure 3.8: <sup>29</sup>Si NMR spectrum of Zeolite A (black) and deconvoluted peak (red)

### Particle size and dispersion of zeolites

Nitrogen adsorption and desorption plots for the nano-zeolites are shown in Figure 3.9. The BET surface area of zeolite A and X came out to be 32 m<sup>2</sup>/g and 229 m<sup>2</sup>/g respectively. However, the isotherm linear plot used for calculating BET surface area had a very low negative y-intercept. This result is not ideal since a negative intercept is not theoretically possible [83]. The degassing also caused a change in the chemical structure of the zeolites, as observed from FTIR spectra before and after the experiment. Nevertheless, SEM micrographs of the zeolite powders before and after the experiment did not reveal any

drastic morphological or particle size difference. Therefore, in qualitative terms, the surface area of zeolite X is clearly greater than zeolite A.

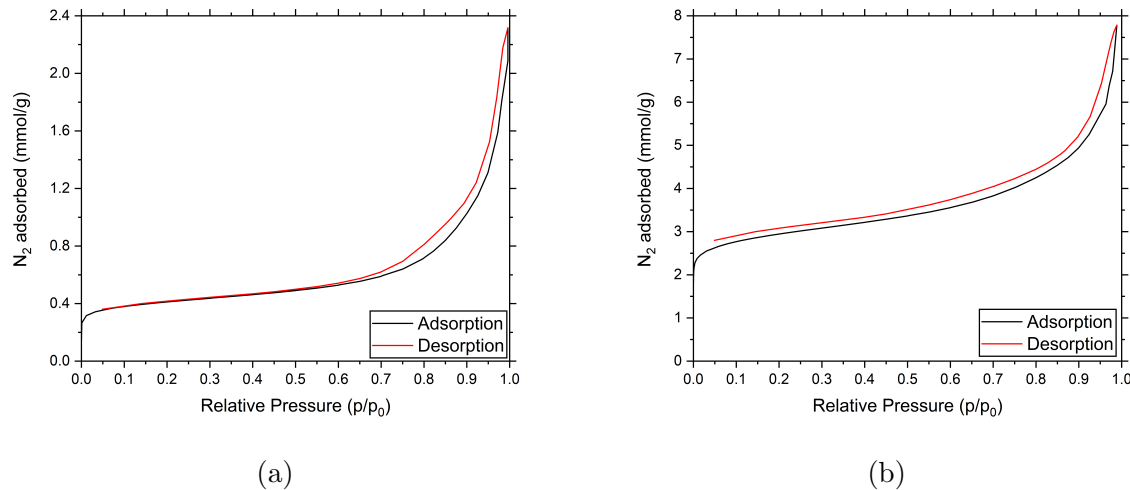


Figure 3.9: Nitrogen adsorption and desorption isotherms of (a) Zeolite A and (b) Zeolite X

SEM micrographs of synthesized zeolite A and X are presented in Figure 3.10. Zeolite A was observed to be highly crystalline, with well defined cubical particles, most of which was observed in an agglomerated state. Size of the individual cubical zeolite A crystals were observed to be  $>250\text{nm}$ . Zeolite X was observed to be composed of small particulates with size  $<200\text{nm}$ , with some particles being in an agglomerated state.

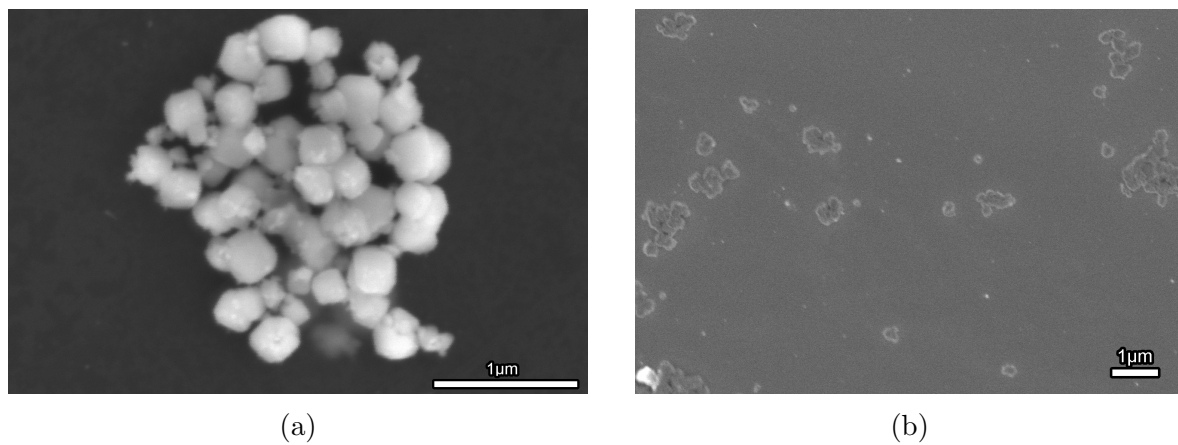


Figure 3.10: SEM micrograph of (a) synthesized zeolite A, and (b) synthesized zeolite X

DLS average particle size, polydispersity index are reported in Table 3.4 and particle size distribution is shown in Figure 3.11. DLS did not indicate any issues with agglomeration for zeolite X but particle sizes for zeolite A was seen to vary. The larger particle sizes of zeolite A indicate that it should have lesser surface area than zeolite X, which is consistent with the surface area measurements presented earlier. The DLS results are also consistent with the SEM particle size measurements. Qualitatively, zeolite A was observed to be in agglomerated state of varying sizes and also in individual cubic crystals, which is reflected in the high PDI value. On the other hand, zeolite X was observed to have fewer agglomerations.

Table 3.4: Average particle size and poly-dispersity index of synthesized zeolites

Sample	Average particle diameter (nm)	Polydispersity Index (PDI)
Zeolite X	69	0.235
Zeolite A	355	0.436

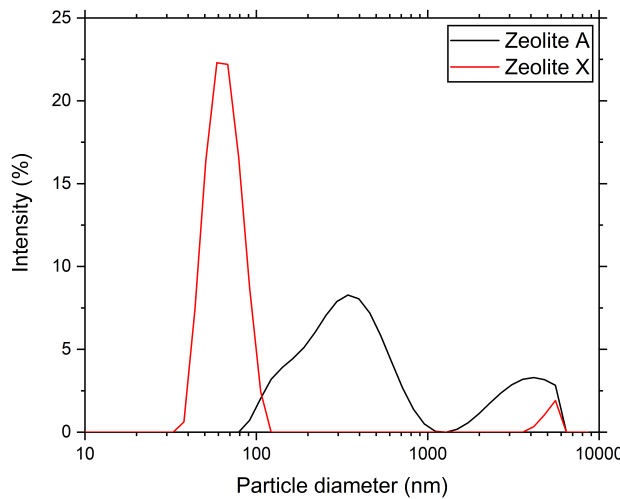


Figure 3.11: Particle size distribution of synthesized zeolites in NaOH solution

ESEM was used to understand the morphological changes in zeolite X wet seed upon drying and wetting cycles. A small quantity of gel was imaged first at 100% RH, and the humidity was decreased to 90%, followed by 50% and 0%. Micrographs were also obtained by

restoring the humidity back to 100%. Resulting ESEM micrographs are presented in Figure 3.12. The microstructure at high humidity levels in Figures 3.12a and 3.12b showed discrete particles with a size  $\leq 200\text{nm}$  throughout the microstructure. Upon drying, these particles were no longer observed in Figures 3.12c and 3.12d. It should be noted that Figures 3.12b, 3.12c and 3.12d are taken from the same region. Re-wetting or increasing the humidity back to 100% led to the formation of some discrete particles, but the original microstructure was not obtained anymore, as observed in Figure 3.12e. The disappearance of these particles consequently implies that the microstructure has lesser surface area. The ESEM micrographs presented here indicates that drying leads to a reduction in surface area, and this decrease is not completely reversible upon re-wetting. Therefore, wet seed was used for this study.

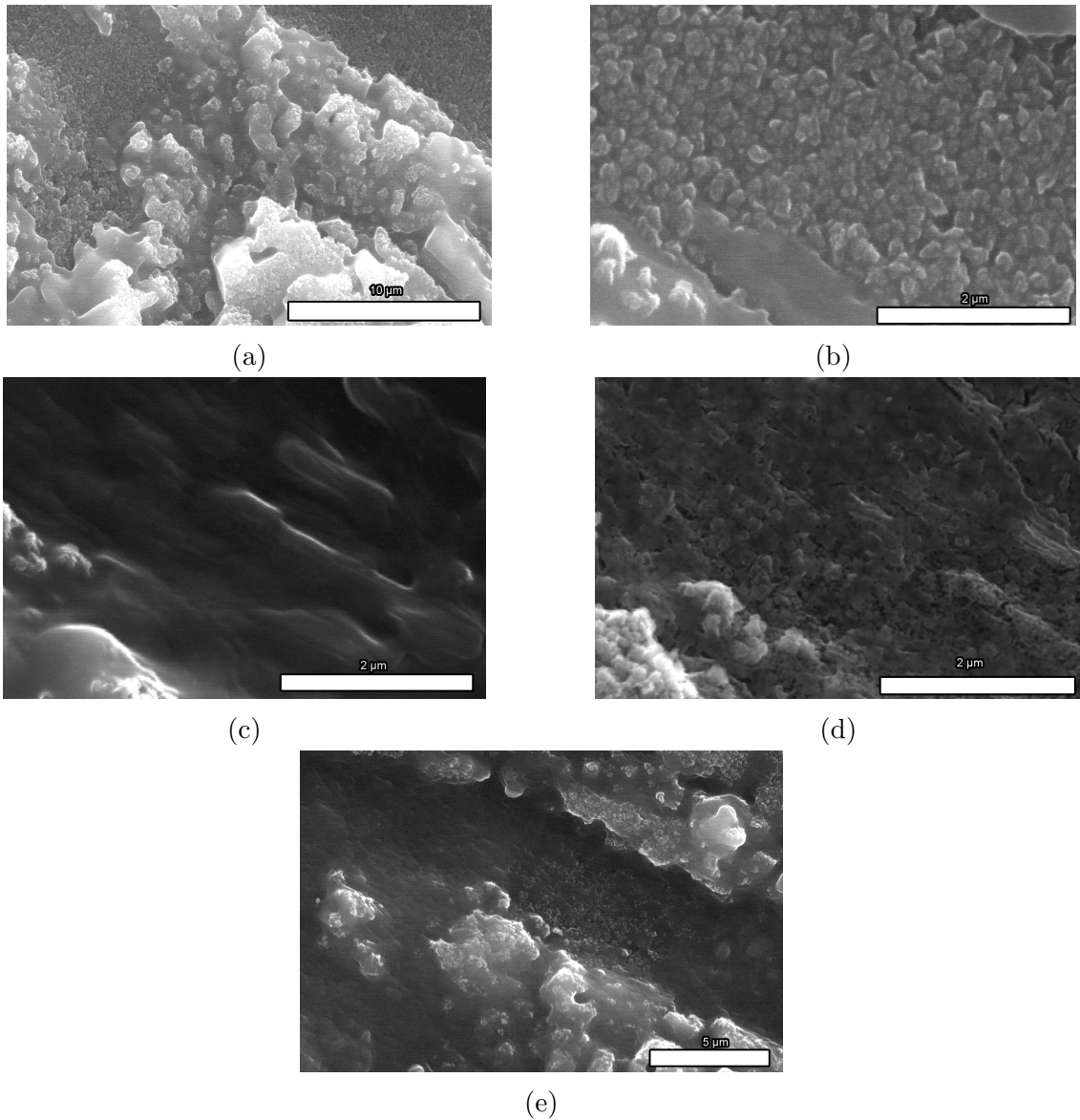


Figure 3.12: SEM micrographs of zeolite X wet seed at (a) 100%RH, (b) 90%RH, (c) 50%RH, (d) 0%RH. (e) shows the microstructure after humidity was increased back to 100%RH

# Chapter 4

## Identifying nucleation seeds

*This chapter is based on the paper “Effect of TiO<sub>2</sub> and ZnO nanopowders on metakaolin-NaOH geopolymers”, Proceedings of the 41st International Conference on Advanced Ceramics and Composites, Ceramic Engineering and Science Proceedings, 38(3), pp. 251-262, 2018. Experimental data on synthesized zeolite seeds has been added, and the discussion has been modified to include the new data. Other minor changes are present throughout the chapter.*

### 4.1 Introduction

An aluminosilicate precursor such as metakaolin yields a three-dimensional aluminosilicate structure with short-ranged, ordered framework upon reaction (often referred as alkali activation) with hydroxide or silicate solution [47]. The proposed reaction mechanism for geopolymerization involve a dissolution step [8, 32] where silicate and aluminate species are released into solution, followed by a polymerization process where polymerized silicate species along with aluminosilicate oligomers are formed [16]. These oligomers further polymerize and ultimately form a three-dimensional amorphous framework [16]. Zeolite phases can also be detected in such systems given certain environmental conditions and age of specimens [81, 84]. Multiple review articles and descriptions of the overall geopolymer mechanism exist on this topic [7–9, 28].

Thus, it is established that a phase transformation occurs from the dissolved silicate and aluminate species in the solution to the final hardened binder. In the context of alkali-activated materials, this transformation is believed to be a nucleation and growth

controlled process [19, 84]. Nucleation and growth is a typical example of a discontinuous, liquid-solid phase transformation, where the new phase formed has drastically different properties from its parent but the change is highly local. The new phase consequently grows spatially out of these small nuclei [62]. Thus, adding nucleation seeds offers promise in controlling reaction kinetics and early age properties, as has been summarized by Kawashima et al. in cement based systems [67]. Addition of tobermorite and xonotlite (crystalline analogues of C-S-H, the primary reaction product of cement hydration) has been observed to increase the rate of hydration of portland cement pastes [65]. The structure of the reaction product at the nanoscale can also be potentially modified due to the presence of seeds. For example, addition of different types of synthesized C-S-H to hydrating tri-calcium silicate ( $\text{C}_3\text{S}$ ) systems has been reported to influence the nano-structure and composition of the reaction product [66]. Furthermore, presence of C-S-H is shown to accelerate the reaction kinetics and increase early age strength of alkali activated slag [72].

Addition of nucleation seeds can also prove whether a reaction is nucleation and growth controlled or dissolution controlled as in the case of the latter, the addition will have little or no effect on the reaction kinetics. By adding nucleation seeds (nano  $\text{Al}_2\text{O}_3$ ,  $\text{ZnO}$  and  $\text{ZrO}_2$ ) to two different geopolymeric binders, a Class F fly ash geopolymer activated through  $\text{NaOH}$  [12] and a binder made by mixing geothermal silica with sodium aluminate [13], it has been proved experimentally that the formation of geopolymeric binder could involve nucleation. The kinetics of the reaction was seen to be accelerated in both cases and the former study reported that the addition of nano-alumina in very small dosages ( $\ll 1\%$  by wt. of precursor) can influence the nature of the product being formed. Adding seeds to the geothermal silica-sodium aluminate binder resulted in a refined microstructure, which consequently led to improvements in compressive strength. Furthermore, elemental analysis revealed that the  $\text{Si}/\text{Al}$  and  $\text{Na}/\text{Al}$  ratios of the product was statistically different between the control and seeded sample, demonstrating the potential for seeds to control the nature of the reaction product.

In summary, addition of nucleation seeds provides i) an opportunity to verify whether a reaction is nucleation controlled, ii) a potential to refine the microstructure of the binder, and iii) a chance to influence the nano-structure of the final reaction product. However, to the best of the author's knowledge, any information on the nucleation seeding in metakaolin based geopolymers is lacking in the published literature. In this study, geopolymers were prepared by adding sodium hydroxide to metakaolin. Nano-TiO<sub>2</sub> (anatase), SiO<sub>2</sub>, zeolite A and zeolite X were added as potential seeding agents in low dosages. Zeolite A and zeolite X were used since they were identified as crystalline analogues of the metakaolin-NaOH geopolymers considered in this study. Influence of these additives on the reaction kinetics was observed through isothermal calorimetry. Selective dissolution using hydrochloric acid (HCl) extractions were performed at 4h, 24h and 144h to quantify the amount of unreacted precursor and results were correlated with the reaction kinetics data obtained from isothermal calorimetry.

## 4.2 Experimental Methods

### 4.2.1 Materials and Sample Preparation

Metakaolin (MK) was procured from BASF chemicals, with XRF composition being listed in Table 4.1. Median particle size and surface area was reported to be 1.21µm and 14.2m<sup>2</sup>/g respectively, by the manufacturer. Sodium hydroxide pellets were supplied by Fisher chemicals with a purity ≥97% and subsequently, made into solutions at the required concentration. Nano-pure water obtained from a Milli-Q water purification system (EMD Millipore, USA) was used throughout the study. All materials were stored at a temperature of 22°C. The metakaolin geopolymers were prepared with a 1:1:1.9:13.6 (Na<sub>2</sub>O:Al<sub>2</sub>O<sub>3</sub>:SiO<sub>2</sub>:H<sub>2</sub>O) molar stoichiometry, using a motorized shear mixer (DrinkMaster, Hamilton Beach). A typical mix consisted of 20g metakaolin, 7.15g NaOH pellets and 20.26g water. NaOH solution was prepared beforehand, and allowed to cool down to room

temperature prior to mixing.

Metakaolin powder was added to sodium hydroxide in a plastic mixing cup and mixed for four minutes. The cup was sealed off and kept at 22°C prior to testing. Nanopowders were dispersed through a probe sonicator (Fisher Scientific, Model 505) in the sodium hydroxide solution prior to mixing. Henceforth, the metakaolin geopolymers prepared are denoted as “MK-NaOH” or “Control”. Dosage of seed additions are reported in % wt. of metakaolin within the mix.

Table 4.1: XRF Analysis of Metakaolin

SiO <sub>2</sub>	Al <sub>2</sub> O <sub>3</sub>	Na <sub>2</sub> O	K <sub>2</sub> O	TiO <sub>2</sub>	Fe <sub>2</sub> O <sub>3</sub>	CaO	MgO	P <sub>2</sub> O <sub>5</sub>	LOI (%)
52.3	45.2	0.22	0.15	1.74	0.42	0.04	0.04	0.08	0.79

#### 4.2.2 Potential seeding agents

TiO<sub>2</sub>, SiO<sub>2</sub> and ZnO nanopowders were procured from US Research Nanomaterials. The nanopowders were added in dosages of 1% and 5% weight of metakaolin in the mix, unless otherwise specified. Although seeds have been observed to be added at levels beyond 5% [18, 65, 67], the authors believe a small quantity of nano-sized particles with high surface area should provide enough sites for heterogeneous nucleation [12, 13, 72]. It should be noted that these oxides have been shown to act as nucleation seeds in cement, low calcium, and high calcium alkali-activated binders [12–14, 18].

Zeolites A and X were synthesized and characterized as described in Chapter 3. Zeolite X was used as a wet seed, and water from the wet seed was subtracted from NaOH solution to ensure the overall mix stoichiometry remains the same. The amount of water to be subtracted was taken to be equal to the mass loss obtained by drying the zeolite X wet seed at 160°C for 24h. A similar procedure has been adopted by Hubler et al., [72] while adding wet, synthesized C-S-H seeds in alkali-activated slag binders. Zeolite A was used in the powdered form.

#### **4.2.3 Isothermal Calorimetry**

After MK-NaOH mixtures were prepared, they were transferred into 20 mL glass ampoules and kept in a TAM Air 8 channel micro-calorimeter. Baseline data was collected for thirty minutes after the signal was stabilized. The samples were then inserted in the calorimeter within 5 minutes after mixing. First 45 minutes of data was discarded since the mixing was done outside of the calorimeter, and the initial rate of heat release can be partly attributed to frictional heat generated while inserting the ampoules. Three replicates for each sample was run, and the results came out to be identical. Therefore, only one curve from each sample is presented in this thesis. The rate of heat and total heat released was normalized to the total amount of geopolymer paste in the ampoule. The time  $t=0$  in the heat evolution curves denotes the time at which samples were inserted in the calorimeter and subsequently, data was recorded every second.

#### **4.2.4 HCl Extraction**

The degree of reaction or the amount of product formed in alkali activated binders has been measured quantitatively using selective dissolution techniques previously [26]. In particular, HCl solutions have been known to remove products generated through alkali-activated binders [85]. To carry out the dissolution process, the reaction needs to be stopped and all free water has to be removed. For this purpose, a solvent extraction method was employed. Geopolymers were crushed with an pestle and mortar at the required age (4h, 24h and 144h) with a 1:1 mixture of acetone and methanol (by volume). While solvent extractions have been known to stop the geopolymer reaction, it has also been reported that the presence of soluble silicates can precipitate silica along with the geopolymers [86]. To ensure that there is no such precipitation, MK-NaOH powders were washed with water prior to the solvent extraction in a manner described by Chen et al. [86]. However, FTIR spectra of powders without and with the water wash was seen to be the same, owing to which the solvent extraction method without prior washing, was used throughout this study. Finally,

0.4g of a powder thus obtained was stirred in 100 ml of a 1:20 HCl solution for 3 hours to remove all reaction products [26]. Subsequently, the solution was vacuum filtered through a Whatman Grade 1 filter paper in a Buchner funnel and flushed twice with nano-pure water. The funnel was then dried at 105°C and the mass loss was recorded. The residue was verified to be metakaolin using FTIR and the mass loss data was used to compute the percent of unreacted metakaolin in a sample. Unreacted metakaolin was calculated by averaging values obtained from four separate extractions. Standard deviation from average is reported as uncertainty.

## 4.3 Results and Discussion

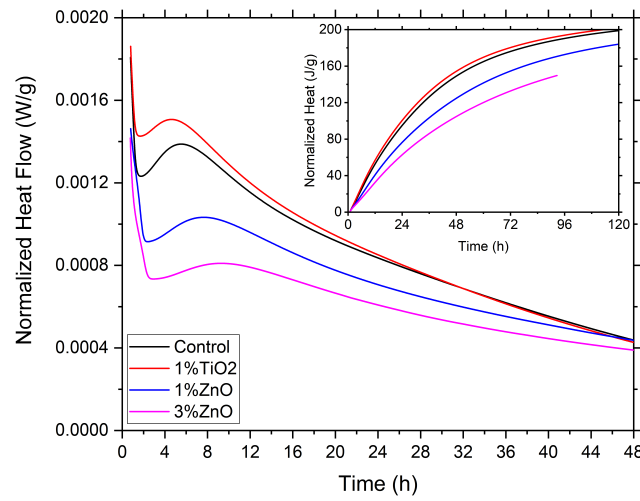
### 4.3.1 Effect of TiO<sub>2</sub> addition MK-NaOH reaction kinetics

Figure 4.1a shows the effect of addition of 1% TiO<sub>2</sub> and ZnO to the control MK-NaOH sample. The control specimen has two distinct peaks in the time-frame of data presented. As part of the experimental model presented by Zhang et al., [50] the first peak (within the first hour) is attributed to the initial heat released from the dissolution of metakaolin. Subsequently the reaction goes through an apparent induction period, followed by a second peak (seen within 5-6 hours). This peak is attributed to the polymerization process that is known to occur within alkali activated binders [50]. Addition of TiO<sub>2</sub> shows two changes compared to control, with the first being rate of heat released increases up to the first 24 hours. The second feature is harder to distinguish, but there is a slight decrease in the time at which the second peak takes place. It should be also noted that further increase in the dosage of TiO<sub>2</sub> did not cause any additional change in the reaction kinetics. While the changes observed through calorimetry are not as dramatic compared to what was observed by Rees et al. [12], the effect of TiO<sub>2</sub> addition on the reaction kinetics is undeniable. Possible explanation of the effect of TiO<sub>2</sub> addition on the reaction kinetics of MK-NaOH is carefully considered here.

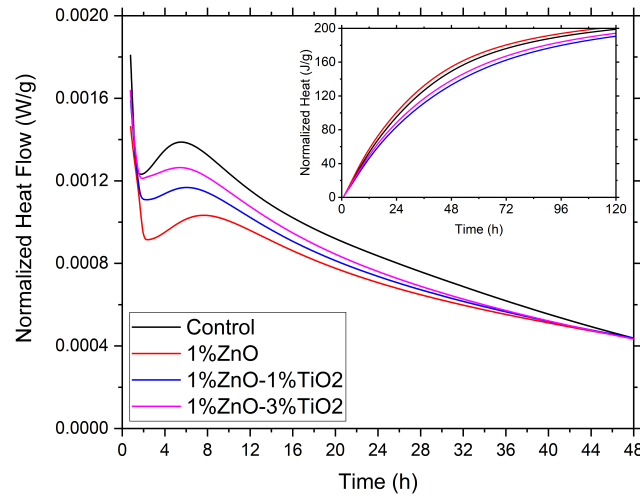
It is unlikely that  $\text{TiO}_2$  directly participated in any chemical reaction since it is known to be inert in alkaline media [18] and the amount added is very small. On the other hand, if the rate of reaction at the early age is controlled by the availability of nucleation sites, addition of  $\text{TiO}_2$  nano-particles was expected to reduce or even eliminate the drop in reaction rate observed between 1-2h. For example, addition of a small quantity (0.5% - 4% by weight of  $\text{C}_3\text{S}$ ) of synthesized C-S-H gel accelerates hydration of tricalcium silicate and virtually eliminates the induction period [14]. This result strongly indicated that the formation of C-S-H is autocatalytic. The lack of pronounced effect of  $\text{TiO}_2$  addition on the length of the induction period could indicate that the availability of nucleation sites is not a rate limiting factor, when geopolymer is synthesized from metakaolin owing to its extremely high surface area ( $14.2 \text{ m}^2/\text{g}$ , which is around forty times higher than typical ASTM Type 1 cement). Another possibility is that the formation of geopolymeric sodium aluminosilicate hydrate (N-A-S-H) is autocatalytic [84]. Therefore,  $\text{TiO}_2$  nano-particles offer limited opportunity for the nucleation of N-A-S-H on its surface which in turn provide more suitable nucleation sites for subsequent N-A-S-H formation. Similar phenomenon is reported when silica fume is added to  $\text{C}_3\text{S}$  based binders [14]. It is believed that pozzolanic C-S-H forms slowly on the surface of the silica fume and subsequently auto-catalyzes the reaction. Thus, a slow acceleration is observed since additional nucleation sites form gradually throughout the early period of hydration instead of being immediately available at the time of mixing. Similar behavior is observed in Figure 4.1a, where an increase in the peak heat of hydration is observed without any change in the induction period. Lastly, there is always a possibility that the lack of pronounced effect of  $\text{TiO}_2$  addition could be attributed to the poor dispersion of  $\text{TiO}_2$  as mentioned earlier. In the subsequent sections, it will be demonstrated that the effect of a seed appears to depend on its surface area. Therefore, poor dispersion limits any possible nucleation effect that  $\text{TiO}_2$  can have on geopolymer formation. Increasing dosage of  $\text{TiO}_2$  also does not serve any purpose since large aggregates have low specific surface areas, which do not provide enough nucleation sites to cause drastic acceleration in the rate of reaction. However, this may not be entirely true, based on effects of  $\text{TiO}_2$  observed in the

presence of ZnO as described below.

To verify that TiO<sub>2</sub> acts as a nucleation seed in MK-NaOH geopolymers, it was used in combination with ZnO nanoparticles. In cement-based systems, ZnO is believed to poison nucleation sites which ultimately causes retardation [61]. Ataie et al. [61] observed that the retarding effect of ZnO on cement hydration can be reduced by addition of a silicon rich, finely divided, highly amorphous rice and wheat husk ash which are verified to act as nucleation sites for C-S-H. Following similar analogy, ZnO was added at 1% and 3% by wt. of MK-NaOH. Figure 4.1 clearly shows that the addition of 1%ZnO has a retarding effect on the MK-NaOH system. It decreases the rate of heat release and delays the appearance of the second peak. The figure also illustrates that the retardation increases with the increase in dosage of ZnO. In a parallel study carried out by the authors, addition of ZnO to an alkali activated fly-ash slag binder also caused similar retardation. The evidence of ZnO nanoparticles being a retarder does contradict the accelerating effect observed by Hajimohammadi et al. [13]. However, these observations could stem from differences in the reaction mechanism when different precursors are used. For example, addition of Al<sub>2</sub>O<sub>3</sub> nanoparticles to Class F fly ash activated through sodium hydroxide has been reported to accelerate the reaction significantly [12]. However, the same did not show any effect on MK-NaOH. When 1%TiO<sub>2</sub> was added to the system containing 1%ZnO, it was observed that the extent of retardation is arrested to some extent (illustrated in Figure 4.1b). Increasing the dosage of TiO<sub>2</sub> to 3% further reduces the retardation, compared to 1%TiO<sub>2</sub>. Since ZnO is known to poison nucleation sites, the fact that TiO<sub>2</sub> can reverse the action of ZnO provides indirect proof that it is indeed acting as a nucleation seed.



(a)



(b)

Figure 4.1: Rate of heat evolution from MK-NaOH (control) binders, with (a) 1%  $\text{TiO}_2$ , 1% $\text{ZnO}$  and 3% $\text{ZnO}$  and (b) a combination of  $\text{TiO}_2$  and  $\text{ZnO}$  nanopowders

#### 4.3.2 Effect of $\text{SiO}_2$ addition on MK-NaOH reaction kinetics

Figure 4.2 shows the effect of adding 1% and 5%  $\text{SiO}_2$  to MK-NaOH . The addition of 1%  $\text{SiO}_2$  shows an increase in the rate of heat released up to the first 24 hours, but no

changes were observed in the time at which the second peak ( $T_{peak,2}$ )<sup>1</sup> is observed. However, unlike  $\text{TiO}_2$ , the addition of  $\text{SiO}_2$  at higher dosages increased the rate of heat evolution drastically. The time at which the second peak is observed ( $T_{peak,2}$ ) reduced by  $\approx 1\text{h}$  upon the addition of 5%  $\text{SiO}_2$ . For reference, adding 5%  $\text{SiO}_2$  results in a Si/Al ratio of 1.07 within the geopolymers (as compared to 0.98 in MK-NaOH).

To interpret this behavior, a mix equivalent to MK-NaOH-5%  $\text{SiO}_2$  mix was prepared using soluble silica (RU Sodium Silicate, PQ Corp) instead of silica nanopowder. Figure 4.3 shows that the rate of heat evolution of this equivalent mix is similar to that of MK-NaOH-5%  $\text{SiO}_2$ . Therefore, it is clear that silica nanopowders are dissolving in NaOH solution. This behavior is expected since sodium silicate solutions are often prepared from solid silica sources like fumed silica dissolved in NaOH. The dramatic increase in rate of heat evolution upon adding 5%  $\text{SiO}_2$  was unexpected since isothermal calorimetry data from literature has reported that increasing the modulus of activator solution decreases the rate of heat evolution [51]. Possible explanations for this acceleration are discussed subsequently.

The addition of external seeds as nuclei for a reaction to proceed lowers the activation energy barrier and increases the rate of reaction [62]. The acceleration observed in cement hydration upon the addition of nanoparticles have been linked to a nucleation seeding effect [14, 18, 63, 65, 66]. Polycondensation processes, which lead to the formation and growth of aluminosilicate network in geopolymers have been observed to contribute majorly to the heat released after the first peak in geopolymORIZATION [29, 54]. On the basis of the observations made when C-S-H gel is used as a seeding agent in  $\text{C}_3\text{S}$  hydration, any nucleation effect should increase the  $R_{peak,2}$  and decrease  $T_{peak,2}$ . These expectations due to nucleation, match the effects observed upon addition of  $\text{SiO}_2$ , as described in the first paragraph of this section. In addition,  $R_{peak,2}$  was seen to increase further upon increasing the dosage of  $\text{SiO}_2$  from 1% to 5%, which is indicative of the fact that more nucleation sites are present, which subsequently accelerates the reaction further. Therefore, the changes observed in Figure 4.2 indicates that

---

<sup>1</sup>with reference to Figure 2.7

the acceleration in rate of reaction is a consequence of  $\text{SiO}_2$  particles providing nucleation sites.

The concept of silica species in solution acting as nucleation sites for silica polymerization and growth has been described in literature by Iler [35]. At a  $\text{pH} > 7$ , monomeric silica species condenses to form dimers and small oligomers. The polymerization route maximizes the formation of  $\text{Si}-\text{O}-\text{Si}$  bonds over  $\text{Si}-\text{OH}$  bonds. Therefore, small cyclic species form at the earliest stages and these cyclic (or spherical) units serve as nuclei for further polymerization. For gel growth, some of the smaller silica units dissolve and polymerize with the larger silica species. Therefore, the number of cyclic silica polymers keep decreasing, and the average size of these polymers keep increasing. The formation of such cyclic silica species have been reported by North and Swaddle, by carrying out NMR spectroscopy on dilute aluminosilicate solutions at low temperatures ( $-9^\circ\text{C}$ ) [56]. Therefore, it can be argued that geopolymers occurs with small cyclic silica species acting as nuclei for growth of an aluminosilicate network. Hence, a nucleation effect could be the reason behind the acceleration seen upon adding  $\text{SiO}_2$  nanoparticles to MK-NaOH.

A second interpretation of the effects of adding 5%  $\text{SiO}_2$  can be obtained from the hypothesis of product formation on (or near) the surface of metakaolin. This product is believed to act as a barrier to dissolution and slows down the rate of reaction [15, 87] for metakaolin geopolymers after  $T_{peak,2}$ . A similar hypothesis has been proposed in the case of geopolymers derived from geothermal silica and fly ash [12, 58]. Alumina and silica species dissolved from the precursor appear to react and form a barrier on precursor surface, which consequently results in slower dissolution. Formation of product on or near the surface of metakaolin has been suggested by Chen et al., based on results from NMR spectroscopy [28]. The consequences of the barrier formation on reaction kinetics was not described in their study. In this study, small quantities of soluble silica (as in the case of adding 5%  $\text{SiO}_2$ ) is hypothesized to react with alumina being dissolved from metakaolin. Increased dissolution was noted (discussed in subsequent sections), which indicated that the barrier formation on

the surface of metakaolin was prevented. The resulting aluminosilicate products from the reaction of silica in activator, and alumina from precursor have also been hypothesized to serve as nucleation sites for geopolymers growth [59]. While no direct evidence of nucleation was provided in their study, it is likely that this hypothesis is correct. Once again, in analogy to the behavior of nano-silica or micro-silica in cement hydration [14], the slight decrease of 1 hour in the value of  $T_{peak,2}$  upon 5%  $\text{SiO}_2$  addition shows that nucleation sites are gradually forming instead of being available for geopolymers growth immediately. In addition, the previous observation of increasing microstructural homogeneity with increasing Si/Al ratios in metakaolin geopolymers (Figure 2.10) [20] can now be explained differently. The presence of nucleation sites provides site for product growth throughout the geopolymers pore space, which can cause the significant increase in microstructural homogeneity.

While these two perspectives provide a reason to as to why does silica accelerate geopolymers reaction, there is no explanation to why would a nucleation seed reduce the rate of reaction. As mentioned earlier, adding soluble silica reduces the rate of reaction [51], and Figure 4.2 also shows that the rate of reaction for MK-NaOH-5% $\text{SiO}_2$  slows down after  $\approx 15\text{h}$ , when compared to control. In literature, the slower rate of reaction upon adding soluble silica has been attributed to lability of aluminosilicate species in solution [20]. However, the silica polymerization model presented by Iler can be used to explain the retardation observed upon addition of silica to metakaolin geopolymers. To elaborate, a third geopolymers mix with higher silica content than the two mixes in Figure 4.2 was prepared with soluble silica. The mix is equivalent to adding  $\text{SiO}_2$  at a dosage  $\approx 50\%$  wt. of metakaolin used in MK-NaOH, resulting in a geopolymers with  $\text{SiO}_2/\text{Al}_2\text{O}_3 = 3.80$ , and calorimetry results for this mix is presented in Figure 4.3. It is observed that upon adding of more soluble silica (resulting in  $\text{SiO}_2/\text{Al}_2\text{O}_3 = 3.80$ ), the rate of heat evolution and total heat evolution is seen to be less than the control mix upto a period of 120 hours.

Iler's model describes that silica polymerization and growth takes place by smaller silica species dissolving and attaching to the larger growing nuclei [35]. Beyond a size of 5nm,

colloidal silica in solution tend to dissolve slowly, and therefore, silica growth is reduced drastically [35]. It is a well known fact that increasing concentration of soluble silica in alkaline solutions (or increase in silica modulus i.e. molar  $\text{SiO}_2/\text{Na}_2\text{O}$ ), leads to silica species becoming more and more polymerized [40]. Sodium silicate solutions with a modulus of 0.5 have been reported to possess 85% of silica in  $\text{Q}^0$  and  $\text{Q}^1$  states [20]. Silica modulus of activator solution in the case of 5%  $\text{SiO}_2$  addition is  $\approx 0.2$ , which confirms that monomeric and dimeric silica species are the majority species in solution. Therefore, in MK-NaOH-5% $\text{SiO}_2$ , rapid reaction is observed because the monomeric and dimeric silica can serve as nuclei and help in polymerization and growth of the aluminosilicate. When the available smaller silica is depleted, aluminosilicate growth slows down which is reflected in the reduced rate of reaction after  $t > 15\text{h}$  (when compared to control).

The activator solution in the case of MK-NaOH-5% $\text{SiO}_2$  has a modulus close to 2.0, where the total  $\text{Q}^0$  and  $\text{Q}^1$  species is believed to be around 15% [20, 40]. Colloidal silica is present throughout the pore solution, and therefore, there is no shortage of nucleation sites in the binder. However, since the species are more polymerized, the process of growth slows down since larger silica species do not dissolve easily. Therefore, the reaction rate in this high-silica geopolymers is slower when compared geopolymers with  $\text{SiO}_2/\text{Al}_2\text{O}_3 = 1.96$  (when  $t > 15\text{h}$ ) and 2.14. This observation proves that soluble silica in activator solution controls the geopolymer reaction by a) providing nucleation sites and b) controlling the growth rate of product.

Further proof of silica acting as a nucleation seed can be obtained from the synthesis of aluminosilicate gel precursors for zeolites. Harvey and Glasser [38] have observed that the formation and growth of these aluminosilicate gels are controlled by the amount of nuclei and “nutrient”. DLS results of aluminosilicate gel formation revealed that low silica and high alkali gels follow a clear nucleation and growth limited process, whereas high silica solutions form gels easily but exhibit a slow growth. Therefore, it was concluded that silicate species (especially monomers) act as nuclei for gel growth. On the other hand,

dissolved alumina was observed to complex preferentially with large silicate species. Once bound to these species, further polymerization and growth of aluminosilicate species slow down since Si–O–Si bonds have to be broken, while the Si–O–Al bonds are not cleaved in alkaline media [38]. Therefore, the availability of aluminum controls the growth of gel; and “nutrient” refers to aluminum in this case. Through this discussion, the role of soluble silica in geopolymmerization becomes very clear. In small quantities, these silicates act as nuclei and a nucleation-controlled step exists in the reaction mechanism. However, upon adding excess silica, the mechanism switches completely to a growth-controlled system where large silica species slowly polymerize. Aluminum availability controls the rate at which the aluminosilicate growth takes place.

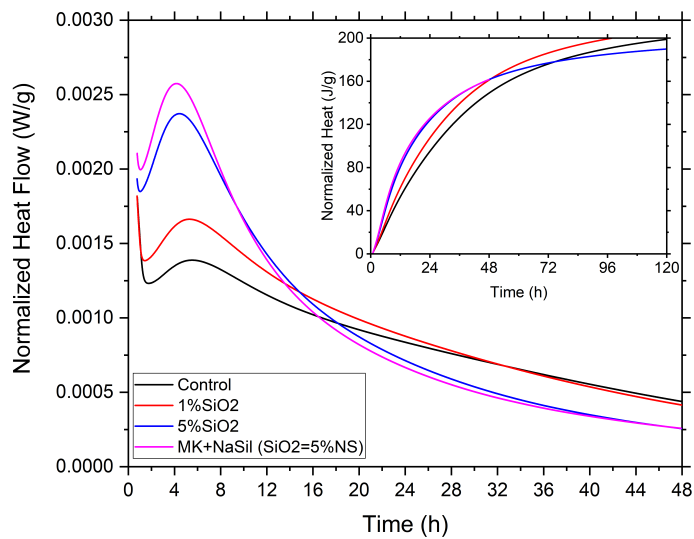


Figure 4.2: Rate of heat evolution from MK-NaOH (control) binders, with 1% and 5% SiO<sub>2</sub>. Geopolymer paste equivalent to MK-NaOH-5%NS, prepared with metakaolin-sodium silicate is denoted as MK+NaSil(SiO<sub>2</sub>=5%NS)

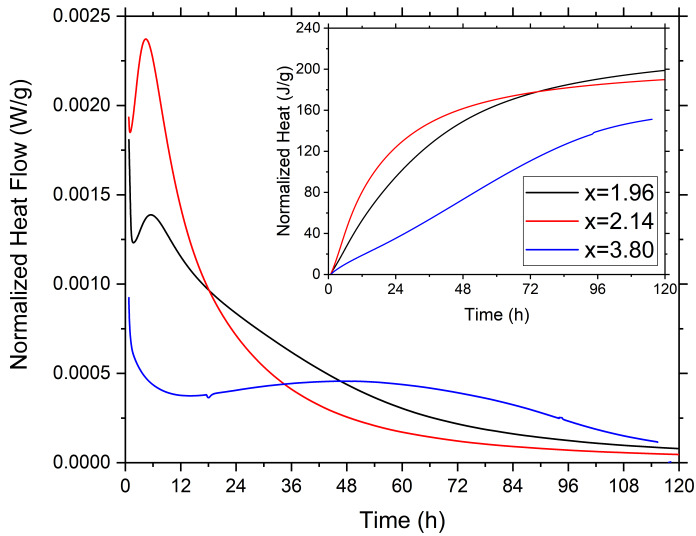


Figure 4.3: Rate of heat evolution from metakaolin geopolymers, with a general stoichiometry of  $1\text{Na}_2\text{O}:1\text{Al}_2\text{O}_3:x\text{SiO}_2:13.6\text{H}_2\text{O}$ , with  $x$  reported in the legend

#### 4.3.3 Effect of zeolite addition on MK-NaOH reaction kinetics

Figure 4.4 shows the effect of adding 1% Zeolite A and Zeolite X to MK-NaOH geopolymers. In both cases, the rate of heat evolution increased slightly ( $R_{peak,2}$ ) and no other changes were evident. Adding zeolite seeds at higher dosages was seen to accelerate the reaction further. With analogy to the previous discussion with  $\text{SiO}_2$  addition, it can be argued that this observation indicates that the zeolites are acting as nucleation seeds. Upon adding 5% Zeolite X,  $T_{peak,2}$  was reduced by 2 hours which is significantly more than the reduction seen upon adding 5%NS, which indicates zeolite X is acting as a better nucleation seed than  $\text{SiO}_2$ . Zeolites are known to be extremely stable in alkaline media [88, 89], and therefore should not accelerate the reaction by dissolving and forming silica species. Therefore, this observation is strongly indicative of an autocatalytic effect that has been claimed to be present in geopolymerization [15, 16]. It should be noted that the  $R_{peak,2}$  for 5% Zeolite X addition is still less than that seen in the case of 5%  $\text{SiO}_2$ , while the total heat evolution in the sample is greater than that of control till 5 days.

The differences observed between the Zeolite X and Zeolite A seeded binders could be explained on the basis of the surface areas of the respective nanopowders. Zeolite A was estimated to have a BET surface area of  $32\text{m}^2/\text{g}$  compared to  $229\text{m}^2/\text{g}$  for Zeolite X. DLS results confirmed that the zeolites were in a dispersed state in NaOH activator solution, and therefore, the trend in surface areas can be regarded to be valid in solution as well. Since higher surface area implies more nucleation sites, zeolite X should accelerate the geopolymers reaction more than zeolite A, as seen. However, it should also be noted that zeolite X was semi-crystalline (XRD Rietveld indicates 14% crystallinity). Qualitatively, SEM micrographs indicated zeolite A formed well defined cubic crystals, and appeared to be more crystalline than zeolite X. Hence, it is also possible that the chemistry of the semi-crystalline zeolite X is more similar to the amorphous geopolymers and can influence the geopolymers reaction to a greater extent than zeolite A. Nevertheless, owing to the pronounced effects of zeolite X, further discussion does not include the effects of zeolite A.

In Chapter 3, zeolite X was revealed to possess a semi-crystalline structure. Additional calorimetry was run by using the amorphous aluminosilicate gel precursor to zeolite X as seed. The gel was obtained by filtering out the aluminosilicate solution (composition reported in Chapter 3) after 24h stirring at room temperature. Subsequently, it was dried at  $105^\circ\text{C}$ , sieved through a  $250\mu\text{m}$  mesh and dispersed through probe sonication. Adding the amorphous precursor to MK-NaOH increased  $R_{peak,2}$  but did not change  $T_{peak,2}$ . IR spectra of the amorphous gel indicated that it has less aluminum substitution compared to the semi-crystalline zeolite, i.e. the amorphous precursor has greater Si–O–Si bonds compared to the semi-crystalline zeolite. As observed in another study [38], Si–O–Si bonds breakdown in alkaline media, and lead to the formation of soluble silica species. The discussion in Section 4.3.2 demonstrated that these silica species can provide nucleation sites for the geopolymers product to grow, which could be the explanation to the increase in rate of reaction. Crystalline zeolite X was also procured as a commercial molecular sieve (Type 13X, Alfa Aesar) and used as a seed. The effects of addition of these materials to MK-NaOH are illustrated in Figure 4.5. The addition of crystalline zeolite X did not have a

significant effect on calorimetry, and on the contrary a slight retardation was observed. This could be because the crystal size in NaOH solution was observed to be  $\approx 600\text{nm}$  through DLS, which is much higher than the particle sizes of synthesized zeolite X. Therefore, the crystalline zeolite should have much lesser surface area, and consequently should not affect the geopolymmerization kinetics significantly.

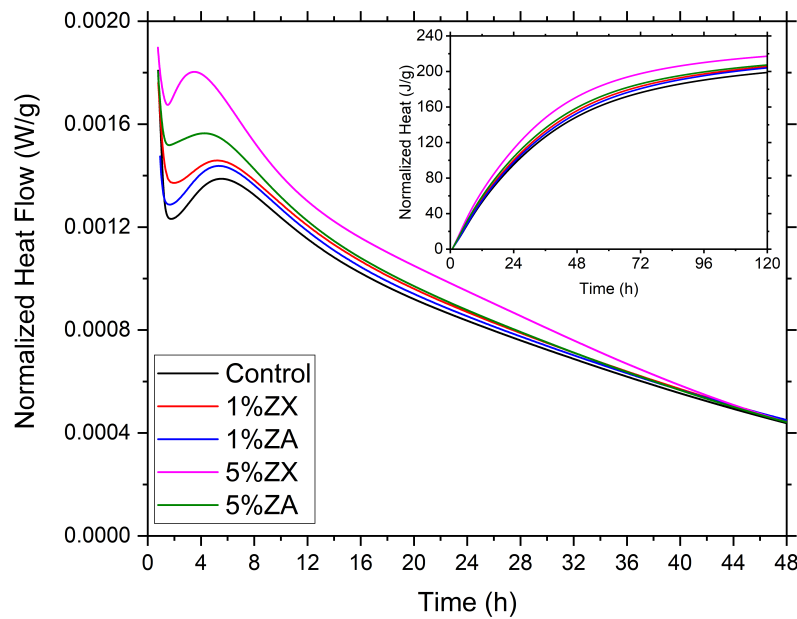


Figure 4.4: Rate of heat evolution from MK-NaOH (control) binders, with 1% and 5% Zeolite X and A

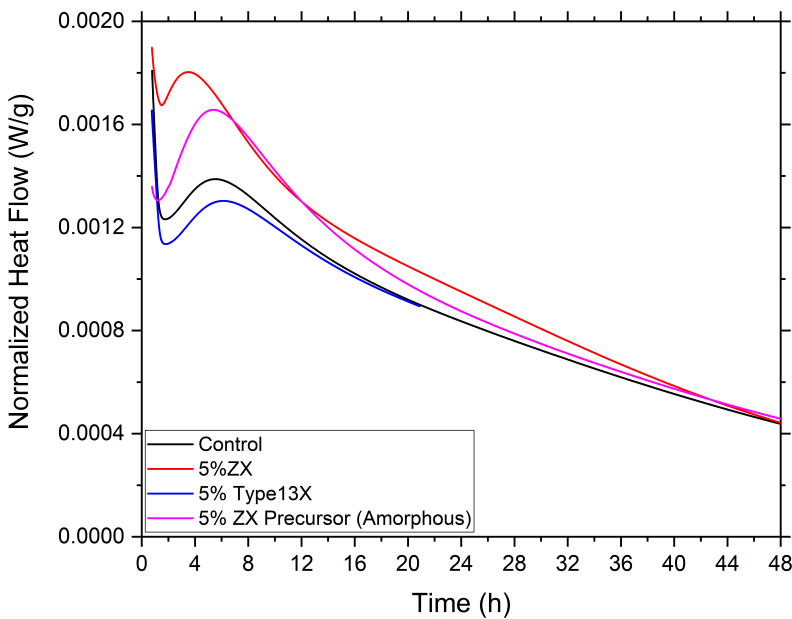


Figure 4.5: Rate of heat evolution from MK-NaOH (control) binders, 5% Zeolite X, 5% Zeolite X precursor and 5% Type 13X

#### 4.3.4 Effect of nanoparticles on degree of reaction

Amount of unreacted metakaolin at various ages is estimated through HCl extraction at 4, 24 and 144h. The discussion in the preceding sections strongly indicate  $\text{TiO}_2$ ,  $\text{SiO}_2$  and zeolite X are acting as nucleation seeds. The increased dissolution that is observed at 4h therefore provides additional indirect evidence that these nanopowders are acting as nucleation seeds. Beyond 4h, metakaolin dissolution is the same as that of control, when considering  $\text{TiO}_2$  and zeolite X nanopowders. This indicates that the nucleation limited stage within MK-NaOH geopolymmerization is very narrow (temporally). Post nucleation, the rate of reaction is determined by the rate of product growth. Polymerization and gel growth of aluminosilicate is controlled by the availability of small silica species and alumina. Since  $\text{TiO}_2$  and zeolite X are believed to act as nuclei only, they are not expected to accelerate geopolymers growth.

On the other hand, silica species can accelerate metakaolin dissolution by providing nucleation sites, and also drive further growth of product, by enabling polymerization of silica species from solution. Therefore, even in a growth controlled state, silica can promote further dissolution of metakaolin (provided there is availability of aluminum species in solution [38]), as observed in Figure 4.6a. It is also interesting to note that while zeolite X appears to act as a better seeding agent than  $\text{TiO}_2$ , based on the rate of heat evolution data in Figure 4.6b, the extent of dissolution caused by both nanopowders are same by 24h as seen from HCl dissolution data. This observation is consistent with the earlier hypothesis of the nucleation controlled step (in metakaolin geopolymers) being a small temporal region in the overall reaction. In addition, it is interesting to note that seeding with 5% zeolite X causes  $T_{peak,2}$  to occur  $\approx 1\text{h}$  prior, compared to seeding with 5%  $\text{SiO}_2$ . This behavior indicates that zeolite X nano-particles provide kinetically favorable nucleation sites, and acts as “better” seed than  $\text{SiO}_2$ . It should be noted that the discussion in Sec. 4.3.2 hypothesized that the silica particles were not the actual nucleating sites; the nano-silica reacts to form small aluminosilicate oligomers, which subsequently act as nucleation sites. The behavior exhibited by zeolite X provides proof of this hypothesis, since the zeolite is an aluminosilicate. Therefore, on the basis of the rate of heat evolution in the presence and absence of seeding agents, the nucleation controlled step appears to occupy the temporal region from 2h onwards, till 24h, for the MK-NaOH control mix.

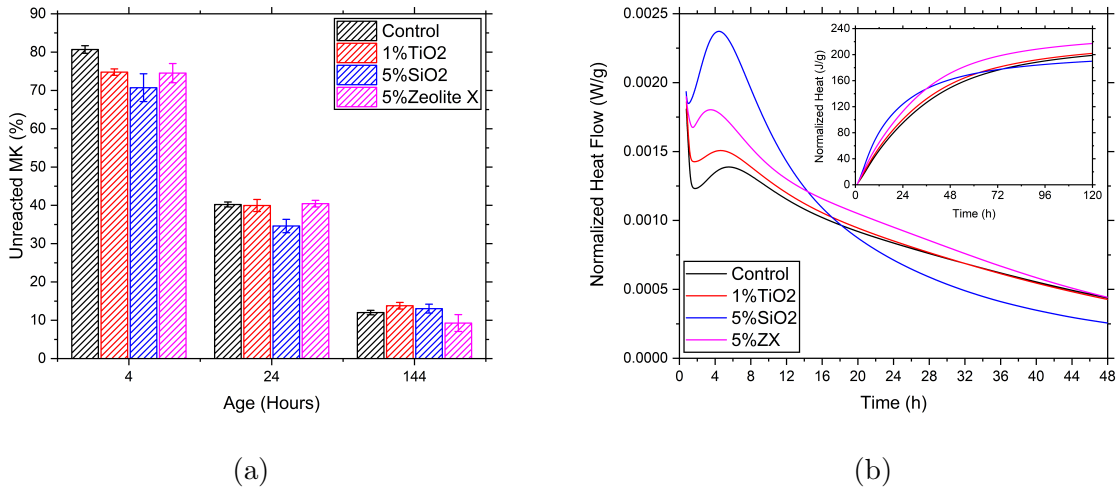


Figure 4.6: (a) Unreacted metakaolin at 4h, 24h and 144h in seeded and un-seeded MK-NaOH binders, (b) Calorimetry data showing effects of TiO<sub>2</sub>, SiO<sub>2</sub> and zeolite X nanopowders

#### 4.4 Conclusions

Insights into nucleation seeding, as obtained from isothermal calorimetry and HCl extraction experiments are presented as follows:

- The acceleration observed in MK-NaOH reaction kinetics provide strong indirect evidence for the presence of a nucleation step in geopolymers
- The nucleation sites in geopolymers appear to be silica species in solution. In low silica geopolymers (like the metakaolin-sodium hydroxide binders), adding small quantities of silica in activator solution will accelerate metakaolin dissolution and geopolymer growth. However excess of silica in activator solution leads to a growth controlled reaction, where the availability of alumina plays a key role in controlling the kinetics of geopolymer growth
- The addition of a semi-crystalline zeolite X seed, which is expected to have a nanostructure similar to that of the metakaolin-sodium hydroxide geopolymer was observed to be most effective in reducing the slight induction period observed in

MK-NaOH binders. This effect indicated the presence of an autocatalytic step, which has previously been hypothesized in geopolymmerization

- HCl dissolution data provides additional evidence for  $\text{TiO}_2$ ,  $\text{SiO}_2$  and zeolite X acting as nucleation seeds. All the three additives result in increased dissolution at 4h, whereas only silica exhibits enhanced dissolution up to 24h. This observation shows that the nucleation stage dominates a short time period (between 4-24h) in the overall geopolymmer kinetics. Adding  $\text{SiO}_2$  led to increased metakaolin dissolution beyond 4 and 24h. This observation provides further evidence that that silica promotes both nucleation and participates in the growth of gel, which serves as an additional driver for dissolution

Based on these hypotheses, a simple mechanistic picture of the geopolymmerization process is summarized in Figure 4.7.

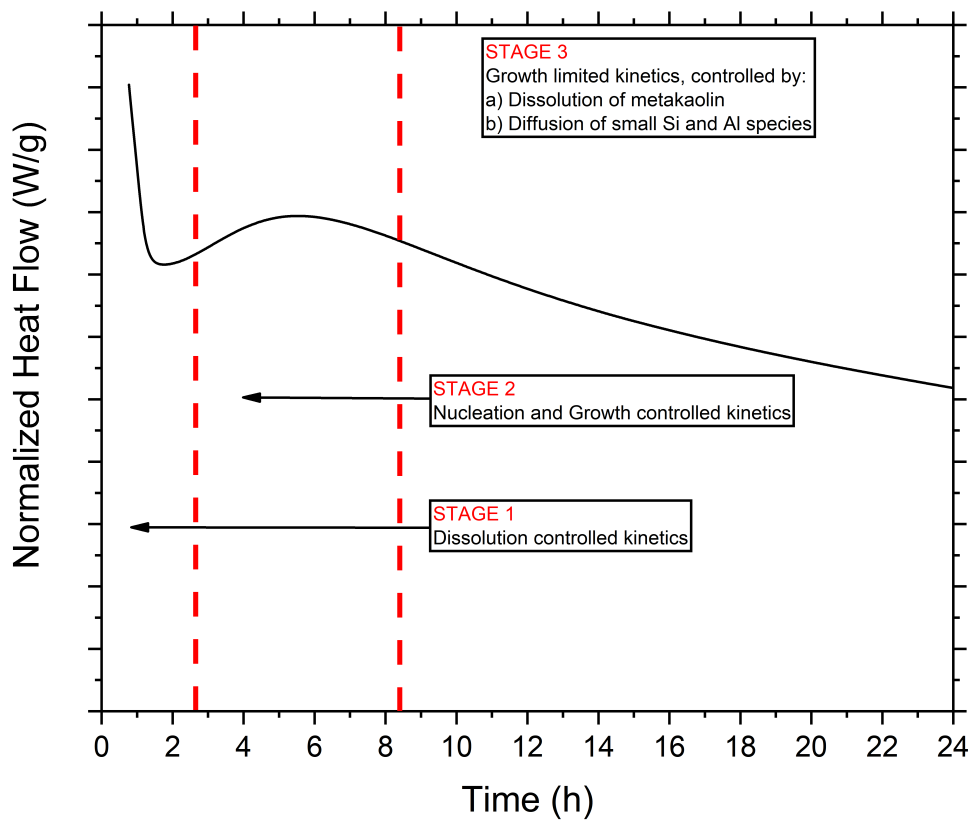


Figure 4.7: Mechanistic description of metakaolin-sodium hydroxide geopolymerization. The stage boundaries demarcated with the red dashed lines are approximate and intended as an aid to provide a visual picture of early age MK-NaOH kinetics

# Chapter 5

## Proof of external nucleation seeding

### 5.1 Introduction

In this chapter, the synthesis of an aluminosilicate precursor for geopolymerization is reported. Geopolymers have been prepared from this synthesized aluminosilicate precursor[90] (henceforth referred to as AlSi) and therefore, they offer another binder system to study geopolymerization. The precursor was used to prepare a geopolymer mix equivalent to the MK-NaOH binder, and the effects of seed addition were studied on this binder system. These precursors were also used in an attempt to prove the ability of zeolite X and  $\text{SiO}_2$  to act as nucleation seeds using the “micro-reactor” approach, established by Suraneni and Flatt [91, 92]. Further information relevant to the preparation of micro-reactors and some results are provided in Appendix A. The aluminosilicate synthesis procedure is reported here, along with results from SEM, XRD, FTIR, NMR and nitrogen adsorption.

The results and discussion in Chapter 4 present strong evidence of a nucleation controlled step being present in metakaolin-sodium hydroxide geopolymer formation. Subsequently, several hypotheses were presented by combining the observations derived from literature and effects of seeds on geopolymer reaction kinetics. In this chapter, zeolite X and  $\text{SiO}_2$  seeds were introduced in the AlSi-NaOH geopolymers to verify the proposed hypotheses in Chapter 4. Experimental isothermal calorimetry data and FTIR spectroscopy on AlSi-NaOH geopolymers, with and without seeds, were utilized to prove that zeolite X is indeed acting as a nucleation seed. The behavior of  $\text{SiO}_2$  in promoting nucleation and its ability to shift the reaction to growth controlled kinetics, when present in excess was proven in this chapter.

## 5.2 Synthesis of aluminosilicate precursor

The procedure used for the preparation of the aluminosilicate was based on the method described by Walkley et al., [93]. The synthesis procedure involves an organic polymeric steric entrapment solution-polymerization route to generate a homogeneous single phase, followed by calcination at moderate temperatures to remove the organic component. The targeted Si/Al ratio of the aluminosilicate was 1.0.

For the synthesis, 5% wt. polyvinyl alcohol (PVA) aqueous solution was prepared from 98–99% hydrolysed PVA (Alfa Aesar, molecular weight between 11,000-31,000) and added to a 40% (by wt.) aqueous solution of aluminium nitrate nonahydrate,  $\text{Al}(\text{NO}_3)_3 \cdot 9\text{H}_2\text{O}$  (Alfa Aesar, 98% purity).  $\text{Al}^{3+}/\text{OH}$  ratio of the solution was kept at 4, with OH being the number of hydroxyl groups in polvinyl alcohol. The resulting solution was subsequently stirred at 60°C for 2h before addition of 40% wt. aqueous colloidal silica solution (Sigma Aldrich, Ludox HS-40). The silica was added to ensure that Si/Al ratio in the solution is equal to 1.0. A typical batch of the PVA-aluminosilicate solution had 2.4g PVA, 80g of  $\text{Al}(\text{NO}_3)_3 \cdot 9\text{H}_2\text{O}$  and 166g of water. 32g of HS-40 colloidal silica was added after stirring for 2h at 60°C. Water in the the resulting aluminosilicate solution was evaporated slowly at 70-80°C with constant stirring, till a viscous gel was formed. The gel was calcined at 550°C for 1h, while the furnace temperature was increased at 3°C/min to oxidize all organic materials from the aluminosilicate. The resulting solid was crushed and sieved through a 125 $\mu\text{m}$  mesh. The sieved powder was characterized and used in geopolymers preparation. The batch proportions mentioned yielded  $\approx$ 35g powder. For the micro-reactors, particles in the 125-250 $\mu\text{m}$  size range were used.

### 5.3 Experimental methods

A Siemens D5000 diffractometer was used in the Bragg-Brentano configuration to collect powder XRD patterns. The electron gun voltage was maintained at 40kV and emission current set at 30mA. A single crystal silicon holder was used as it does not contribute to the background in the XRD patterns. XRF was carried out on a Shimadzu EDX-7000 instrument using a Rhodium X-ray source. The measurements were made in a helium atmosphere, and a fundamental parameter method was used to generate quantitative values for the elemental composition of the synthesized aluminosilicate. JEOL6060 SEM was used in the secondary electron mode, to characterize the morphology the aluminosilicate particles. Infrared spectra of the aluminosilicates were collected on a Perkin Elmer Frontier Spectrometer. An Attenuated Total Reflectance (ATR) attachment with a diamond crystal was used for the measurements. An average of 8 scans were taken for each spectra, with a resolution of  $4\text{cm}^{-1}$ . Nitrogen adsorption was carried out on a Micromeritics ASAP2020 instrument to measure the BET surface area of the aluminosilicate. The samples were pre-degassed at  $150^\circ\text{C}$  for 24h and at  $300^\circ\text{C}$  for 3h, both under a vacuum pressure of 30mm Hg.  $^{29}\text{Si}$  NMR spectra was collected using a Varian Inova Spectrometer operating at 7.04T. A  $90^\circ$  pulse, with a width of  $4\mu\text{s}$  was used. Recycle delay was kept at 30s and 2048 scans were measured for each spectrum. 1024 scans were collected for  $^{27}\text{Al}$  NMR spectra with a recycle delay of 1s and pulse width of  $2\mu\text{s}$ . Peak deconvolution was carried out using MNova v11.0.1 (Mestrelab Research S.L.).

The AlSi-NaOH geopolymers were characterized through isothermal calorimetry (at  $22^\circ\text{C}$ ) for early age reaction kinetics. FTIR spectra were collected at 1d and 7d age to understand the nature of products forming. The IR spectra of AlSi geopolymers were compared with those of MK-NaOH geopolymers to compare the products obtained from the two precursors. The AlSi-NaOH geopolymer reaction was stopped by crushing the sample with an agate mortar-pestle in acetone-methanol (1:1 by volume) [86]. The suspension was filtered through a Grade 1 Whatman Filter paper supported on a Buchner funnel, and the

residue was dried in a vacuum pressure of 18-20in Hg. Subsequently, the dried residue was used for FTIR measurements.

## 5.4 Characterization of synthesized aluminosilicate

### 5.4.1 Chemical characterization

The IR spectrum of the synthesized aluminosilicate is shown in Figure 5.1a, along with the IR spectrum of metakaolin for the purposes of comparison. Powder XRD pattern (Figure 5.1b) of the aluminosilicate shows no crystalline peaks, and therefore, the synthesized aluminosilicate is X-ray amorphous (like metakaolin). XRF data (Table 5.1) shows bulk Si/Al molar ratio equal to 1.0. FTIR and XRD suggests that the aluminosilicate has a chemical structure similar to that of metakaolin.

Table 5.1: Elemental composition (% wt.) of synthesized aluminosilicate

$\text{SiO}_2$	$\text{Al}_2\text{O}_3$	$\text{SO}_3$
53.5	46.3	0.1

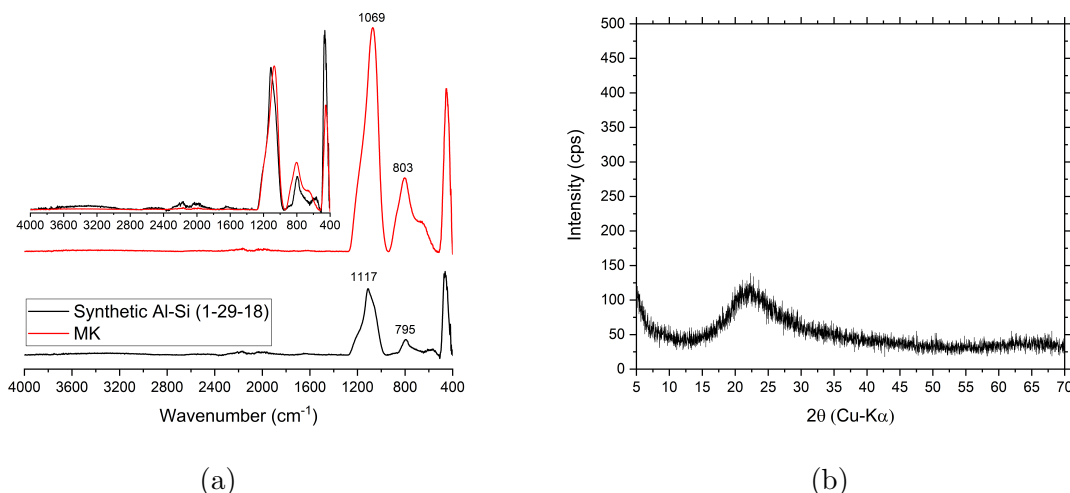


Figure 5.1: (a) IR spectra of synthesized aluminosilicate and metakaolin (normalized spectra inset) and (b) Powder XRD pattern of synthesized aluminosilicate

$^{29}\text{Si}$  and  $^{27}\text{Al}$  NMR spectra of the synthesized aluminosilicate are shown in Figure 5.2. The  $^{29}\text{Si}$  spectrum was deconvoluted from -90 to -130 ppm and two peaks were obtained, centered at -110 and -103 ppm. These frequency shifts correspond well to  $\text{Q}^4$  and  $\text{Q}^3$  silicon sites [82]. A small hump between -75 to -90 ppm indicates the presence of low Q species but the quantity of these sites are clearly much lower compared to  $\text{Q}^4$  and  $\text{Q}^3$  sites. The  $^{27}\text{Al}$  spectrum had peaks at 65 ppm, 35 ppm, and 6 ppm which correspond to Al(IV), Al(V) and Al(VI) sites respectively [82]. The NMR results correlate well with the NMR results on the aluminosilicate synthesized by Walkley et al., [93]. Unlike metakaolin, which is primarily composed of  $\text{Q}^4(1\text{Al})$  centers [47], the synthesized aluminosilicate possesses  $\text{Q}^4(0\text{Al})$  Si sites and tetrahedral alumina. Therefore, the structure of the synthesized aluminosilicate has been described to consist of a highly polymerized silicon rich phase, and another aluminum rich phase like mullite [93].

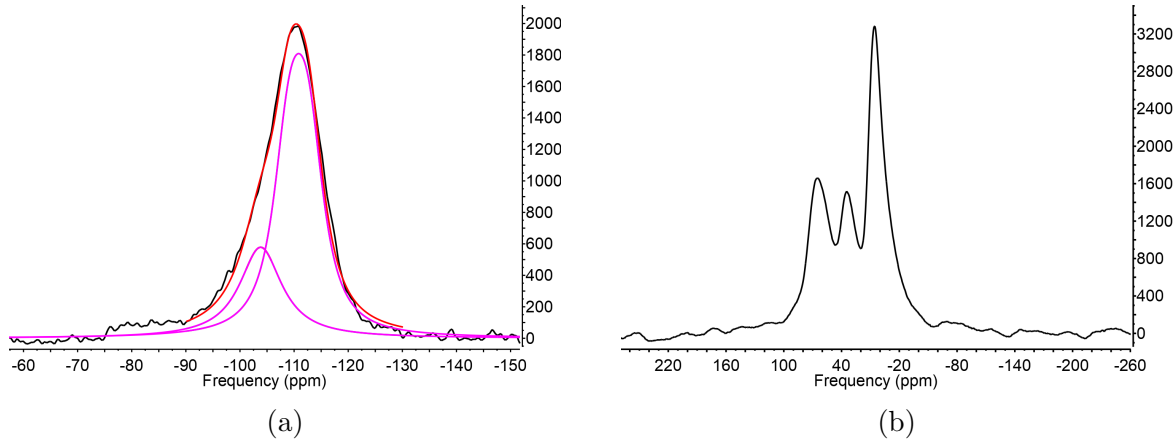


Figure 5.2: (a)  $^{29}\text{Si}$  NMR spectra of synthesized aluminosilicate and (b)  $^{27}\text{Al}$  NMR spectra of synthesized aluminosilicate

There is no information to as to how are the silicon and aluminum rich phase distributed spatially in the synthesized aluminosilicate. Therefore, SEM-EDS was used to generate qualitative Si and Al maps to check for the sample's homogeneity. For this purpose, a 200  $\mu\text{m}$  particle was embedded in epoxy and polished using SiC paper (2500X and 4000X). The maps for the sample are shown in Figure 5.3. The EDS maps clearly revealed a distinct Si rich region around 50  $\mu\text{m}$  in size. Therefore, it should be kept in mind that the micro-reactors

milled in the sample will have a high probability of being in either the Si rich or Al rich regions. It is unlikely that there will significant changes in the Si or Al concentrations within a micro-reactor with a cross section of  $5\mu\text{m} \times 1\mu\text{m}$ . Based on these results, it should be noted that the synthesized aluminosilicate is definitely not “metakaolin-like”.

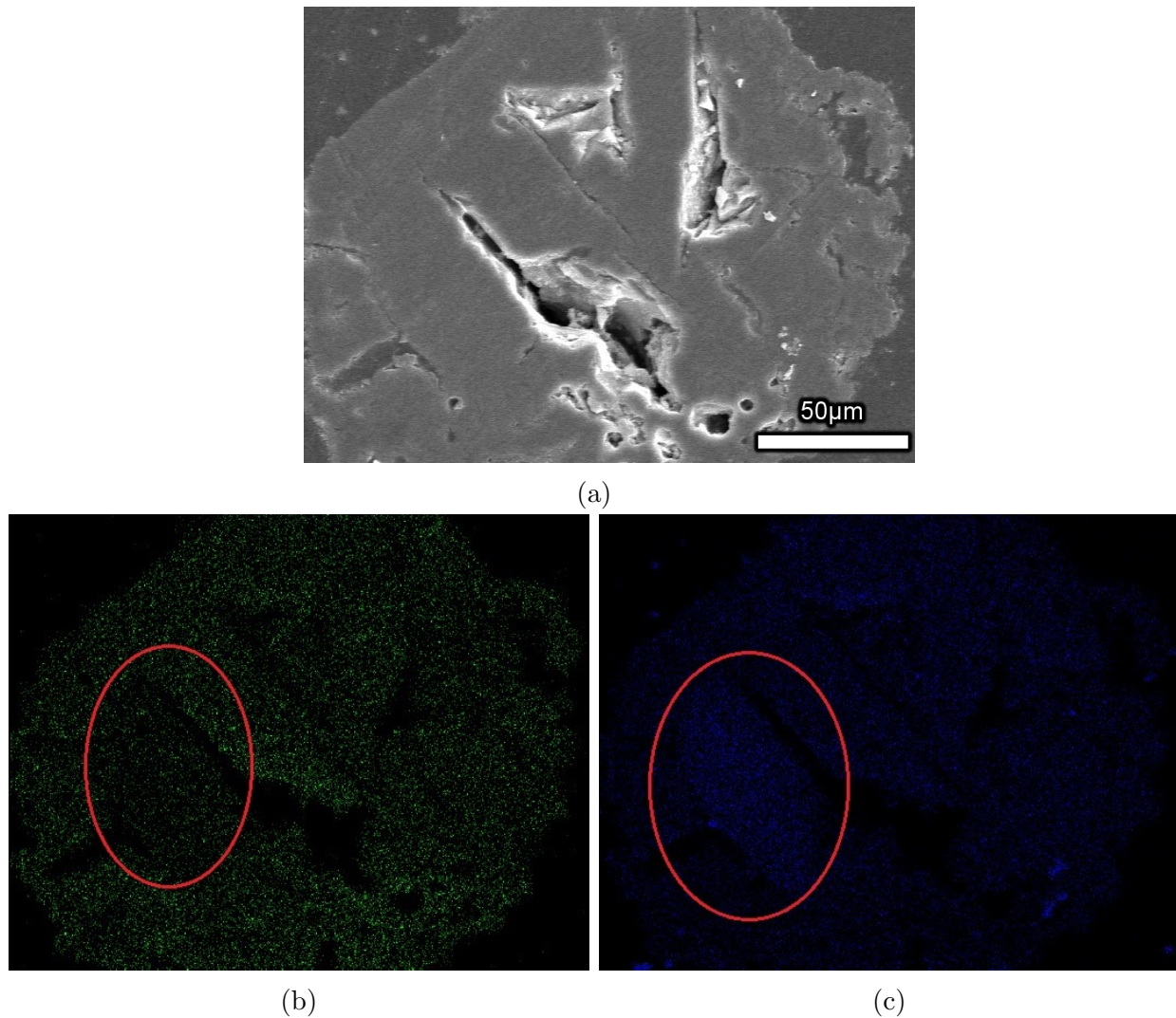


Figure 5.3: (a) SEM micrograph, (b) Al, and (c) Si EDS maps of synthesized aluminosilicate particle, with Si rich region encircled in red

#### 5.4.2 Surface area and morphology

Nitrogen adsorption and desorption isotherms are shown in Figure 5.4. The specific surface area was observed to be  $157\text{m}^2/\text{g}$ . The isotherms and surface areas measured

are noted to be very close to the aluminosilicate synthesized by Walkley et al [93]. SEM micrograph (Figure 5.5) shows that the aluminosilicate particles possess an angular morphology, which is typical of crushed powders.

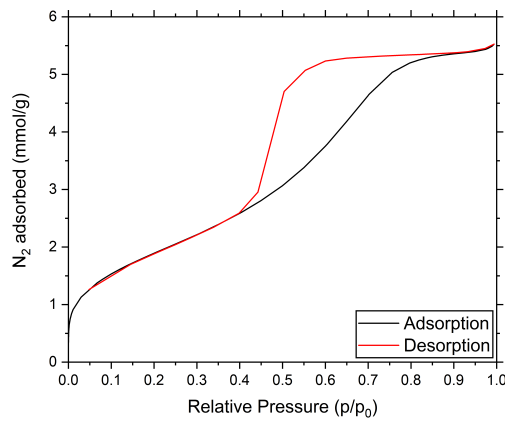


Figure 5.4: Nitrogen adsorption and desorption of synthesized aluminosilicate

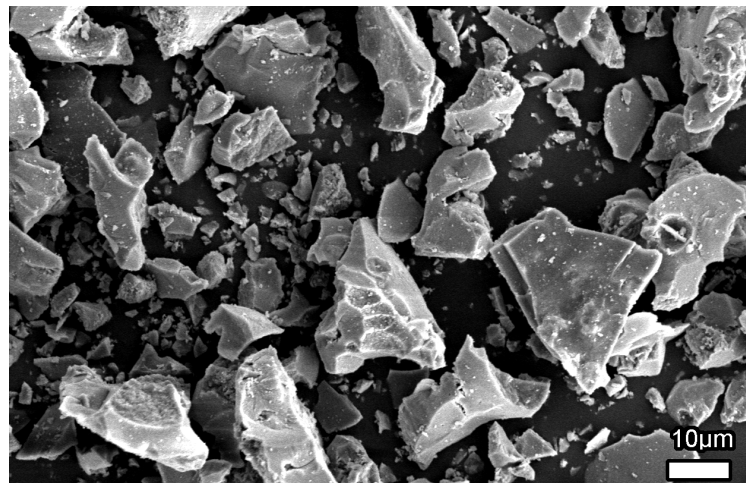


Figure 5.5: SEM micrograph of the crushed aluminosilicate particles

## 5.5 AlSi-NaOH geopolymers: Results and Discussion

### 5.5.1 Comparison to MK-NaOH geopolymers

Isothermal calorimetry and FTIR spectra were used to understand the differences between geopolymers derived from synthetic aluminosilicate ( $\text{Si}/\text{Al}=1.00$ ) and metakaolin ( $\text{Si}/\text{Al}=0.98$ ). The metakaolin and the synthetic aluminosilicate were clearly different in terms of local molecular structure and surface areas. The synthetic aluminosilicate had surface areas an order of magnitude greater than metakaolin, while NMR and SEM-EDS revealed the presence of silicon rich regions in the microstructure.

Adding NaOH solution to the synthesized aluminosilicate, there was a rapid increase (within first 30s) in the temperature of the mixing cup with slight stirring, analogous to what is observed when NaOH pellets are dissolved in water for concentrated NaOH solutions. This observation, combined with the fact that the AlSi precursor has high surface area makes it clear that rapid dissolution of the precursor is taking place. The isothermal calorimetry data for AlSi geopolymers in Figure 5.6 also exhibits higher heat evolution compared to metakaolin geopolymers before 9h, confirming rapid rate of reaction.

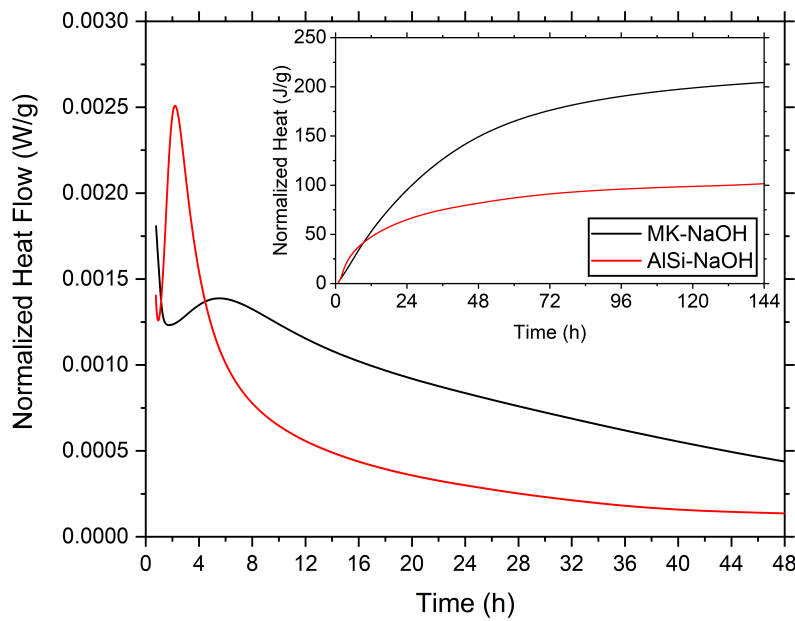


Figure 5.6: Isothermal calorimetry data for AlSi-NaOH and MK-NaOH geopolymers

FTIR spectra at 1d in Figure 5.7a for the AlSi-NaOH and MK-NaOH geopolymers show significant differences, with two asymmetric Si-O-T ( $T=Si/Al$ ) stretching peaks being observed in the AlSi geopolymers. Figure 5.7b makes it clear that the shoulder at  $1100\text{cm}^{-1}$  for AlSi-NaOH-1d spectrum is coming from unreacted aluminosilicate precursor. Therefore, the presence of two asymmetric stretching peaks (at  $1018\text{cm}^{-1}$  and  $968\text{cm}^{-1}$ ) means that there are two silicon environments in the geopolymer product derived from the AlSi precursor. This observation, the fact that the AlSi precursor dissolves rapidly, and the presence of a Si-rich phase in the precursor implies that there is an incongruent dissolution of the synthesized aluminosilicate. It is likely that silicon is being preferentially dissolved out over aluminum, leading to the formation of a phase separated, silicon rich, aluminosilicate gel (indicated by the peak at  $1018\text{cm}^{-1}$ ) within the geopolymer at early age (<1d).

Figure 5.7b shows that the peak at  $968\text{cm}^{-1}$  coincides closely with the peak for geopolymer product obtained from metakaolin, which means that the second silicon environment (with more aluminum substitution, at  $968\text{cm}^{-1}$ ) belongs to the product

observed in metakaolin geopolymers. FTIR spectra for the MK-NaOH geopolymers from 4h to 70d shows a single peak, and the peak position is always within the range of  $968\text{-}975\text{cm}^{-1}$ , which means this environment is the thermodynamically preferred product for the mix stoichiometry. Therefore, the Si-rich geopolymer gel is probably a metastable phase which transforms into the geopolymer product typically observed in MK-NaOH geopolymers. Indeed, Figure 5.7c shows that with increasing age, the peak intensity ratios at  $1018\text{cm}^{-1}$  to  $968\text{cm}^{-1}$  decrease. As a side note, unlike in some of the other spectra presented in this thesis, none of the IR spectra in Figure 5.7 have been normalized. Normalization cannot be carried out because the presence of two asymmetric stretching peaks leads to ambiguity in deciding the abscissa to be used for normalizing any two spectra. The analysis reported here only utilizes the relative differences in the ratio between peak intensities at  $1018\text{cm}^{-1}$  and  $968\text{cm}^{-1}$  for two spectra; otherwise, peak intensities are not used in any interpretation.

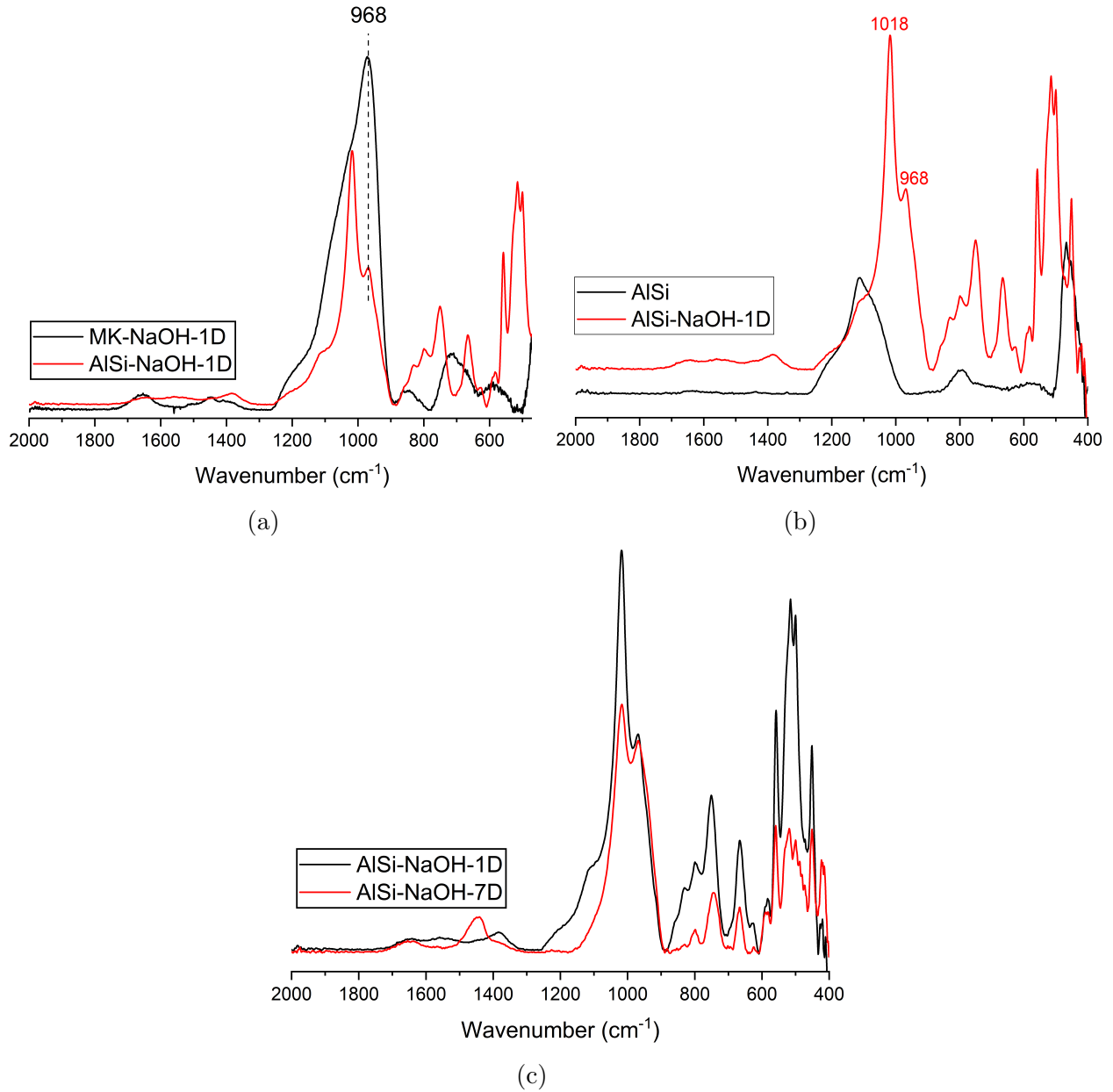


Figure 5.7: FTIR spectra comparing (a) MK and AlSi geopolymers at 1d, (b) AlSi precursor and geopolymer derived from the precursor at 1d, and (c) AlSi geopolymers at 1d and 7d

### 5.5.2 Seeding in AlSi-NaOH geopolymers

Adding 5% SiO<sub>2</sub> and zeolite X displayed pronounced retardation on the kinetics of AlSi-NaOH geopolymerization, as shown in Figure 5.8. Considering addition of SiO<sub>2</sub>, it

was discussed that the role of silica was to provide nucleation sites and promote growth in the geopolymers product. However, the incongruent, rapid dissolution of Si from the AlSi precursor implies that there will be excess Si over Al in the pore solution. This lack of Al in solution implies that gel polymerization and growth will slow down (limited by availability of Al species in solution), as discussed in Sec. 4.3.2. Therefore, the reduction in the rate of reaction due to addition of external  $\text{SiO}_2$  in activator solution is not surprising, and is explained by our previous hypotheses. However, the behavior of zeolite X is difficult to understand from calorimetry data alone, and is described with FTIR spectra in the following paragraph.

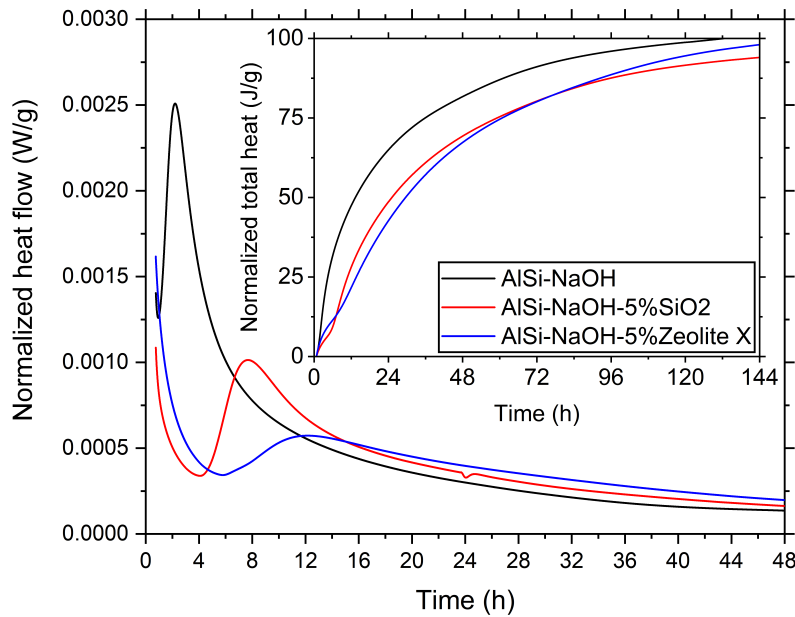


Figure 5.8: Isothermal calorimetry data for AlSi-NaOH mix and mixes seeded with 5%  $\text{SiO}_2$  and zeolite X

Before proceeding further, the hypothesis tested in this paragraph is the fact that zeolite X only nucleates the growth of the geopolymers product observed in MK-NaOH geopolymers. Zeolite X seed addition was observed to decelerate the AlSi geopolymers strongly in the first 48h. FTIR spectra in Figure 5.9 shows that

peak intensity ratios at  $1018\text{cm}^{-1}$  and  $968\text{cm}^{-1}$  to be decreasing in the following order: AlSi-NaOH-1d>AlSi-NaOH-5% zeolite X-1d>AlSi-NaOH-7d. This observation implies that more of the metakaolin geopolymers-like product is forming in the zeolite X seeded binder compared to the unseeded mix at 1d, confirming our hypothesis that the zeolite X seed indeed nucleates the growth of geopolymers product. No clear proof can be obtained as to why such slow kinetics are observed upon seeding with zeolite X. The following hypothesis is offered as an explanation.

It is clear from Figures 5.6 and 5.7a that the AlSi-NaOH geopolymers react rapidly to form a silica rich geopolymers product along with lesser amounts of the typical geopolymers observed from MK-NaOH binders, in the first 24h. The presence of zeolite X probably imposes a constraint on the reaction to form the MK-NaOH type geopolymers product, which is not kinetically favorable for the AlSi-NaOH geopolymers. Therefore, the reaction drastically slows down since more aluminum has to be dissolved out of the AlSi geopolymers to form the MK-NaOH-like geopolymers product.

On a separate note, the AlSi precursor system is not well explored and several fundamental studies such as leaching (or dissolution) to quantify release rates of Si and Al, along with NMR and long term calorimetry needs to be carried out. Such experiments were not carried out since it goes beyond the scope of this study. It is clear that this binder system offers promise in yielding more experimental information about geopolymers in general.

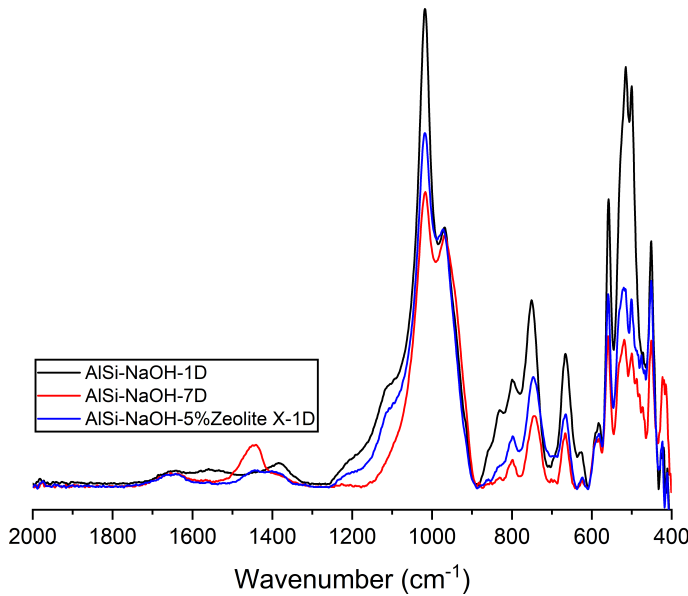


Figure 5.9: FTIR spectra of AlSi geopolymers at 1d and 7d, along with spectrum of AlSi-5%Zeolite X seeded geopolymer at 1d. Based on peak intensity ratios at  $1018\text{cm}^{-1}$  and  $968\text{cm}^{-1}$ , it is clear that more of the MK-NaOH geopolymeric product (w.r.t Si-rich geopolymer) is formed at 1d upon zeolite X addition, in comparison to AlSi-NaOH-1d

## 5.6 Conclusions

The following conclusions were obtained from this chapter.

- An amorphous aluminosilicate with an Si/Al ratio of 1.0 was successfully synthesized. Despite possessing the same Si/Al ratio as metakaolin, the precursor was observed to be different from metakaolin, as observed through microchemical analysis and NMR spectroscopy. The synthesized aluminosilicate possessed two phases, one relatively richer in silica than the other. Surface area of synthesized aluminosilicate was one order of magnitude higher than that of metakaolin.
- Reaction with NaOH led to extremely high heat generation, indicative of rapid dissolution. Geopolymer product formed was observed to be composed of two phases,

one richer in silica relative to the other. FTIR indicated that the low silica geopolymers product was similar to the product obtained from MK-NaOH geopolymers. The formation of two products was believed to be due to incongruent dissolution of precursor, with Si being preferentially dissolved over Al. FTIR revealed that the Si rich phase was formed at early age ( $\leq 1$ d). The intensity of its corresponding Si–O–T asymmetric stretching peak decreased over time, relative to the asymmetric stretching peak of the MK-NaOH-type geopolymers product.

- The role of  $\text{SiO}_2$  as a nucleation seed and presence of dissolved alumina as a limiting factor for growth was proved by applying the hypothesis derived from the previous chapter to geopolymers prepared from a synthesized aluminosilicate precursor. Excess Si is clearly present in the pore solution of AlSi-NaOH geopolymers at the time of mixing, due to rapid, incongruent dissolution which consequently leads to a growth-controlled geopolymer reaction. The addition of  $\text{SiO}_2$  through the activator solution therefore reduces the rate of reaction, since the growth controlled geopolymerization is limited by the availability of dissolved alumina.
- The seeding effect of zeolite X was also proved using FTIR spectroscopy, which revealed the ability of zeolite X seed to promote the formation of MK-NaOH-type geopolymers product over the silica-rich geopolymers product observed in the AlSi-NaOH geopolymers binder. However, the formation of the MK-NaOH-type product is not kinetically favorable at early age ( $\leq 1$ d), and therefore, the addition of zeolite X strongly retarded AlSi-NaOH geopolymerization.

# Chapter 6

## Consequences of external seeding

### 6.1 Introduction

In this chapter, the effects of nucleation seeding was characterized by using the Avrami equation to model nucleation kinetics. Isothermal calorimetry data presented in Chapter 4 was used as experimental data for Avrami modeling. The Avrami model has been applied previously in studies involving the characterizing the hydration of cement or tricalcium silicate ( $C_3S$ ) [64, 94–96] through isothermal calorimetry. However, the use of Avrami equation to model cement hydration has a fair share of concerns, as highlighted by multiple studies [64, 97]. The Avrami model assumes that nucleation is spatially random, whereas for cement hydration, it has been well established that nuclei form preferentially on cement (or  $C_3S$ ) particle surfaces [98]. Cement hydration process is a complex process, with the kinetics being controlled by multiple rate-controlling steps at different temporal steps. If the rate of diffusion of reactants to the reaction site becomes rate controlling (which is known to happen in the later stages of cement hydration [98]), the Avrami model is no longer valid [64]. The Avrami fit parameters are also observed to be different from theoretical values [64]. Fit parameters obtained in this study are compared between control vs. seeded mixes only, and no emphasis is placed on the “absoluteness” of the value obtained.

Literature has shown that some consequences of seeding in geopolymer binders include strength improvement [13], microstructural refinement [13], and spatial changes in Si and Al elemental distribution of geopolymer gel [13, 59]. Therefore, the effects of adding 5% zeolite X and 5%  $SiO_2$  on porosity, strength and crystalline phase composition were also investigated on the MK-NaOH geopolymers.  $SiO_2$  and zeolite X seeds were chosen since

they had the greatest effect on reaction kinetics, when compared to zeolite A and TiO<sub>2</sub>.

To determine if seeds can affect the chemical nature of products forming from MK-NaOH binders, XRD patterns were collected on the seeded and control binders. While the chemical structure of the amorphous geopolymers gel is hard to characterize, crystalline zeolites forming from MK-NaOH upon aging can be characterized easily through XRD. Therefore, XRD patterns were collected at 28d, 56d and 70d (since MK-NaOH control was observed to form zeolite X and zeolite A at around 28d under sealed conditions at 22°C). Changes in XRD patterns would indicate that the seeding generates new kinetically or thermodynamically accessible products.

Microstructural refinement can be characterized through porosity measurements of seeded and un-seeded MK-NaOH binders at early age ( $\leq 7$ d). Typical methods for measuring porosity on cement based binder materials have been described in detail elsewhere [99, 100]. Some of the simplest porosity measurements include saturating oven dried specimens with non-reacting organic solvents like methanol and isopropanol [99]. However, oven-drying can damage the microstructure of binder materials and remove chemically bound water as well [101]. Therefore, less severe methods of drying such as solvent exchange and freeze drying are typically used to preserve the microstructure. Helium pycnometry has also been used to measure the porosity of cement binders [102]. Apart from these methods, mercury intrusion porosimetry (MIP) [99, 102] and backscattered scanning electron microscopy [100] have also been employed to quantify porosity in such materials. The advantage of these two methods is that it offers an estimate of pore-size distribution, however, the pore-size distribution from MIP is known to be inaccurate due to the bottleneck effect [103].

In this study, approximate measurements of porosity were obtained through SEM-BSE at 1d and 7d age. Attempts to supplement the SEM-BSE porosity values with helium pycnometry led to questionable results and a description of these attempts are presented in the Appendix C. Compressive strength results at 1d, 7d, 28d, 56d and 70d are also presented to investigate any practical benefits of external nucleation seeding on the

MK-NaOH binder.

## 6.2 Materials and methods

The metakaolin-sodium hydroxide geopolymers were prepared in the same manner as described previously in Sec. 4.2.1. Seed synthesis and its dispersion in NaOH solution was described in Chapter 3. AlSi-NaOH geopolymers were prepared with the same stoichiometry as those of MK-NaOH geopolymers. 20g AlSi was mixed with 7.15g of NaOH pellets and 20.26g water to form the paste used in isothermal calorimetry. As before, the NaOH solution was prepared beforehand and the mixing was carried out with the powder and activator solution at room temperature. The same motorized shear mixer (DrinkMaster, Hamilton Beach) was used to mix the AlSi-NaOH pastes for 4mins.

### 6.2.1 Avrami modeling

The Avrami model was applied to isothermal rate of heat evolution data from the control MK-NaOH mix, and other mixes seeded with 1%TiO<sub>2</sub>, 5% SiO<sub>2</sub> and 5% zeolite X. A four parameter Avrami equation (Eq. 6.1) described in literature [64, 95] was used. Curve fitting was carried out in OriginPro, using the Levenberg-Marquardt iteration algorithm. Tolerance was set by limiting the chi-squared value to less than  $1 \times 10^{-9}$ .

$$R = Ank_{avr}^n(t - t_o)^{n-1} \exp(-[k_{avr}(t - t_o)]^n) \quad (6.1)$$

where, R is the rate of reaction (or rate of heat evolution from calorimetry); A is a normalization constant, t<sub>o</sub> is the delay between the time of mixing and onset of nucleation and growth kinetics, and k<sub>avr</sub> is the effective rate constant, combining rate constants for nucleation, growth and diffusion processes (which are assumed to remain constant) during the kinetic process [64, 94].

Based on the description of geopolymmerization processes in Chapters 2 and 4, it is clear that the metakaolin dissolution process beginning from time  $t=0$  lead to presence of silica and alumina monomers in solution. The formation of small cyclic aluminosilicate species (which were described to be nuclei for geopolymmer growth in Chapter 2 and 4) is a very rapid process occurring in the scale of milliseconds, as described by North and Swaddle [56]. Therefore,  $t_0$  in Eq. 6.1 was set to zero during curve fitting. In a previous study,  $t_0$  was set to zero for modelling hydration kinetics of rapidly dissolving  $\text{C}_3\text{S}$  with surface area of  $0.7\text{m}^2/\text{g}$  [94]. For comparison, metakaolin used in this study had a surface area of  $14\text{m}^2/\text{g}$ .

The discussion in Sec. 4.3.2-4.3.4 illustrates that similar to cement hydration, geopolymmer reaction kinetics are controlled by different rate controlling mechanisms at different time intervals. Adding seeds was observed to affect the second rate peak, which indicated that it is related to nucleation and growth processes. Therefore, a section of the rate peak was used to fit Eq. 6.1. The lower and upper time bounds for the section were chosen arbitrarily, based on whether an Avrami fit was obtained with the data. For example, the data-set used for fitting Avrami model on MK-NaOH is shown in Figure 6.1. It should be noted that a similar procedure has been adopted for while modeling cement hydration kinetics through Avrami equations [64, 94].

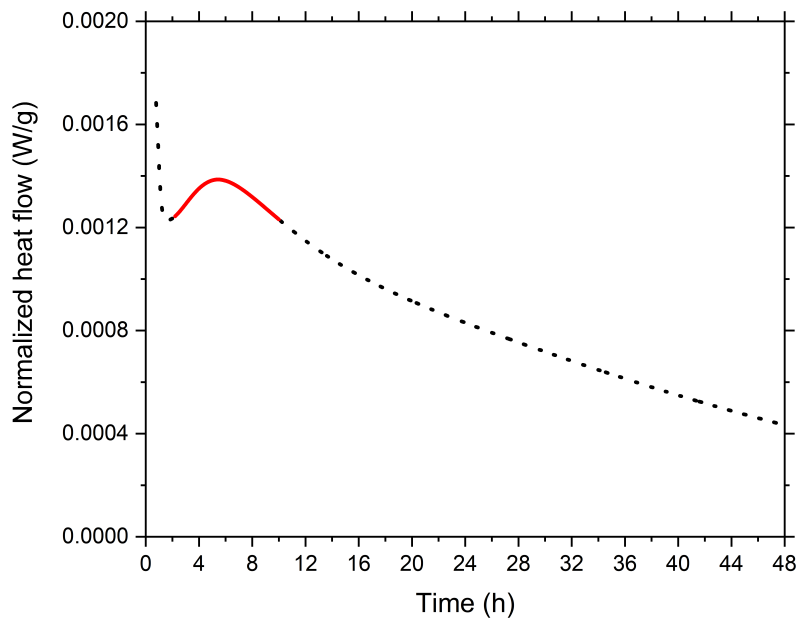


Figure 6.1: Section of rate of heat evolution data for MK-NaOH used for fitting the Avrami equation (red) within the entire calorimetry dataset (black, dotted)

### 6.2.2 SEM-BSE porosity measurements

SEM-BSE measurements to quantify porosity of cement based binders involve an epoxy-impregnation procedure of the sample to preserve the microstructure during polishing, and also to ensure that contrast is generated between the calcium phases (cements) and pores [100]. The epoxy filled pores ensure that incident electron beam do not lead to backscattered electrons being ejected from the pores. This procedure of measuring porosity cannot be adopted for measuring porosity in metakaolin geopolymers, since there is little difference between the backscattering coefficient of epoxy (carbon) and sodium-aluminosilicates [70]. Therefore, there is barely any contrast between epoxy and aluminosilicates, as illustrated in Figure 6.2.

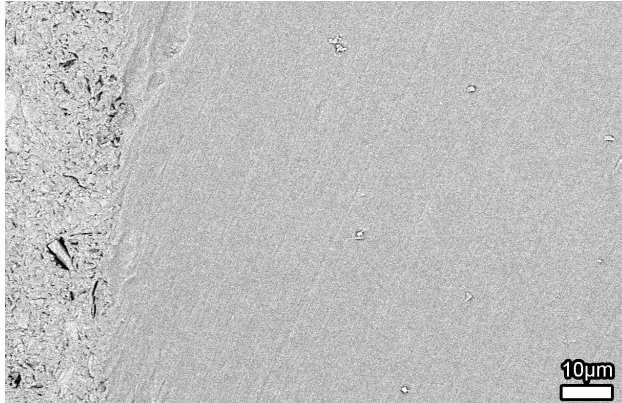


Figure 6.2: SEM-BSE micrograph of epoxy impregnated sample, with plain epoxy on the right side and a portion of the epoxy impregnated aluminosilicate seen on the left. No contrast difference is observed

To address this issue, the samples were partially epoxy impregnated to aid in polishing, and backscattered electron images were taken in the non-impregnated region. This resulted in the pores showing up in absolute black, which enabled the use of image analysis to estimate porosity. This method suffers from drawbacks, since there is no knowledge of whether the microstructure in the non-impregnated region is getting affected due to polishing. In addition, there is no solid to prevent backscattered electrons coming out of the pores. Errors due to such an effect were partially addressed by using a low accelerating voltage of 8kV, which leads to a low interaction depth and therefore limits BSE electron emissions from deep inside the sample. The parameters described can be factored into Eq. 6.2 for estimating interaction depth [70].

$$R = \frac{0.0276A}{Z^{0.89}\rho} E_{\circ}^{1.67} \quad (6.2)$$

where, R is the interaction depth ( $\mu\text{m}$ ), A is atomic weight (g/mol), Z is atomic number,  $\rho$  is density ( $\text{g}/\text{cm}^3$ ), assumed to be  $2\text{g}/\text{cc}$ , which is common for crystalline derivatives of MK-NaOH geopolymers, zeolites A and X [104]. This leads to an approximate interaction depth of  $1\mu\text{m}$ , which indicates that the black regions in BSE-SEM micrographs are atleast  $1\mu\text{m}$  deep.

Therefore, the porosity values from this procedure are not absolute and should be treated with caution. However, the effect of seeding was prominent enough to be distinguishable visually, and the porosity percentages presented will serve as an aid to compare the differences in porosity between the un-seeded and seeded samples. Pore size distribution data is not presented owing to the errors associated with this measurement.

For porosity measurements, geopolymers were poured in cylindrical molds of 0.5in diameter and 1in height. The samples were demolded after 1d, and were sealed off till testing. Geopolymerization was stopped by immersing the samples in  $\approx$ 50ml acetone-methanol solvent (1:1 by volume) in a vacuum dessicator, under 20in Hg vacuum pressure for 24h. Subsequently, the samples were transferred to 50ml of fresh acetone-methanol and submerged for another 24h. After the solvent exchange, the samples were dried in the same dessicator, and then used for preparing SEM samples. Control, 5% $\text{SiO}_2$  and 5% zeolite X seeded samples were analyzed at 1d and 7d age.

For porosity measurement, two different samples of the same composition were partially epoxy-impregnated using a low viscosity two-part epoxy (EPO-TEK 301, Epoxy Technology). A fresh section was exposed using a low speed diamond saw (Buehler Isomet), and ground using SiC paper with grit sizes 600, 800, 1000 and 1200. Subsequently, 15 SEM-BSE micrographs were taken at random locations for each sample, leading to a total of 30 images per mix, with each image covering an area of  $\approx$ 50 $\times$ 38 $\mu\text{m}$ .

Image analysis was carried out with ImageJ. The Otsu algorithm was used to determine the threshold between solid (light) and pores (dark). Subsequently, an erode and dilate process was applied to remove individual and small clusters of pixels within the solids that arise out of the thresholding process. The image analysis procedure is highlighted in Figure 6.3.

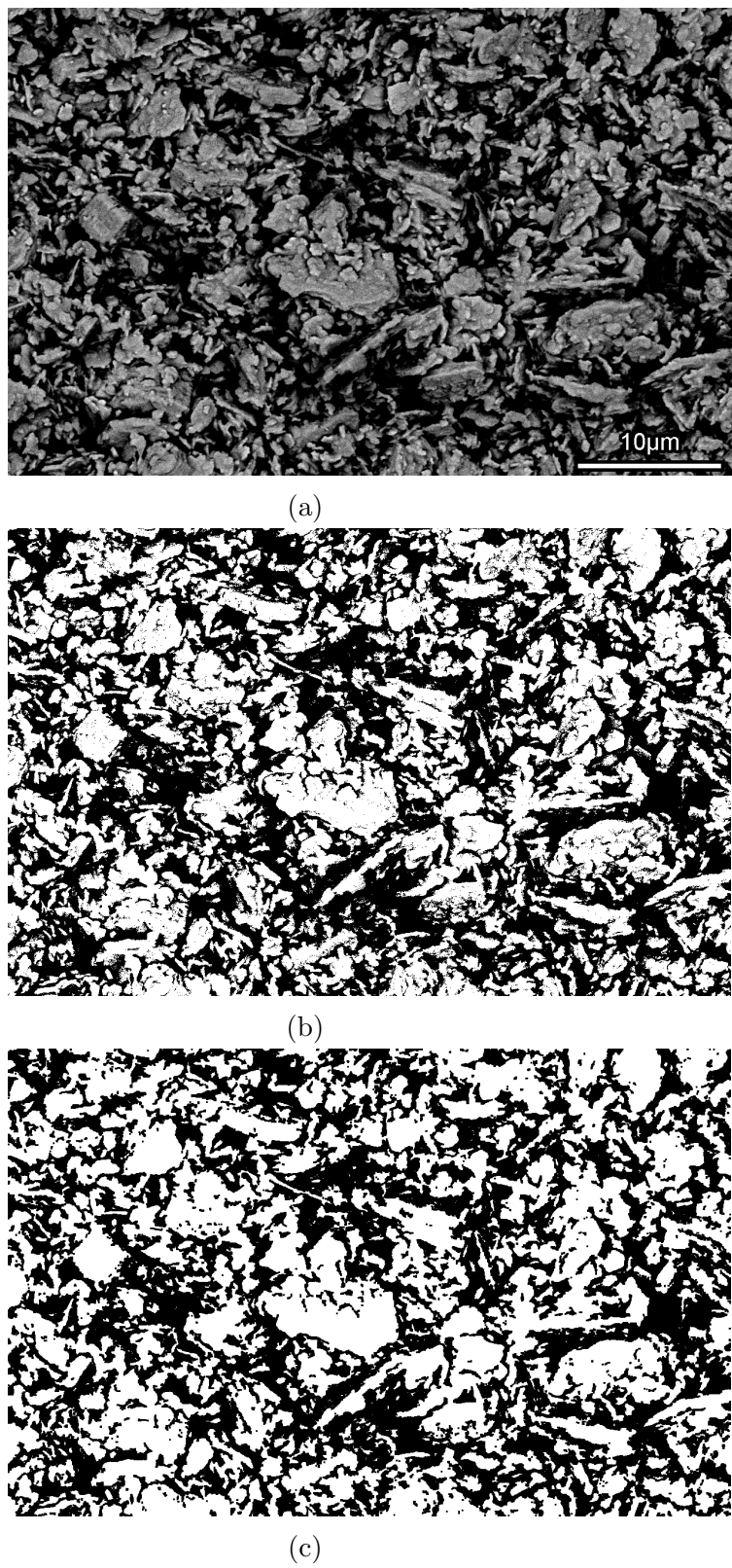


Figure 6.3: a) SEM-BSE micrograph of MK-NaOH-1d, (b) after applying threshold as per Otsu algorithm, (c) after applying erode and dilate process, following which porosity percentage (dark region) is calculated

### **6.2.3 X-Ray diffraction**

XRD patterns were collected on a Siemens-Bruker D5000 diffractometer using Cu-K $\alpha$  radiation, with the patterns being recorded from 5 to 70° 2 $\theta$  at a rate of 1° per min. XRD patterns were collected for control, 5%SiO<sub>2</sub> and 5% zeolite X seeded samples at 28d, 56d and 70d age. The solvent exchange method using acetone-methanol was used to stop the geopolимер reaction. ZnO was used as internal standard, and was mixed in a ratio of 1:3 (ZnO:Sample, by wt.). Both the sample and internal standard were sieved through a 125 $\mu$ m sieve, following which, the internal standard and sample were lightly ground for 5 minutes to ensure even dispersion of ZnO throughout the sample. A single crystal Si holder was used for carrying out the measurements to avoid background noise from the holder.

### **6.2.4 Compressive strength**

Compressive strength measurements were carried out using 1 inch cubes. The geopolимер paste was introduced in three layers, and each layer was compacted by placing the mold on top of a flow table and cycling it 50 times. The flow table is typically applied for measuring slump flow of cement pastes and mortars, and is described in ASTM C230 [105]. Strength tests were carried out on an Instron load frame equipped with a 10kN static load cell, at a constant displacement rate of 1mm/min. Mean compressive strength for 12 cubes were reported. All the samples were demolded 1d after casting, and were kept at 22°C, in a sealed condition before and after demolding.

## **6.3 Results and Discussion**

### **6.3.1 Avrami modeling**

The Avrami parameters obtained by fitting Eq. 6.1 to calorimetry data are presented in Table 6.1, and fitted curves are illustrated in Figure 6.4. Similar to what is observed in

Avrami curve-fits of cement hydration, the Avrami equation fits the second rate peak in MK-NaOH geopolymers. However, the Avrami equation fails to model the reaction after  $\approx$ 6-8h, which is indicating that the reaction goes into growth controlled kinetics, limited by dissolution of precursor and/or diffusion of Si and Al species. These two observations agree with the mechanistic description of geopolymers kinetics, thereby strengthening the proposed kinetic mechanism in Figure 4.7.

The reaction rate constant,  $k_{avr}$  shows the expected relative trends upon seeding, with the 5%  $\text{SiO}_2$  and zeolite X seeded mixes showing a higher rate constant relative to control. Since the constant  $K_{avr}$  is derived from a combination of multiple processes (nucleation, diffusion, etc.), it cannot be clearly judged as to whether the acceleration is solely due to nucleation. However, considering the case of zeolite X, which was considered to be inert in NaOH solutions, the reaction can only be accelerated if a seeding effect is considered. The rate constants between zeolite X and  $\text{SiO}_2$  are observed to be the same, despite the fact that the latter mix generates a much higher rate of heat evolution than zeolite X in the first 24h. Since growth kinetics are clearly accelerated upon  $\text{SiO}_2$  addition, the combined rate constant comparison indicates that zeolite X acts as a better nucleation seed, as hypothesized within the discussion in Sec. 4.3.4. Avrami fit parameters on  $\text{TiO}_2$  seeded mixes showed similar  $k_{avr}$  compared to control.

Table 6.1: Avrami parameters for fitting Eq. 6.1 to isothermal calorimetry data

Sample	A (J/g)	n	$k_{avr}$ ( $\text{hr}^{-1}$ )
MK-NaOH	0.0240	1.423	0.07828
MK-NaOH-1% $\text{TiO}_2$	0.0267	1.334	0.07719
MK-NaOH-5% $\text{SiO}_2$	0.0269	1.557	0.11673
MK-NaOH-5%ZeoliteX	0.0237	1.461	0.11656

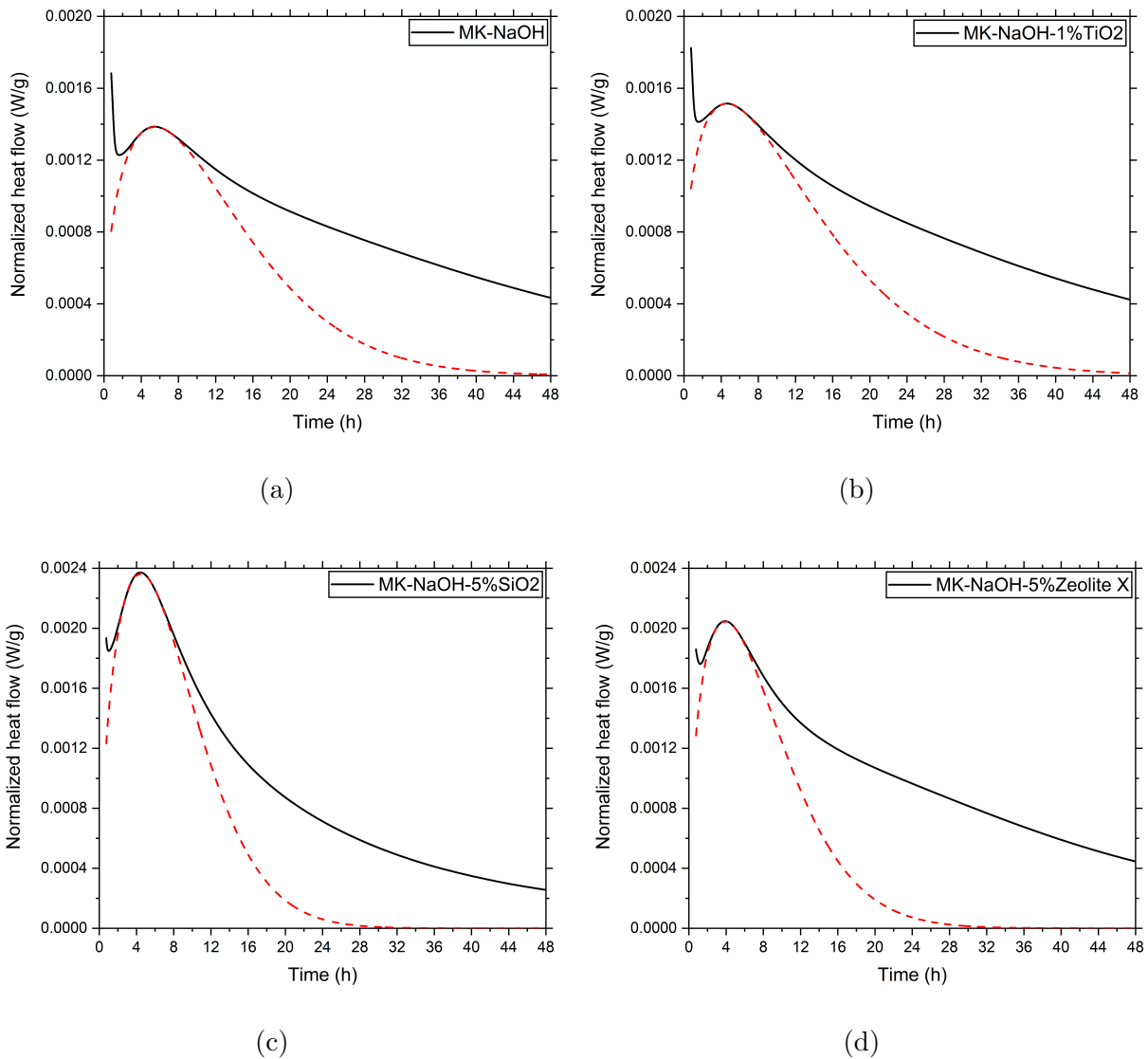


Figure 6.4: Avrami fits (red, dotted) for a) MK-NaOH, and MK-NaOH seeded with (b) 1%TiO<sub>2</sub>, (c) 5% SiO<sub>2</sub> and (d) 5% zeolite X. Experimental calorimetry data in black

### 6.3.2 SEM-BSE Porosity measurements

The porosity obtained from image analysis of the SEM-BSE micrographs is presented in Figure 6.5. The results clearly show that the addition of 5% SiO<sub>2</sub> and zeolite X decreases porosity, an effect which is consistent with external nucleation seeding in both cement and geopolymers binders [13, 14]. As described earlier, the porosity percentage values may not be

accurate, owing to procedural issues in generating contrast between voids and the sample. However, metakaolin geopolymers with Si/Al ratio of 1.4 have been observed to yield porosity (measured through mercury intrusion porosimetry) values in the order of 30-40% after 85°C curing for 2h [106]. Other low-silica metakaolin geopolymers have been observed to possess porosity around 40% [107], at 1d age. The data from literature therefore suggests that the values in Figure 6.5 are not wildly inaccurate. Irrespective of the porosity values in different samples, SEM micrographs in Figure 6.6 show clear proof of microstructure refinement taking place as a consequence of external seeding.

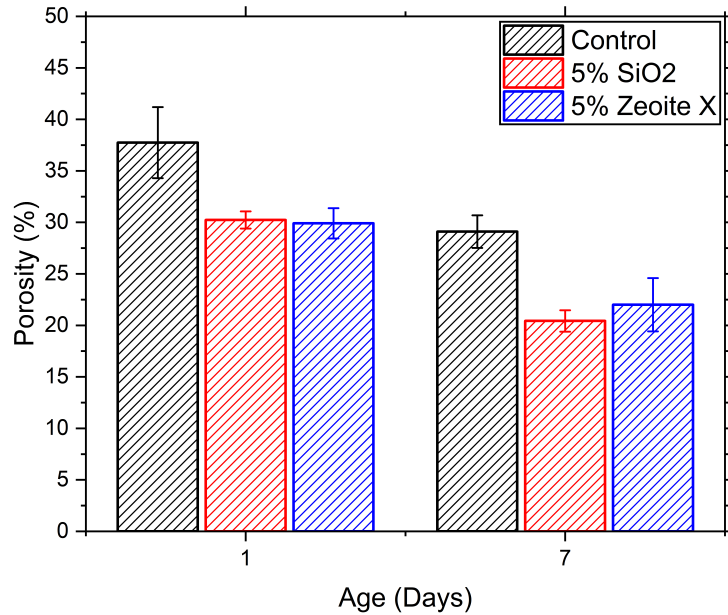


Figure 6.5: Porosity data from image analysis of seeded and unseeded MK-NaOH geopolymers. Standard deviation from mean is reported through error bars

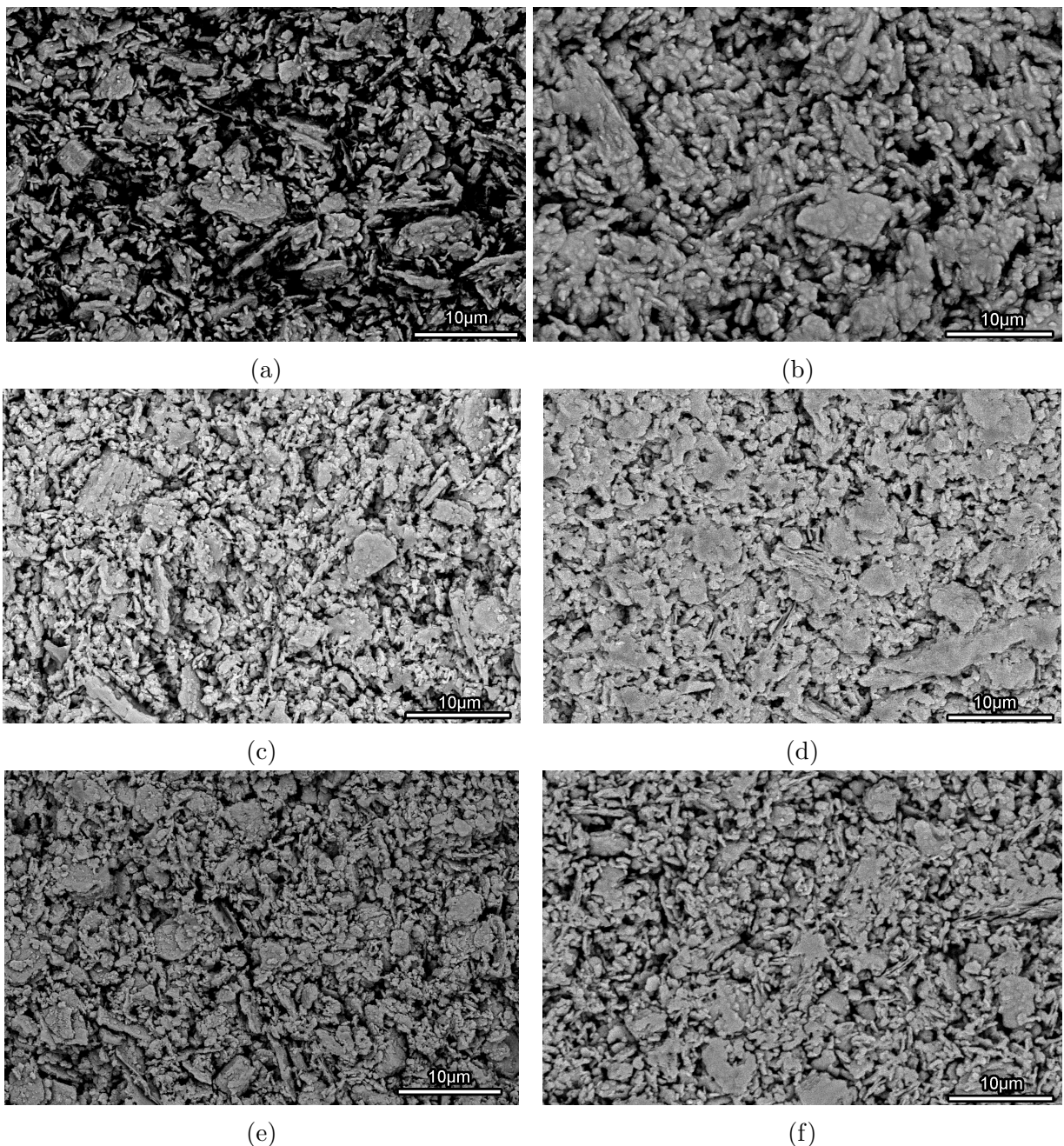


Figure 6.6: SEM-BSE micrographs of MK-NaOH at (a) 1d, (b) 7d along with MK-NaOH seeded with (c) 5% ZX at 1d, (d) 5% Zeolite X at 7d, (e) 5% SiO<sub>2</sub> at 1d, and (f) 5% SiO<sub>2</sub> at 7d

### 6.3.3 X-Ray diffraction

Zeolites A and X were observed to form in MK-NaOH geopolymers at ages  $\geq 28\text{d}$ , under sealed conditions at  $22^\circ\text{C}$ . A similar report of faujasites forming in metakaolin-sodium hydroxide geopolymers have been reported by Palomo et al., [108] demonstrating that the geopolymers can turn into zeolites under ambient conditions. Faujasite formation has also been observed in Class F fly ash-sodium hydroxide geopolymers cured at  $30^\circ\text{C}$  for  $100\text{d}$  [12]. Curing under elevated temperatures typically leads to shorter crystallization times [8].

XRD patterns in Figure 6.7 demonstrates that zeolite crystallization is delayed upon seeding. At  $28\text{d}$ , the control mix already shows the presence of zeolites A and X, whereas no zeolite phases were observed in the 5% SiO<sub>2</sub> and zeolite X seeded geopolymers. Literature on zeolite nucleation during synthesis is vast and these studies lead to the conclusion that zeolite seeds have differing effects in different systems [109–113]. For example, the addition of zeolite A seeds removed the induction period observed during the synthesis of zeolite A [114] and have been shown to accelerate the growth of zeolite A [111]. On the other hand, the application of seeds in the synthesis of zeolite A from dilute aluminosilicate solutions suppressed nucleation of new crystals and promoted the growth of seed crystals [113]. Another study demonstrated that the seeding directs the formation of new zeolite crystals [110]. A summary of nucleation in zeolites has been presented by Thompson [113], while Cundy and Cox have presented a detailed review on the hydrothermal synthesis of zeolites [115].

Owing to the widespread effects reported in literature, it is not possible to explain why would the addition of SiO<sub>2</sub> and zeolite X seeds suppress zeolite formation in geopolymers. Rees et al., have shown that the Al<sub>2</sub>O<sub>3</sub> seed can suppress the formation of faujasite in fly ash-sodium hydroxide geopolymers but they provide little explanation to as to why does alumina seed control the structure of zeolites forming in geopolymers. However, it is mentioned that the kinetics of zeolite crystallization are extremely slow in geopolymer mixes (at ambient temperatures) since re-arrangement of aluminosilicate species to form zeolites

are constrained in geopolymers mixes, which have much lower  $\text{H}_2\text{O}/\text{SiO}_2$  and much higher  $\text{OH}^-/\text{SiO}_2$  ratios. The ability of aluminosilicates to undergo re-arrangement probably linked to the porosity of the hardened microstructure. This hypothesis is based off the observation that high silica geopolymers ( $\text{SiO}_2/\text{Al}_2\text{O}_3 = 3.8$ , as described in Figure 4.3), which are known to possess low porosity values [20], did not form any zeolites upon ageing at  $22^\circ\text{C}$ . Therefore, the reduction in porosity due to seeding could have some role to play in the retardation observed in zeolite crystallization upon seeding.

It should also be noted that the addition of  $\text{SiO}_2$  clearly promotes the formation of zeolite X over zeolite A (with reference to the peak intensity ratio at  $6^\circ$  and  $7^\circ 2\theta$ , which corresponds to zeolite X and A respectively and is marked accordingly in Figure 6.7). This increase in formation of zeolite X could be arising out of a thermodynamic preference for zeolite X, which has  $\text{Si}/\text{Al}$  ratio  $>1$ , same as that of the 5%  $\text{SiO}_2$  seeded geopolymer ( $\text{Si}/\text{Al}$  ratio of 1.07). The control mix has a  $\text{Si}/\text{Al}$  ratio of 0.96, similar to that of Zeolite A, which has a fixed  $\text{Si}/\text{Al}$  ratio of 1. There may be other factors behind the preferential formation of zeolite X, since it is hard to understand why a slight increase in  $\text{Si}/\text{Al}$  ratio beyond 1 cause a drastic change in the relative proportions of zeolites A and X forming from the geopolymer.

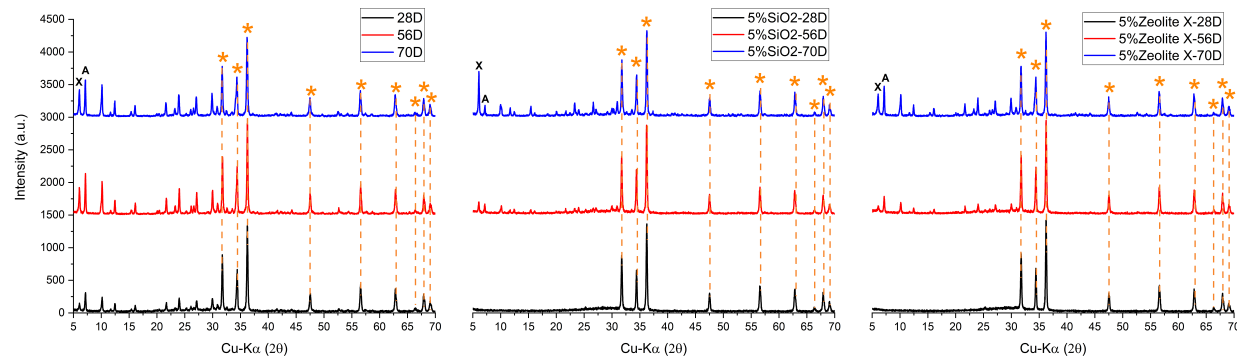


Figure 6.7: XRD patterns of seeded and unseeded MK-NaOH geopolymers at 28d, 56d and 70d. Bragg diffraction peaks from  $\text{ZnO}$  (internal standard) are marked with an asterisk

#### **6.3.4 Compressive strength**

Compressive strength data is presented in Figure 6.8 for the control mix and those seeded with 5% zeolite X and 5% SiO<sub>2</sub>. As expected from the decrease in porosity at 1d and 7d, mean compressive strength for seeded mixes was observed to be higher at both 1d and 7d. Adding 5% SiO<sub>2</sub> and zeolite X resulted in a strength improvement greater than 100% of control at 1d age. At 7d age, the SiO<sub>2</sub> mix exhibited  $\approx$ 33% higher compressive strength, and the zeolite X seeded mix showed a slight increase in mean compressive strength over control. However, at 28d age, both zeolite X and SiO<sub>2</sub> seeded mixes had significantly higher strength ( $\approx$ 66%) than control.

At  $>7$ d age, the strength of control mix was shown to decrease slightly, and the zeolite X seeded mix exhibited a large drop in strength from 28 to 56d. It should be noted that crystallization was seen to occur in both these binder mixes (at age  $<28$ d for control, and between 28-56d for zeolite X seeded mix) and crystallization is believed to cause a loss in strength for some geopolymers [106]. XRD indicates that the addition of SiO<sub>2</sub> led to a higher proportion of zeolite X over zeolite A, compared to control and zeolite X seeded MK-NaOH binders. Therefore, the results in Figure 6.8 appears to indicate that the formation of zeolite A is leading to a decrease in strength. However, no other conclusive evidence of this fact is presented in this thesis.

For practical purposes, nucleation seeding alone (i.e. considering mix with zeolite X) on the MK-NaOH geopolymers studied does appear to improve the amorphous product significantly till 28d age since  $\approx$ 66% higher strength was obtained upon seeding. In addition, early age ( $<7$ d) increase in compressive strength was also observed. However, this fact needs to be generalized by further testing on optimized, industrially relevant geopolymers.

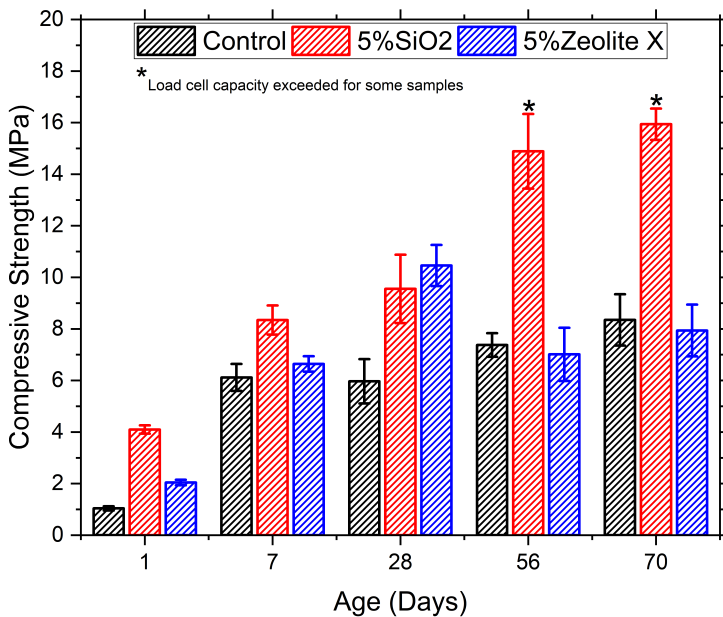


Figure 6.8: Compressive strength of geopolymers with and without seeds; Standard deviation from mean reported through error bars

## 6.4 Conclusions

The following conclusions can be made on the basis of the results and discussion presented in this chapter.

- Avrami model demonstrated that zeolite X and SiO<sub>2</sub> seeds can accelerate the geopolymer nucleation and growth. Nucleation was shown to be enhanced upon zeolite X addition (in comparison to SiO<sub>2</sub> addition), whereas addition of SiO<sub>2</sub> promoted nucleation and growth of gel.
- Seeding with SiO<sub>2</sub> and zeolite X caused a marked decrease in porosity at 1d age, which consequently manifests in an increase in compressive strength at the same age. A lesser extent of improvement in porosity was observed at 7d age, and compressive strength was enhanced only in the case of SiO<sub>2</sub> seeded mixes at the same age. 28d strengths for both the seeded mixes were  $\approx 66\%$  higher, showing that external seeding could have

some practical relevance. However, it appears that crystallization can be accompanied by strength loss in some cases, as observed in the zeolite X seeded MK-NaOH binder.

- XRD demonstrated that seeds retard zeolite crystallization, which was attributed to the low porosity in seeded mixes. SiO<sub>2</sub> seeds was observed to direct the formation of zeolite X over zeolite A at 70d. Therefore, it was concluded that seeds are not accelerating the formation of zeolites from geopolymers, a commonly observed phenomenon during zeolite synthesis.

# Chapter 7

## Salicylic acid extraction of aluminosilicates

*This chapter is based on the journal article draft for “Salicylic acid-methanol extraction of aluminosilicates”, prepared for submission to the Journal of American Ceramic Society. At the time of writing this thesis, the paper was not submitted yet. The NMR data reported in the chapter has been obtained by Dr. Xu Chen at the University of Illinois, and is included in this thesis for the sake of completeness. Dr. Leslie Struble served as a co-adviser on this project along with Dr. Paramita Mondal. The chapter is slightly different from the draft of the paper, with discussion on NMR spectra re-written.*

### 7.1 Introduction

Salicylic acid-methanol (SAM) extraction is a chemical dissolution technique used commonly in cement research to separate calcium silicates and free lime from anhydrous clinkers and cements [116]. This selective dissolution technique has been popularly used to study cement clinker morphology through electron microscopy and energy dispersive spectroscopy [116] and to improve phase content measurements through x-ray diffraction by removing interfering substances [117]. SAM solutions with certain salicylic acid-to-methanol ratios have found applications in enriching belite by selectively dissolving alite [118].

In addition to anhydrous cement, hydrated calcium silicate hydrate (C-S-H) in other cementitious materials can also be removed through SAM extraction. This was done to measure parameters like dissolution extent of blast furnace slag in OPC-slag cements [119] and characterize nature of hydration products formed in OPC-fly ash cements [120]. SAM

extraction has also been verified to dissolve synthesized C-S-H gels, as seen in a study from Garcia et al [121]. Their study also attempts to examine the nature of synthesized gels such as N-A-S-H gel and an intermixed C-S-H + N-A-S-H gel, through infrared spectroscopy (FTIR). SAM extraction was used to remove C-S-H from the mixed gel, but FTIR failed to characterize the changes upon SAM extraction. It was also not clear whether an intermixed C-S-H + N-A-SH gel was synthesized successfully, and therefore, no experimental evidence was obtained on whether N-A-S-H gels are immune to SAM attack. Interestingly, SAM extraction was not carried out on synthesized sodium aluminosilicate hydrates (N-A-S-H) because the authors believed that soluble calcium complexes drive dissolution of calcium silicates in SAM solution. Since N-A-S-H did not have any calcium, it was assumed to be immune to SAM attack.

Based on the same assumption, that N-A-S-H is immune to SAM, a two-step selective dissolution method was developed to characterize reaction products from alkali-activated fly-ash slag binders [26]. These binders are known to be a convoluted product of mixed C-S-H/C-A-S-H and aluminosilicate (N-A-S-H/K-A-S-H) gels [24–26], and the idea was to use SAM extraction to remove C-S-H/C-A-S-H. Subsequently a HCl extraction was done on the SAM residue to remove unreacted slag and geopolymer product. The removal of these phases at each step was verified through FTIR and spectral subtraction [26].

In a more recent study [122], during the two-step dissolution tests on sodium-silicate activated metakaolin geopolymers with external calcium, SAM removed C-S-H/C-A-S-H and unexpectedly some Q<sup>4</sup> silicate sites (which are associated with 3D structures, probably in N-A-S-H containing gel). Uncertainties when assigning these Q<sup>4</sup> sites as C-A-S-H were discussed and found not to affect final conclusions of the study, but no evidence was provided to understand how and why SAM removed the Q<sup>4</sup> silicate sites [122]. In our current tests (shown later), SAM extraction was seen to remove large quantities of a metakaolin-sodium hydroxide paste ( $\approx$ 60% mass loss) despite metakaolin possessing negligible calcium. To the best of our knowledge, there exists no explanation of the mechanism behind SAM extraction.

This study has two objectives, i) to confirm that SAM can dissolve three-dimensional aluminosilicates, ii) to understand the mechanism behind SAM dissolution of sodium aluminosilicates. A metakaolin-NaOH geopolymer and three synthetic zeolites, A, X and Y were used for characterizing the effects of SAM on aluminosilicates. These zeolites possess Si/Al ratios comparable to the geopolymer, and have the same short-range structure as geopolymers. The fact that zeolites are crystalline makes it easier to characterize the effects of SAM dissolution. To understand the mechanism of SAM extraction, mass losses in binders or zeolites were measured after SAM extraction and microstructural changes were characterized through scanning electron microscopy (SEM). X-Ray diffraction (XRD) was used to observe changes in crystalline structure of the zeolites while nanostructural changes were examined by Fourier transform infrared spectroscopy (FTIR) and nuclear magnetic resonance (NMR). Bulk chemical composition was measured by X-Ray fluorescence (XRF). In the subsequent paragraphs, it will be proved beyond doubt that SAM indeed attacks different aluminosilicates to various extents. The extent of attack was also revealed to be controlled by silica polymerization state in the aluminosilicate structure, and this opens the possibility of using SAM solution to characterize silica polymerization in no-calcium aluminosilicates.

## 7.2 Experimental Methods

### 7.2.1 Materials and Sample Preparation

Reagent grade salicylic acid (Sigma Aldrich) and methanol (Macron Fine Chemicals) were used throughout the study. Zeolite A synthesis was described in Chapter 3, using reagent grade fumed silica (Sigma Aldrich), sodium aluminate (Sigma Aldrich), sodium hydroxide pellets (Fischer) and Milli-Q (EMD Millipore) water. Zeolite X and Y were procured as commercial molecular sieves (Alfa Aesar). The metakaolin used to make geopolymers was procured from BASF chemicals. Metakaolin-sodium hydroxide

geopolymer (MK-NaOH) was prepared with the same 1:1:1.9:13.6 ( $\text{Na}_2\text{O}:\text{Al}_2\text{O}_3:\text{SiO}_2:\text{H}_2\text{O}$ ) molar stoichiometry as reported in Ch 4. At desired age, the geopolymer reaction was stopped by crushing the solid binder in an agate mortar and pestle in the presence of acetone-methanol [86]. The slurry was filtered using a Grade 1 Whatman Filter Paper and Buchner funnel, following which it was dried in a vacuum desiccator at moderate vacuum. This powder was utilized for all subsequent tests. The salicylic acid-methanol extractions were carried out at room temperature which was noted to be within 20-22°C for all experiments. SAM extractions were run by following the procedure laid down by Stutzman [117]: 4g of salicylic acid was dissolved in 60ml of methanol, into which 1g of sample was added. Adsorbed water in methanol was not accounted for or quantified in the SAM solution. The resulting solution was stirred for two hours on a magnetic stirrer and filtered through a Grade 1 Whatman filter paper supported on Buchner funnels. Any residue recovered was then dried at 105°C and the weight loss was measured. The residue was also run through XRD (in the case of zeolites), XRF and FTIR. HCl dissolution was carried out on the metakaolin geopolymers following procedures reported previously, to quantify unreacted metakaolin [26, 85]. Metakaolin was verified to be immune to SAM and HCl dissolution, with no mass loss and no change being observed in FTIR spectra of metakaolin before and after SAM and HCl extraction. In addition, NMR spectra (not presented here) of residue from HCl extraction of metakaolin geopolymers was seen to be the same as that of metakaolin. This shows that congruent dissolution of metakaolin takes place in NaOH solutions.

### 7.2.2 Methods

FTIR was carried out on a Perkin Elmer Frontier spectrometer. An attenuated total reflectance (ATR) accessory with a diamond crystal was used to carry out the measurement. XRD was carried out on a Siemens-Bruker D5000 diffractometer. Patterns were obtained at the rate of 1°/min, with a step size of 0.02°, X-ray emission current of 30mA and electron

gun voltage of 40kV. Single crystal silicon holder was used to reduce background noise in the powder diffraction pattern. Search and match for phase identification was carried out on MDI Jade Version 9.6. Rietveld analysis was carried out using TOPAS Version 5. Crystal structures were generated through VESTA, an open source software, using powder diffraction cards and crystallographic information files. XRF was carried out on a Shimadzu EDX-7000 instrument with a Rhodium x-ray source. The samples were analyzed in a helium atmosphere and an in-built fundamental parameters method was utilized to generate quantitative values. XRF results for the metakaolin and zeolites used in this study is shown in Table 4.1 and 7.1 respectively. Solid-state  $^{29}\text{Si}$  direct polarization (DP) magic angle spinning nuclear magnetic resonance (MAS NMR) tests were conducted on the zeolites and geopolymers specimens before and after the SAM extraction using a Varian Inova Spectrometer operating at 7.04 T. The pulse width was 2.5 $\mu\text{s}$ , a 90-degree pulse. Recycle delay was 30s and number of scans was 2048 for each test. Solid-state cross-polarization (CP)  $^1\text{H}/^{29}\text{Si}$  MAS NMR tests were conducted using the same spectrometer. The contact time was optimized to show the highest intensity. Recycle delay was 4.0s and 1024 scans were acquired.

Table 7.1: XRF composition of zeolites, in oxide weight %

Material	$\text{SiO}_2$	$\text{Al}_2\text{O}_3$	$\text{Na}_2\text{O}$
Zeolite A	42	35	23
Zeolite X	50	32	18
Zeolite Y	68	21	11

### 7.3 Results

The results are split into two sections. The first section covers the use of SAM on zeolites, and the second covers its use on metakaolin-sodium hydroxide geopolymers.

### 7.3.1 Zeolites

The structure of zeolite A has been described earlier in Sec 3.3.1. Our XRD patterns do not indicate the presence of any other crystalline phase and NMR spectra does not reveal any other silicon site apart from Q<sup>4</sup>(4Al) sites, proving that the synthesized zeolite A is phase pure. Upon running the SAM extraction on zeolite A, 100% dissolution was noted, which is quite contrary to the idea that SAM does not attack three-dimensional sodium aluminosilicate phases. The previously colorless solution was also noted to turn clear pink, confirming the occurrence of a chemical reaction. SAM extraction on zeolite X led to incomplete dissolution with a mass loss of 23%. The same pink color was observed, as seen earlier in the case of zeolite A. The solution was not clear, which confirms that full dissolution of the zeolites was not attained.

XRD pattern of zeolite X and the residue obtained after SAM extraction are shown in Figure 7.1, and the residue is seen to possess the same crystalline peaks, some of which have reduced intensity. No shift was observed in the peak positions which indicates that the lattice spacings of zeolite X are unaffected by the extraction. Infrared spectroscopy was used to obtain additional structural information on the zeolite X and its residue. The FTIR spectra presented in Figure 7.2 reveal two changes: the main peak from Si—O—T asymmetric stretching ( $\approx 970\text{ cm}^{-1}$ ) is situated at higher wavenumbers, and a small peak was seen to emerge around  $830\text{--}900\text{ cm}^{-1}$ . The former observation is well known to be a consequence of increasing Si/Al ratio in zeolites [123] due to dealumination. The latter observation has been seen to take place upon the formation of silanol groups in zeolite structures [123]. The peak at  $566\text{ cm}^{-1}$ , attributed to vibration from D6R (double six-membered rings) groups, was seen to be unaffected, indicating that the  $\beta$ -sodalite cages are still well linked to each other. XRF analysis indicates that the SAM residue does not contain any sodium, and Si/Al ratio has increased to 1.5 from 1.3, which confirms dealumination. Dealumination implies that SiO—Al bonds are broken and this can explain the emergence of silanol (SiO—H) groups. Analyzing the residue obtained from zeolite X through SEM (results not shown) did not

show any change in the size or morphology of particles after SAM extraction.

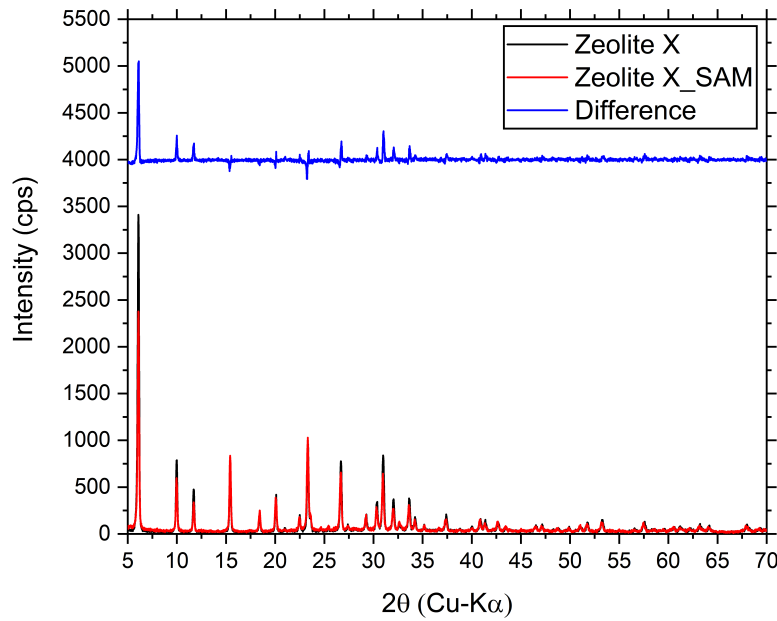


Figure 7.1: XRD patterns of Zeolite X, before (black) and after (red) SAM extraction.  
Intensity difference between the two patterns is also plotted (blue)

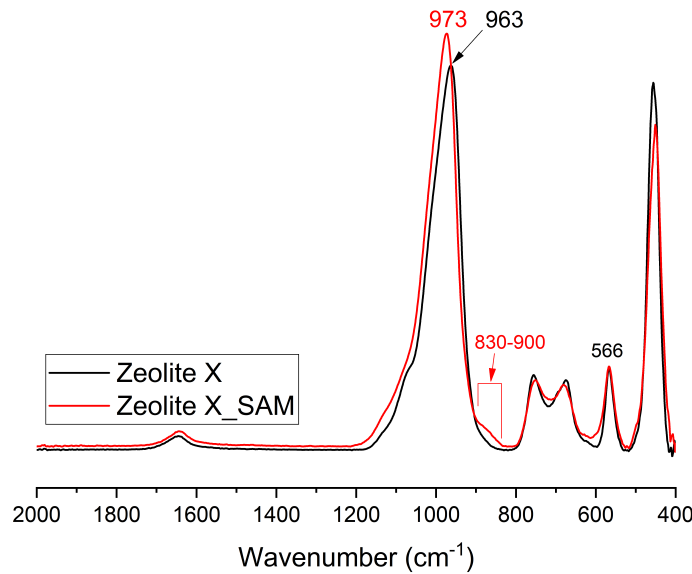


Figure 7.2: FTIR spectra of zeolite X before (black) and after (red) SAM extraction

Subsequently, Rietveld refinement was carried out to gain further understanding about the changes brought about by SAM extraction in the crystal structure of zeolite X. The structure of zeolite X was refined based on the crystallographic information file from PDF #97-006-5500. Subsequently, all the sodium sites in the refined structure were set to zero occupancy, as per from XRF and the diffraction pattern of the zeolite was simulated in Figure 7.3. Figures 7.1 and 7.3 are observed to exhibit similar trends, and the removal of sodium accounts for several of the differences in peak intensities between zeolite X and its SAM residue, most notably, the sharp decrease in intensity at  $6^\circ 2\theta$ . Dealumination was not accounted within the refined structure without sodium. Therefore, the difference patterns (in blue) between Figures 7.1 and 7.3 are not expected to be the same. Rietveld refinement details are provided in Appendix B.

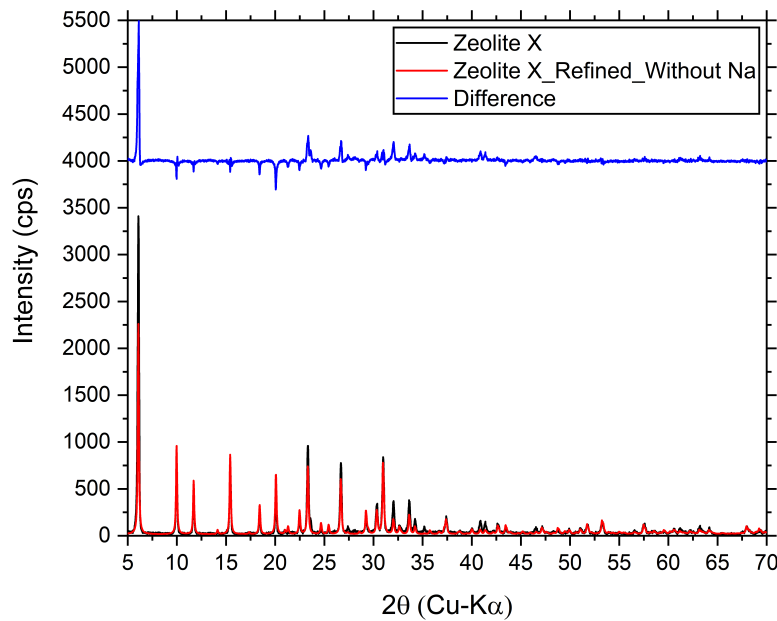


Figure 7.3: XRD pattern of zeolite X with (black) and without (red) Na, with the latter being obtained from Rietveld refinement. Intensity difference between the two patterns is also plotted (blue)

$^{29}\text{Si}$  DP MAS NMR spectra in Figure 7.4 confirms dealumination, with Q<sup>4</sup>(4Al) and Q<sup>4</sup>(3Al) peaks reducing in intensity after normalizing the NMR spectra of residue. All peak

assignments were made with references to peak positions reported by Lippmaa et al [37].  $\text{Q}^4(2\text{Al})$  and  $\text{Q}^4(1\text{Al})$  peaks were used to normalize spectra since these sites tend to remain unaffected by SAM solution, as described in the subsequent paragraph. CP MAS NMR spectra of SAM residue (not presented in thesis) showed increased intensity between -80 and -83 ppm in compared to the corresponding DP spectrum, which indicates the presence of Si–OH silanol groups, consistent with the FTIR results presented.

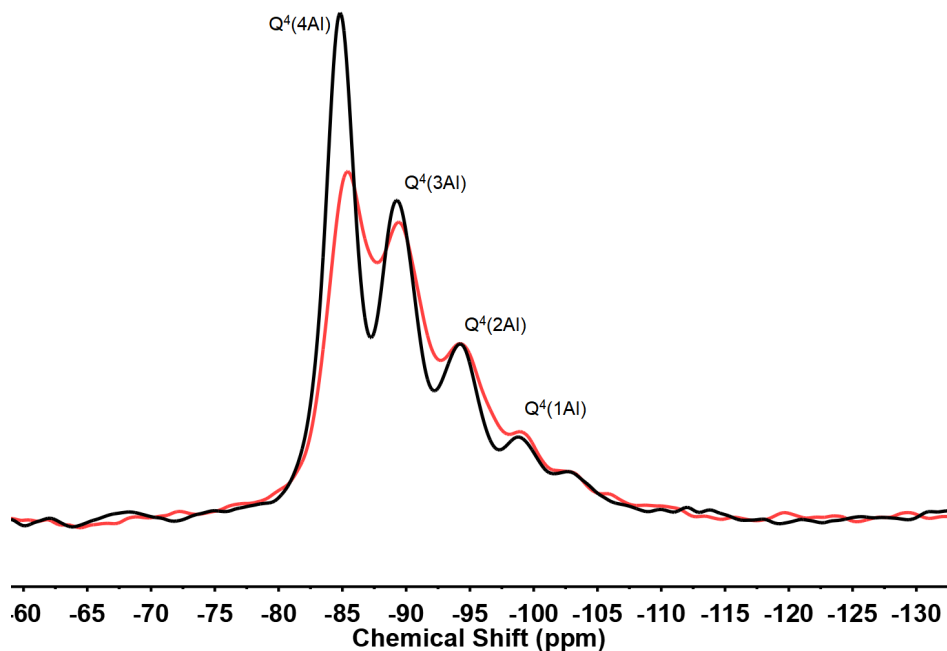


Figure 7.4:  $^{29}\text{Si}$  DP MAS NMR spectrum of zeolite X (black) and sam residue of zeolite X (red). Spectra of residue was normalized to ensure equal intensity levels at  $\text{Q}^4(2\text{Al})$  and  $\text{Q}^4(1\text{Al})$  peak positions for the two spectra

A third zeolite, zeolite Y was subjected to SAM extraction. This zeolite has the same crystal structure as zeolite X, but possesses a higher Si/Al ratio, between 1.5-3.0 [77]. Zeolite Y with Si/Al ratios higher than 2.35 has been characterized to possess  $\text{Q}^4(3\text{Al})$  and lesser Al substituted Si sites [77]. Si/Al ratio for the zeolite Y used in this study was 2.7, which suggests that  $\text{Q}^4(4\text{Al})$  sites are absent. The zeolite was observed to be completely immune to SAM extraction, as no changes in color of solution, FTIR spectra and XRD patterns were observed. XRF composition remained unchanged before and after the extraction as well. SAM solution was thus seen to attack aluminosilicates and the tendency

to get attacked appears to be controlled by the Si/Al ratio, and hence the Si environment within the aluminosilicate. Zeolite A, composed of Q<sup>4</sup>(4Al) silicon sites, was seen to be dissolved completely, whereas zeolites with no Q<sup>4</sup>(4Al) sites remained unaffected by the SAM solution. Zeolite X, which has some Q<sup>4</sup>(4Al) sites was seen to be attacked partially, which specifically suggests that the presence of Q<sup>4</sup>(4Al) silicon sites controls reactivity of aluminosilicates towards SAM attack.

### 7.3.2 Geopolymers

The mechanism of metakaolin-sodium hydroxide geopolymerization can be described broadly as a solution mediated, two-step process: dissolution and polymerization [9, 28, 50]. HCl extraction of MK-NaOH was utilized to quantitatively determine the unreacted metakaolin, and results are presented in Table 7.2, with standard deviation for four samples presented as uncertainty. Isothermal calorimetry data for MK-NaOH in Figure 7.5 shows that the reaction kinetics start slowing and the heat evolution rate is quite low after 3d. This combination of calorimetry and HCl dissolution data makes it clear that dissolution slows down from 1d to 7d; while polymerization of aluminosilicate is known to occur during this time, it remains uncharacterized using these techniques.

Table 7.2: Mass losses in SAM extraction and unreacted metakaolin from HCl extraction for MK-NaOH at 1d and 7d

Age of Sample	SAM Mass loss (%)	HCl Mass loss (%)	Unreacted Metakaolin (%)
1d	58±2	60±1	40±1
7d	72±1	88±1	12±1

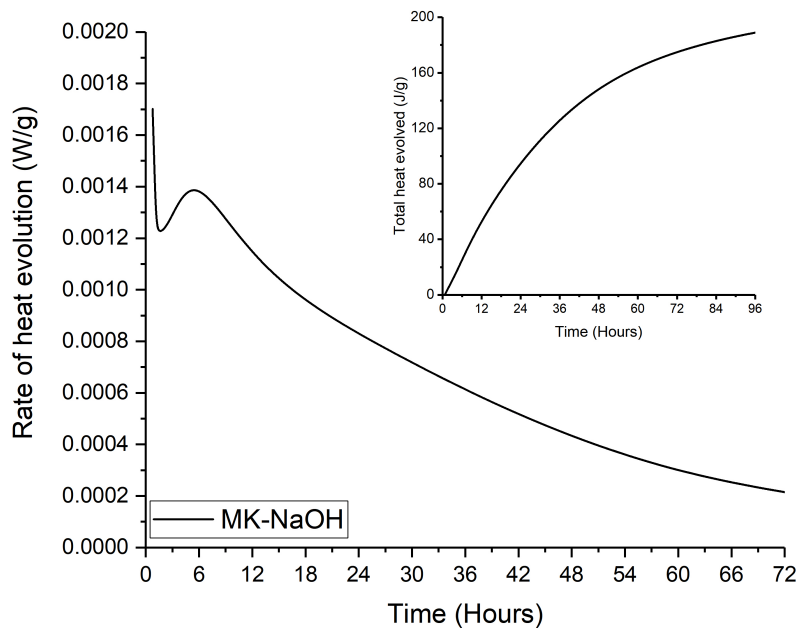


Figure 7.5: Isothermal calorimetry data for MK-NaOH

At 1d, response of MK-NaOH to SAM extraction is the same as HCl extraction, with both the extractions having the same mass loss. FTIR revealed the SAM residue to be metakaolin. A pink color was again observed in the solution, similar to what was seen in SAM extraction of zeolites. The pink color in SAM solution has also been observed when powders containing C-S-H were extracted.

At the age of 7d, it was seen that SAM extraction could not remove the geopolymer gel completely, and residue was not pure metakaolin. It is hypothesized that the structural changes within the gel from 1d to 7d causes the gel to become more resistant to SAM extraction. To identify these changes, FTIR spectra of MK-NaOH (Figure 7.6) were analyzed at 1d and 7d. For this study, band assignments are made only for peaks between 1200-850  $\text{cm}^{-1}$  using data for low-silica zeolites [123], and the literature review by Rees [124]. In Figure 7.6, the asymmetric stretching peak of Si–O–T bonds at  $1071\text{cm}^{-1}$  in raw metakaolin shifts to  $975\text{cm}^{-1}$  in the 1d spectrum. At 7d, the peak position is located at  $967\text{cm}^{-1}$ . This decrease in peak position is usually linked to greater aluminum substitution, or to low

silica polymerization. This analysis is valid when no other process other than aluminum incorporation or silica polymerization is involved. However, dissolution still takes place in these binders. The main peak of metakaolin, observed as a shoulder (indicated in Figure 7.6) at 1d is barely visible at 7d. The observation was supported by HCl dissolution data, which confirms further dissolution of metakaolin from 1d to 7d. The formation of geopolymer gel species could also result in the slight decrease of main peak position from  $975\text{cm}^{-1}$  and  $967\text{cm}^{-1}$  and thus it is hard to interpret any changes from main peak positions alone. The small peak centered at  $\approx 850\text{cm}^{-1}$  could be due to presence of silanol groups ( $\text{Si}-\text{O}^-$  or  $\text{Si}-\text{OH}$ ) and/or lattice vibrations in aluminum tetrahedra. As discussed by Rees [124], it is hard to interpret peaks in the region of 500-800  $\text{cm}^{-1}$ , since they could be generated from ring vibrations or symmetric stretching of  $\text{SiO}-\text{T}$  bonds. Nevertheless, slight differences were observed in the three peak positions (marked with vertical arrows in the normalized spectra within Figure 7.6) at intensities below  $850\text{cm}^{-1}$  for the 1d and 7d geopolymer spectra.

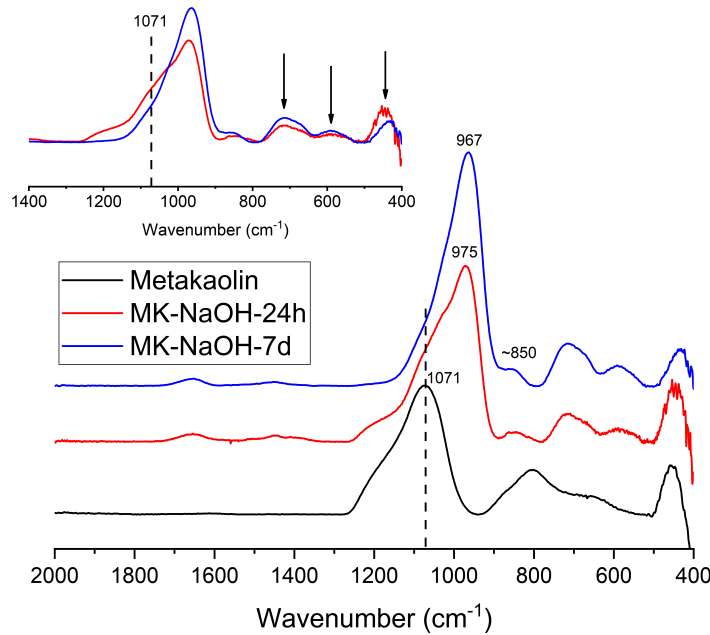


Figure 7.6: FTIR of Metakaolin (black), MK-NaOH at 1d (red) and 7d (blue). Normalized spectra are presented on the top left. Dashed black line indicates the position of asymmetric stretching peak at  $1071\text{cm}^{-1}$  for metakaolin

Figure 7.7 reveals that the main peak position for MK-NaOH at 7d increased from  $965\text{cm}^{-1}$  to  $1017^{-1}$  upon SAM extraction. XRF analysis shows that the Si/Al ratio remains the same before and after the extraction while the Na/Al ratio has reduced from 1.0 to 0.3. Thus, aluminosilicate gel with a Si/Al ratio of 1 was removed from the geopolymer. The response from unreacted metakaolin was thus magnified and contributes to peak intensity at higher wavenumbers as observed in the spectra. The difference in response to SAM attack between MK-NaOH at 1d and 7d is clearly arising from the structural changes resulting from the ongoing dissolution and polymerization. NMR spectroscopy is thus utilized to characterize these structural changes in the geopolymer.

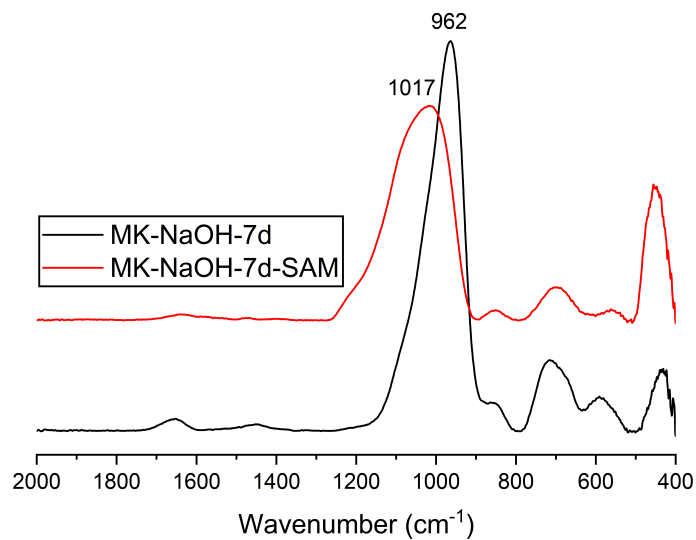


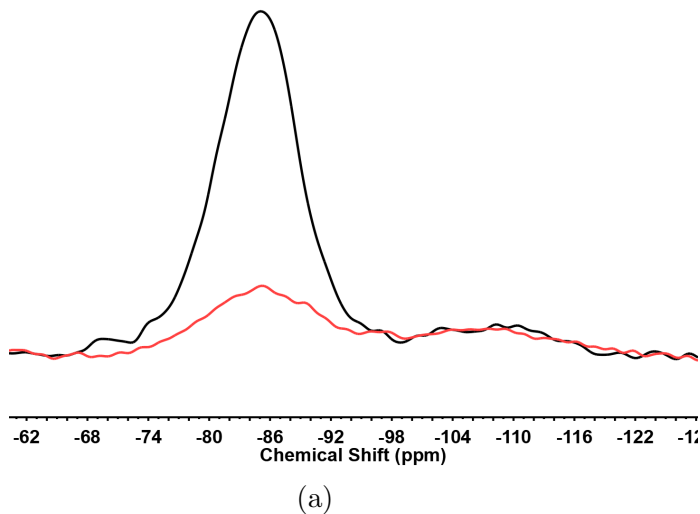
Figure 7.7: FTIR of Metakaolin (black), MK-NaOH at 1d (red) and 7d (blue). Normalized spectra are presented on the top left. Dashed black line indicates the position of asymmetric stretching peak at  $1071\text{cm}^{-1}$  for metakaolin

The  $^{29}\text{Si}$  MAS NMR spectrum of the MK-NaOH-1d (not shown) was found to contain Q<sup>4</sup>(4Al) geopolymer product and unreacted metakaolin. The residue was observed to be unreacted metakaolin, which confirms that the Q<sup>4</sup>(4Al) geopolymer was removed by SAM extraction. The  $^{29}\text{Si}$  MAS NMR spectrum of MK-NaOH-7d and its SAM residue are shown

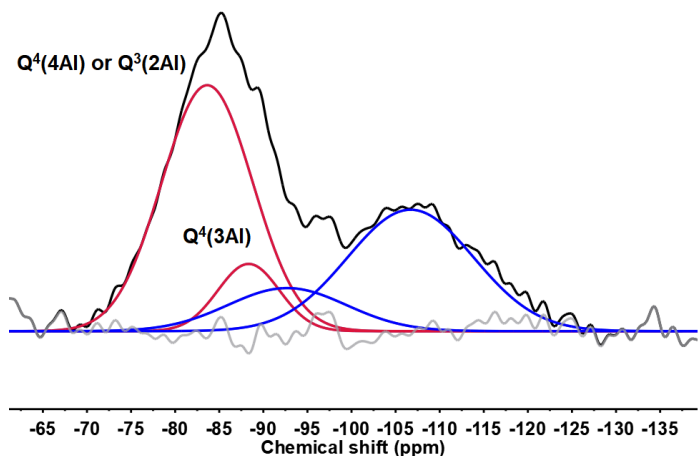
in Figure 7.8a. The two spectra were normalized to show the same intensity in the region between -110 and -120 ppm, which is attributed to the unreacted metakaolin and is expected to show the same intensity between these two spectra.

The NMR spectrum of the SAM residue was further deconvoluted as shown in Figure 7.8b. Two peaks were first assigned to metakaolin (blue). Cross-polarization spectrum (not shown) indicated a peak at -83 ppm, which falls in the range of peak positions for Q<sup>4</sup>(4Al) and Q<sup>3</sup>(2Al) silicon sites. Therefore, the MK-NaOH-7d SAM residue was deconvoluted further by adding one peak with the same width and chemical shift as observed in the CP spectrum. Height of the peak was determined by ensuring a good fit within the range of -70 to -80 ppm. Subsequently, another peak was added and assigned to Q<sup>4</sup>(3Al) to achieve a good fit, as shown in Figure 7.8b.

A separate attempt on deconvolution (not shown) was carried out by introducing a Q<sup>4</sup>(4Al) peak with the same width and position as the Si site removed by SAM, obtained by subtracting the two spectra in Figure 7.8a). This lead to three aluminosilicate peaks in addition to the two metakaolin peaks in the deconvoluted spectrum. The highest intensity of Q<sup>4</sup>(4Al) that could be achieved (while maintaining a good fit) was  $\approx$ 12% of the total intensity of the SAM residue. Therefore, the SAM residue at 7 days clearly possesses multiple Si sites in addition to the unreacted metakaolin. Some Q<sup>4</sup>(4Al) sites could still be present but their Si molar percent is no more than 12% of the total SAM residue.



(a)



(b)

Figure 7.8:  $^{29}\text{Si}$  DP MAS NMR spectrum for a) MK-NaOH-7d (black) and corresponding SAM residue (red). (b) shows the deconvoluted spectrum for the SAM residue, which contains an aluminosilicate (red), unreacted metakaolin (blue) and the residual spectrum (gray)

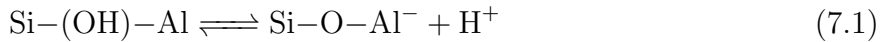
## 7.4 Summary and Discussion

SAM extraction on zeolite A which consists only of  $\text{Q}^4(4\text{Al})$  sites led to complete dissolution, whereas zeolite X which primarily possessed  $\text{Q}^4(4\text{Al})$  and  $\text{Q}^4(3\text{Al})$  silicon sites, was partially dissolved. Zeolite Y with very little  $\text{Q}^4(4\text{Al})$  sites [37] remained unaffected in SAM solution. Therefore, zeolites with  $\text{Q}^4(4\text{Al})$  sites are attacked by the SAM solution.

The results from SAM extraction on the MK-NaOH geopolymer are reminiscent of the observations seen from SAM extraction on zeolites A and X. Geopolymer product formed at 1d was revealed to consist only of Q<sup>4</sup>(4Al) silicon sites and was completely removed by SAM extraction, leaving behind metakaolin residue. However, at 7d, structural changes in the geopolymer led to the formation of Q<sup>4</sup>(3Al) and Q<sup>3</sup>(2Al) silicon sites. NMR revealed that SAM extraction led to the loss of Q<sup>4</sup>(4Al) Si sites, and the residue obtained after dissolution was no longer metakaolin.

Trends similar to the effects of SAM on zeolites were observed by Hartman and Fogler while studying the dissolution of zeolites in mineral acids [125]. Zeolite A was seen to dissolve completely in concentrated HCl (pH<1). Zeolites with higher Si/Al ratios such as analcime and Zeolite Y were seen to dissolve non-stoichiometrically, with aluminum being preferentially removed from the aluminosilicate framework. Their studies led to the conclusion that the dissolution was controlled by the presence of aluminum sites on the zeolite framework and was independent of the structure or framework of the zeolite itself. The observation of dealumination bears some similarity to what is seen from SAM extraction on Zeolite X. However, it is hard to describe acidity of salicylic acid in methanol (acids are described typically for aqueous solutions). Nevertheless, pH of SAM solution was measured to be 1.75. For reference, a saturated solution of salicylic acid in water (solubility being 2.55g/L of water at ambient temperature [126]) was observed to have a pH of 2.6. An additional experiment was conducted to verify if the SAM extraction is driven by its acidic character. Methyl salicylate (the methoxy ester of salicylic acid) was added to methanol in the same molar ratio as that of salicylic acid and methanol. The pH of the resulting solution was 5.6, much higher than that of SAM solution, since the acidic hydrogen in carboxylic acid is replaced with a non-acidic methoxy group. Zeolite X and MK-NaOH-7d geopolymer was observed to be immune to this methyl salicylate-methanol solution, which proves that the acidic hydrogen in the SAM solution plays a critical role in aluminosilicate dissolution. However, two observations remain unexplained: i) The selective removal Q<sup>4</sup>(4Al) Si sites in zeolites and geopolymers, and ii) incomplete removal of Q<sup>4</sup>(4Al) sites in the zeolite X.

To answer the first question, the Brönsted acidity of zeolites has to be understood. Brönsted acidic sites are developed in  $\text{SiO}_2$  tetrahedral structures when the  $\text{Si}^{4+}$  is substituted by  $\text{Al}^{3+}$ , leading to a negative charge developing in the lattice. This negative charge is compensated by a proton attached to the oxygen atom connecting neighboring Si and Al atoms. This  $\text{Si}-(\text{OH})-\text{Al}$  group is called the “bridged hydroxyl group” and is responsible for the Brönsted acidity of zeolites and a schematic is shown in Equation 7.1. [127, 128]



The chemical composition of aluminosilicates leads to a variation in the Brönsted acid strength of protons associated with bridged hydroxyl groups in the aluminosilicate. The total number of acidic sites depends on the Si/Al ratio in the aluminosilicate, with one proton being theoretically available for every  $\text{Al}^{3+}$  site. A decrease in Si/Al ratio has been observed to lead to an increase in stretching wavenumbers and chemical shift of the proton associated with the O–H bond in  $^1\text{H}$  MAS NMR spectrum [127]. In addition to experimental evidence, *ab initio* computations showed a decrease in the proton bond dissociation energy with increasing Si/Al content. Consequently, the acid strength of a given bridged hydroxyl group is controlled by the number of aluminum atoms in the next nearest neighbour (NNN) positions to the Al atom in the bridged hydroxyl group [127–129]. Therefore, the introduction of a weak acid like salicylic acid-methanol leads to the replacement of charge balancing sodium ions with protons. The covalent character of the O–H bond will increase with decreasing acidity (lower acidity means equilibrium of the reaction in Eq. 7.1 will lie to the left) and this will consequently weaken the Al-O bond [128]. On the other hand, zeolite Y with stronger acidic sites than zeolite X, owing to its higher Si/Al ratio, forms  $\text{Si}-\text{O}-\text{Al}^-$ . This structure is strongly bound to the  $\text{Na}^+$  cation and therefore, the cation is not replaced with the proton from salicylic acid. Zeolite Y, was therefore observed to be unaffected by SAM extraction. Therefore, the variation in Brönsted acidity of  $\text{Q}^4(4\text{Al})$  to  $\text{Q}^4(0\text{Al})$  sites is the likely reason behind the observation of selective removal of  $\text{Q}^4(4\text{Al})$  Si sites.

Subsequently, the weakening of Al-O bond enables the conjugate base of the salicylic acid to attack and remove Al by chelation. Such a mechanism is observed by other weak organic acids and chelating agents used for the dealumination of zeolites [130–132]. The importance of chelation will be used to understand the partial removal of Q<sup>4</sup>(4Al) sites in zeolite X. Prior to that, the existence of a chelating effect in the SAM dissolution mechanism was proven by dissolving the zeolite X in acetic acid-methanol solution with a pH of 1.75 (Acetic acid cannot form a bidentate complex like salicylic acid). A mass loss of 9% was observed, which, compared to 23% mass loss in the case of SAM solution clearly proves that chelation by salicylic acid is instrumental in the dealumination mechanism. Salicylic acid has been observed to form bidentate complexes with aluminum in a 1:1 [133, 134] or 1:2 (aluminum:salicylic acid molar ratio) [134] in acidic aqueous media of pH 2. The dealumination of the Al atoms associated with a Q<sup>4</sup>(4Al) Si site then leads to the removal of the Q<sup>4</sup>(4Al) Si atom itself, as observed through NMR.

It is hypothesized that there are steric hindrances that prevent the salicylic acid from attacking and removing aluminum below the zeolite crystal surfaces, and therefore, incomplete removal of Q<sup>4</sup>(4Al) sites are noted. A similar, incomplete dealumination was observed upon treating ZSM-5 zeolites with oxalic acid, which lead to the formation of a tris-aluminum oxalate complex. The size of the complex makes it impossible for diffusion inside the zeolite framework structure, which consequently leads to incomplete dissolution. In addition, the zeolite X crystal size is >2µm as observed from SEM, so steric hindrance to salicylic acid intrusion or outward diffusion of aluminum salicylates could be the reason to the incomplete dissolution observed. In comparison, the zeolite A crystal size was <0.5µm, as shown in Figure 7.9. A second hypothesis can also be proposed; protons associated with the bridged hydroxyl bonds are strongly bound to the oxygen in the O1 and O3 positions [128] as shown in Figure 7.10. Consequently, any Q<sup>4</sup>(4Al) Si site in those locations will also have a difference in acidity, which could be another reason to as to why a fraction of the Q<sup>4</sup>(4Al) sites were removed.

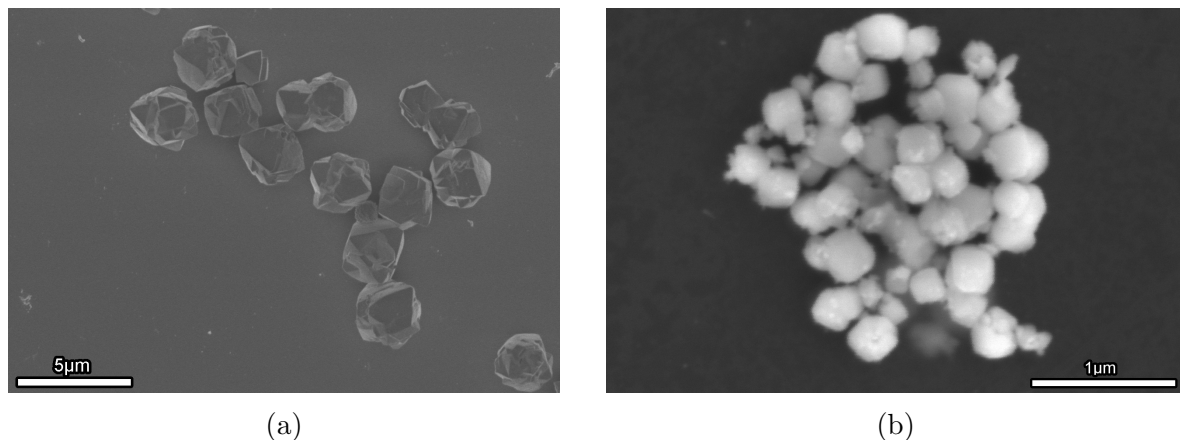


Figure 7.9: SEM micrograph of (a) zeolite X crystals, and (b) zeolite A crystals. Zeolites were dispersed on a carbon film supported on a TEM grid, and imaged without any sputter coating

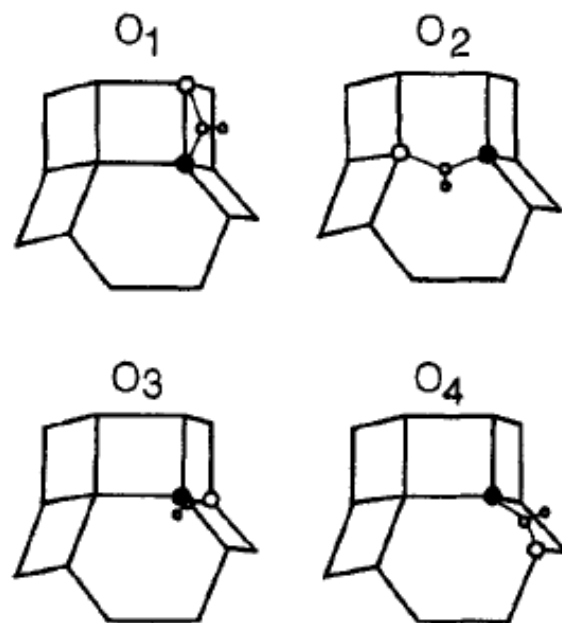


Figure 7.10: Different bridging hydroxyl sites for faujasites (adapted from [128])

## 7.5 Conclusions

In conclusion, it was proven beyond a doubt that SAM extraction can affect aluminosilicates. Dissolution is controlled by the presence of Q<sup>4</sup>(4Al) silicon sites. Therefore,

the SAM extraction method could potentially be used to characterize the presence of Q<sup>4</sup>(4Al) silicon sites in aluminosilicates. The mechanism of SAM extraction appears to involve an acid attack by salicylic acid. Bridged hydroxyl groups associated with Q<sup>4</sup>(4Al) silicon are the least acidic sites, owing to which the oxygen atom associated with these sites serves as a base and binds to the proton coming from the weak salicylic acid. Subsequently, the weakened Al-O bond is broken by the conjugate base of salicylic acid, which binds Al through chelation, and consequently, dealumination is observed. It is hypothesized that differences in acidity within the different bridged hydroxyl sites of zeolite X and/or steric hindrances to salicylic acid attack and chelation led to the incomplete removal of Q<sup>4</sup>(4Al) Si in zeolite X. However, no concrete evidence of these hypotheses are presented in this study. The results presented demonstrate conclusively that SAM extraction cannot be used to selectively dissolve calcium silicates from a mixture of calcium silicates and sodium aluminosilicates. On a different note, the results from SAM extraction on zeolites indicates that zeolite A has very low acid resistance. Hence, geopolymers with a higher proportion of zeolite A over X is expected to have poor acid resistance. On the other hand, adding 5% SiO<sub>2</sub> led to the formation of zeolite X over A. Therefore, SiO<sub>2</sub> addition not only enhances the microstructure and compressive strength (as reported in Chapter 6) but can improve durability of geopolymers to acid attack.

# Chapter 8

## Summary and Conclusions

The objective of this study was to characterize heterogeneous nucleation in metakaolin-sodium hydroxide geopolymers by adding external seeding agents. Changes in reaction rate of the metakaolin geopolymers upon adding nano TiO<sub>2</sub>, SiO<sub>2</sub>, zeolite A and zeolite X were monitored through isothermal calorimetry. HCl dissolution was used to quantify percentage of unreacted metakaolin in the geopolymer. These tests enabled formulation of hypotheses regarding a nucleation step in geopolymer formation. The hypotheses were subsequently tested on a synthesized aluminosilicate-sodium hydroxide geopolymer. The nucleation step was characterized by modeling geopolymerization kinetics (with and without seeds) using the Avrami equation. Subsequently, SEM-BSE was used to measure 2-D porosity in the geopolymers to quantify changes in porosity due to seeding. XRD measurements were taken at aged (28-70d old) samples to see if the nucleation seeds could direct the formation of zeolites in the metakaolin geopolymers. Compressive strength measurements were made on 1d-70d old samples to check for practical benefits of seeding. Key conclusions derived from these studies are listed as follows:

- The presence of a nucleation step was hypothesized from the increase in rate of heat evolution (at early age) upon the addition of seeds at dosage levels of 1%-5% wt. of metakaolin in mix. HCl dissolution also demonstrated faster dissolution of metakaolin upon seeding till 4h upon addition of TiO<sub>2</sub>, SiO<sub>2</sub> and zeolite X. Only nano SiO<sub>2</sub> seeded mixes were observed to undergo increased metakaolin dissolution, till 24h. Both these observations are characteristic of a nucleation step existing in geopolymer formation.
- On the basis of the above observations, it was hypothesized that zeolite X acts only as a nucleation seed, and affects the kinetic stage controlled by nucleation of product.

On the other hand,  $\text{SiO}_2$  is believed to react with dissolved alumina and form small aluminosilicate species, which serve as nuclei for further growth. In addition, the remaining  $\text{SiO}_2$  also participates in the growth of product, which means, it contributes to both nucleation and growth of product. However, it was noted from literature that the availability of dissolved alumina is key towards the growth of geopolymers-like, amorphous aluminosilicates.

- Adding excessive  $\text{SiO}_2$  in activator solution leads to complete nucleation site saturation, and the kinetics of geopolymers become purely growth controlled. Literature on amorphous aluminosilicate gels has proved that such growth controlled kinetics are controlled by availability of alumina in solution. Dissolution of metakaolin is slowed upon excess silica addition, and dissolved alumina is rapidly consumed by silica upon release. Therefore, availability of free alumina is limited and consequently, the reaction rate slows down.
- The synthesized aluminosilicate ( $\text{AlSi}$ ), despite possessing similar  $\text{Si}/\text{Al}$  ratio as that of metakaolin, exhibited extremely rapid, incongruent dissolution, with silica being released to solution preferentially over alumina. As a result, a metastable silica rich geopolymers were observed to form along with the metakaolin-sodium hydroxide type geopolymers product.
- The addition of nano- $\text{SiO}_2$  was observed to slow down the reaction kinetics, which was clearly due to the lack of dissolved alumina, required for product growth, as hypothesized earlier. On the other hand, zeolite X slowed down reaction kinetics drastically, but increased the proportion of MK-NaOH type geopolymers product forming w.r.t the silica rich geopolymers, proving that the zeolite X can nucleate the MK-NaOH geopolymers product.
- The Avrami nucleation and growth model was observed to fit early age reaction kinetics data (upto 12h) for MK-NaOH mixes and those seeded with zeolite X and  $\text{SiO}_2$  seeds. The combined reaction rate constant was observed to be higher for the zeolite X and

$\text{SiO}_2$  seeded mixes in comparison to the control mix, which added further evidence of these additives acting as nucleation seeds.

- Porosity measurements through SEM demonstrated that seeding with 5% zeolite X and  $\text{SiO}_2$  led to marked reduction in porosity at 1d age. A decreased porosity was also observed at 7d age. The microstructure refinements consequently manifested as increased compressive strength at 1d, although statistically significant improvements were observed only for the 5%  $\text{SiO}_2$  seeded mix at 7d. 5% zeolite X seeded mix exhibited significantly higher strength at 28d, w.r.t control.
- XRD on MK-NaOH showed that zeolite A and zeolite X is formed at the age of 28d. Seeding was observed to retard zeolite crystallization from amorphous geopolymers. This behavior was hypothesized to be due to the decreased porosity which offers hindrance to structural re-arrangement. 5%  $\text{SiO}_2$  seeded mix was observed to promote the formation of zeolite X over zeolite A, whereas the control and zeolite X seeded mix was observed to possess more zeolite A over zeolite X. Therefore, there is some evidence that seeds can also direct the structure of zeolite crystals derived from geopolymers.

A secondary objective involved understanding and elucidating the mechanism of aluminosilicate dissolution in salicylic acid-methanol solution. Synthesized zeolite A, commerical Type 13X (zeolite X) and zeolite Y molecular sieve, along with the metakaolin-sodium hydroxide geopolymers were the aluminosilicates tested with SAM solution. The zeolites and geopolymers, along with the residue left from SAM dissolution were characterized through XRD, XRD Rietveld, XRF, FTIR,  $^{29}\text{Si}$  MAS NMR and SEM. Key conclusions pertaining to this objective are presented as follows:

- In contrary to literature stating aluminosilicates are immune to SAM dissolution, this study revealed that SAM solution can dissolve low silica aluminosilicates containing  $\text{Q}^4(4\text{Al})$  Si sites.

- The mechanism of dissolution was concluded to be an acid attack, with the conjugate base of weak acidic bridged hydroxyl ( $\text{Si}-(\text{OH})-\text{Al}$ ) sites serving as the base. The acidity of these bridged hydroxyl varies with the presence of aluminum in the next-nearest-neighbor sites, and decreases in the following trend:  $\text{Q}^4(1\text{Al}) > \text{Q}^4(2\text{Al}) > \text{Q}^4(3\text{Al}) > \text{Q}^4(4\text{Al})$ . The Si sites referred to in the Q notation are the Si atoms connected to the bridged hydroxyl groups. Since salicylic acid is weak, only  $\text{Q}^4(4\text{Al})$  sites are selectively attacked. The other acidic sites are hypothesized to be stronger than salicylic acid and therefore, do not react with salicylic acid.
- Chelation of aluminum by salicylic acid led to dealumination in the zeolites and geopolymers. The removal of aluminum was also accompanied by loss of the attached  $\text{Q}^4(4\text{Al})$  silicon.
- The SAM dissolution does not selectively remove calcium silicate hydrates from a mixture of calcium silicate hydrates and sodium aluminosilicates, and the latter phases also dissolve in SAM solution. Therefore, the technique should not be used for selective dissolution in any future studies.

## Appendix A

### Micro-reactors in synthesized aluminosilicate

The synthesized aluminosilicate in Chapter 5 has been utilized in an attempt to use the micro-reactor approach described by [91, 92]. The synthesized was necessary since metakaolin is known to be unsuitable for generating micro-reactors [135]. Metakaolin particles are extremely fine, with an median particle size of around  $3\mu\text{m}$ . The particles are soft and flocculate easily; therefore it is hard to obtain single metakaolin particles. Post epoxy-impregnation, metakaolin particles can be removed through the polishing process [20]. Therefore, a controlled aluminosilicate with a larger particle size is required for the micro-reactors, and the synthesis of such an aluminosilicate has been described in literature [93]. The aluminosilicate can be synthesized with a Si/Al ratio of 1.0, which is similar to the metakaolin used in this study. The synthesis process for the material involves calcining at  $550^\circ\text{C}$  to obtain a hard mass, which is subsequently ground to a desired particle size. Therefore, the particles generated from this process can be tailored to a particular size, and are hard, which makes it suitable for use in the micro-reactor preparation procedure.

Micro-reactors are prepared by follows. Multiple single particles, around  $250\text{-}500\mu\text{m}$  in size, were placed on a silicone embedding mold (SPI Supplies) and an ultra-low viscosity resin (LR White) was used to impregnate the particles. The samples were impregnated by placing the submerged samples in a vacuum oven (vacuum pressure  $\approx 28\text{in Hg}$ ) for 18-24h. Subsequently, vacuum pressure was released and the oven set to  $60^\circ\text{C}$  for 24h. The resulting sample is shown in Figure A.1.

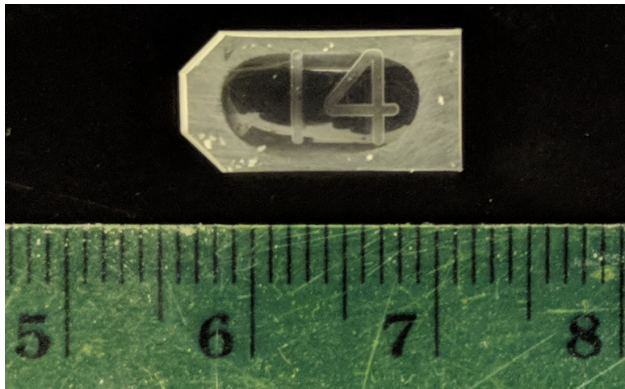


Figure A.1: Embedded single aluminosilicate particles; scale inset is in centimeters

The samples were subsequently polished lightly using 1000 grit SiC paper (for 30-60 seconds) to expose a surface of the aluminosilicate. Subsequently, 1200 grit SiC paper and 1 $\mu\text{m}$  diamond paste (on TexMet C cloth) was used to fine polish the surface. The resulting polished particles are shown in Figure A.2.

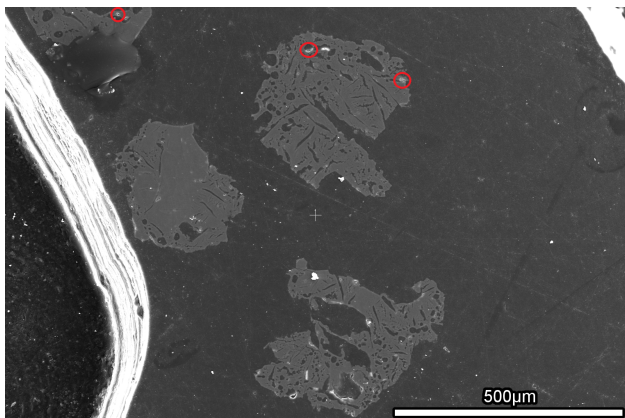


Figure A.2: Polished, resin impregnated aluminosilicate particles; small cracks from polishing and/or poor impregnation were observed (highlighted with circles)

A focussed ion beam SEM (Scios 2, FEI, United States) was used to mill microreactors 5 $\mu\text{m} \times 1\mu\text{m} \times 1\mu\text{m}$  in size. Ga ion beam was used, with a beam voltage of 30kV and beam current of 0.1nA. Each micro-reactor was milled in 2-3mins at these settings. Prior to milling, the surface of the embedded samples were sputter coated (Emitech K575, Quorum Technologies, United Kingdom) with a 30nm layer of Au-Pd. Resulting micro-reactor is shown in Figure A.3. Three micro-reactors were prepared on each particle to ensure

repeatability of any observations reported.

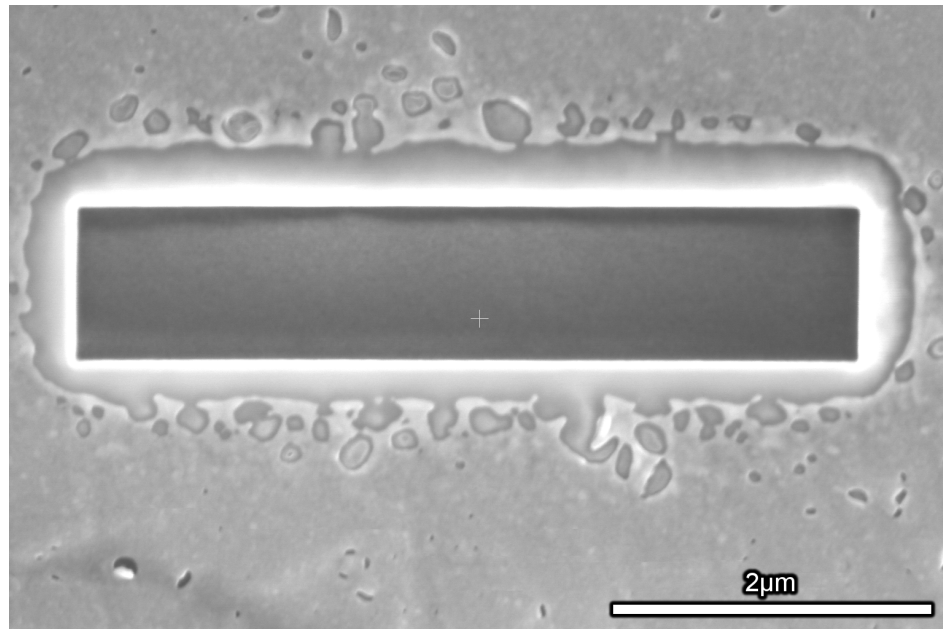


Figure A.3: FIB milled micro-reactors on a synthesized aluminosilicate particle

Subsequently, the micro-reactors were immersed in 1M NaOH solution for 2h, 24h and 48h. 2g SiO<sub>2</sub> was dispersed in 100ml of 1M NaOH solution, to observe the effect of nano-silica on the micro-reactors. The samples were immersed in 15ml of NaOH solution taken in a 50ml centrifuge vial, and a low vacuum pressure (4-5in Hg) was applied to introduce the solution into the milled gaps. Subsequently, the centrifuge vials were sealed off and stored at room temperature for the desired time. It should be noted that Suraneni and Flatt used around  $1.0 \pm 0.2$  ml of solution for carrying out the experiments. Such a step was not possible because the sodium hydroxide sample either evaporates under ambient conditions, or carbonates heavily if stored at 100% RH. A SEM micrograph of this issue is shown in Figure A.4. Keeping the samples submerged and sealed ensures that there is minimal loss of solution through evaporation and negligible carbonation.

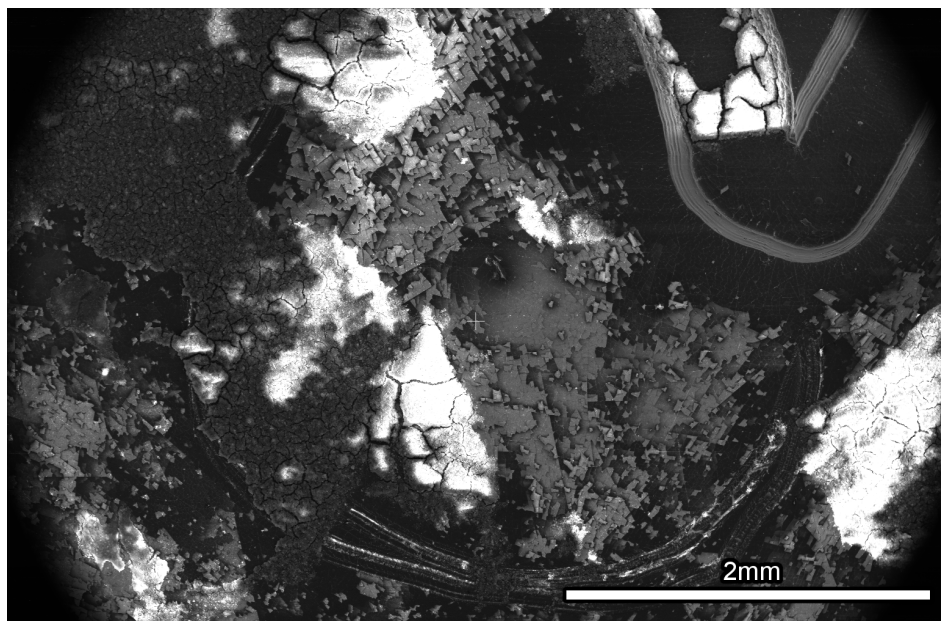


Figure A.4: Micro-reactor after 24h exposure to 200 $\mu$ l 1M NaOH solution, maintained at 100% RH

To stop the reaction, the sample was taken out of NaOH solution, and immersed in 50ml of 1:1 acetone-methanol solution (by volume) for 2h. Subsequently, the sample was removed and dried under vacuum (20in Hg vacuum pressure). Micro-reactor exposed to 1M NaOH for 2h is shown in Figure A.5, and is the only sample that did not exhibit any issues. Clear dissolution by pit formation is observed in the micrograph. This was the only set of data that had conclusive findings, and other measurements were plagued by two major issues, as explained in the following paragraphs.

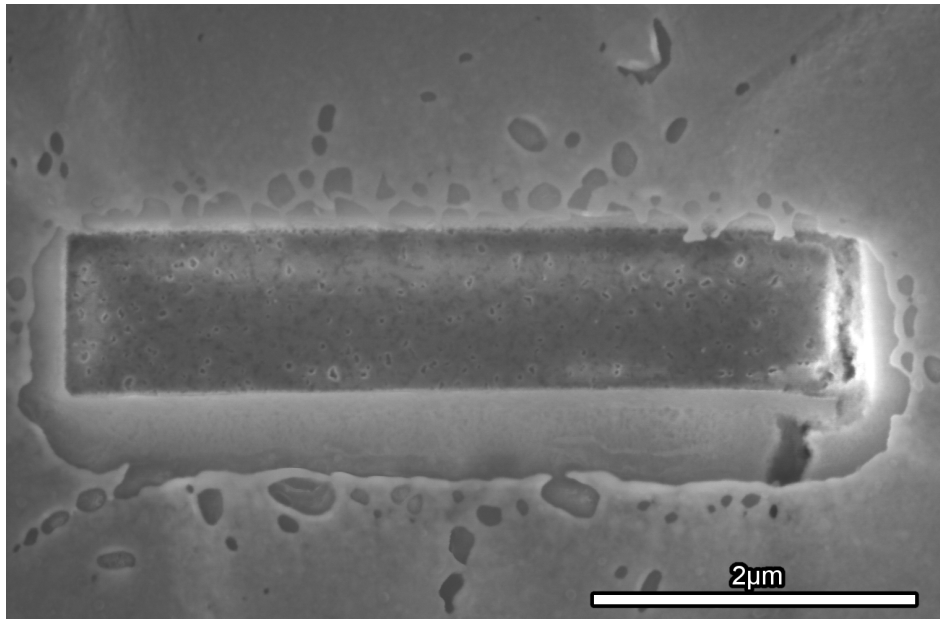


Figure A.5: Micro-reactor after 2h exposure to 1M NaOH solution

Micro-reactor exposed to NaOH solution with SiO<sub>2</sub> for 2h is shown in Figure A.6. The micrograph shows that the Au-Pd layer has shifted and is now partially covering the milled gap, therefore obstructing the view of the reactor bottom. Despite the obstruction, it appears that the presence of silica in solution accelerated the dissolution of the reactor base, with a small fissure around 3μm long being observable. Small pits are also observed although the features are not well resolved. The evidence is not conclusive since no other intact micro-reactors were obtained; other reactors had the issue with shifting Au-Pd layers.

The reason for the shifting Au-Pd layer is due to exposure of the sample to acetone-methanol. LR White resins weakens in acetone-methanol, and has a tendency to warp. Consequently, the Au-Pd layer shifts, and prevents clear imaging of the micro-reactors. An image of a sample exposed to 24h of acetone-methanol is shown in Figure A.7, and considerable damage can be visually observed due to the exposure to solvent. One way to address this issue would be to carry out solvent exchange in iso-propanol, which was observed to leave LR White intact.

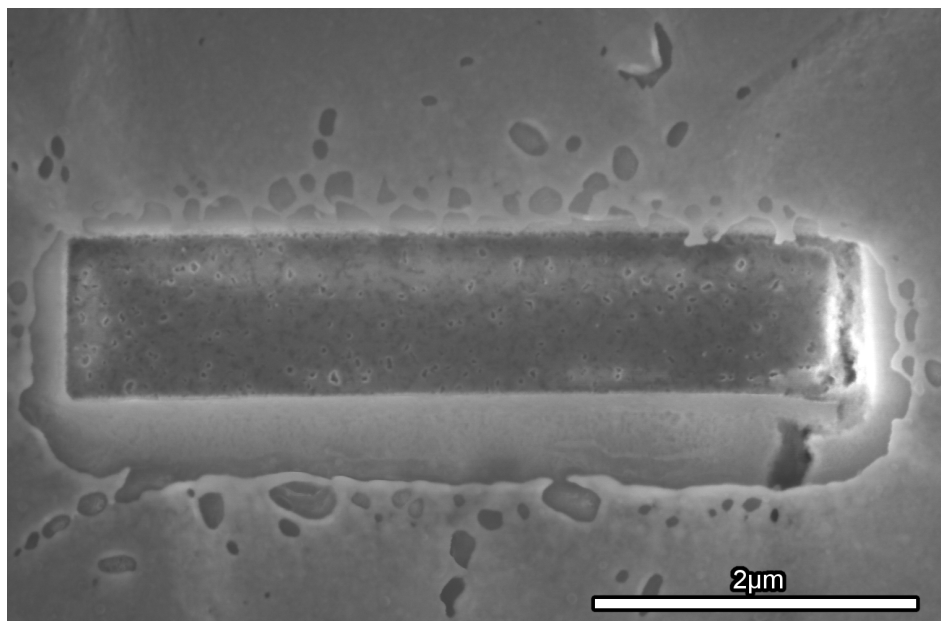


Figure A.6: Micro-reactor after 2h exposure to 1M NaOH solution containing  $\text{SiO}_2$



Figure A.7: LR White after 24h exposure to acetone-methanol

The second issue arose from the nature of synthesized aluminosilicate particles. In Chapter 6, it was reported that the aluminosilicate reacts extremely rapidly with NaOH solution. Consequently, it was observed that the embedded particles, despite having the 30nm Au-Pd layers get destroyed completely when imaged at 24h. Two examples of this behavior is shown in Figure A.8. Figure A.8a shows that the aluminosilicate particle disintegrates after 24h and micro-reactors can no longer be imaged. It is believed that the small gaps in the

sample (Figure A.2) lead to NaOH intrusion and reaction inside the sample. Consequently, dissolution and product formation leads to the destruction that is evident in Figure A.8a. On the other hand, Figure A.8b exhibits some kind of product formation on the top of the aluminosilicate particle in the presence of  $\text{SiO}_2$ , which could either be geopolymers or carbonation. Nothing conclusive could be obtained from these micrographs, and in either case, micro-reactors could not be imaged. Therefore, it appears that the reactive nature of the aluminosilicate makes it unsuitable for the micro-reactor experiments described in this appendix.

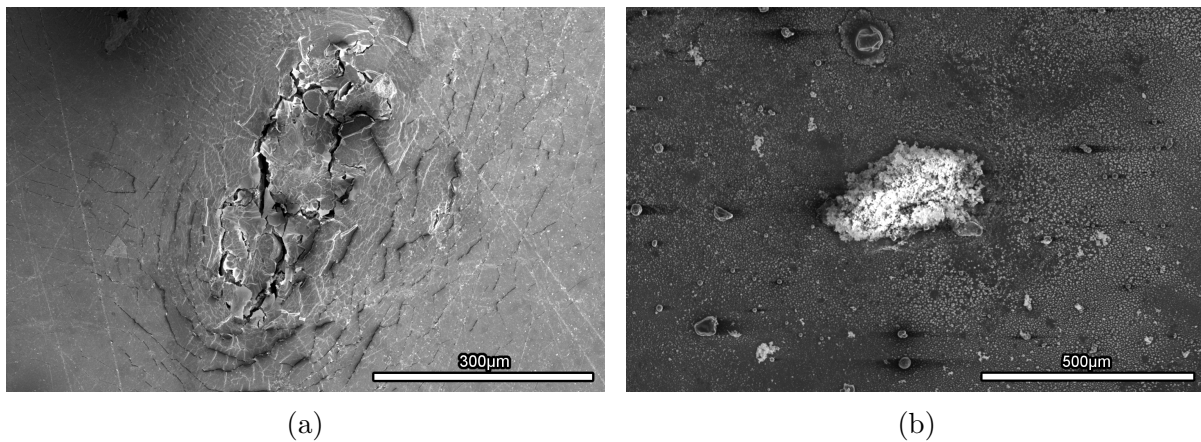


Figure A.8: Micrographs of aluminosilicate particle (a) after 24h exposure to 1M NaOH solution, and (b) after 24h exposure to 1M NaOH solution with  $\text{SiO}_2$

## Appendix B

### Rietveld refinement procedures

Rietveld refinement was carried out using TOPAS, Version 5 from Bruker AXS. Type 13X molecular sieve or zeolite X was refined to understand the effects of salicylic acid-methanol (SAM) on the unit cell structure. The same procedure was applied to the synthesized semi-crystalline zeolite X (described in Chapter 3) to quantify amorphous phase percentage within the zeolite X.

For the refinements, two Cu-K $\alpha$  peak wavelengths were considered within incident radiation, with wavelengths of 1.540596 $\text{\AA}$  and 1.544493 $\text{\AA}$ . Lorentzian peak shape was considered for the incident radiation, with half-widths of 0.501844 and 0.626579 $\text{\AA}$  for the peaks respectively. No refinement was carried out on these parameters. Background fitting was carried out using a Chebychev least-squares-fit algorithm. Goniometer radius was adjusted to the one on the instrument. Background fit results are displayed in Figure B.1.

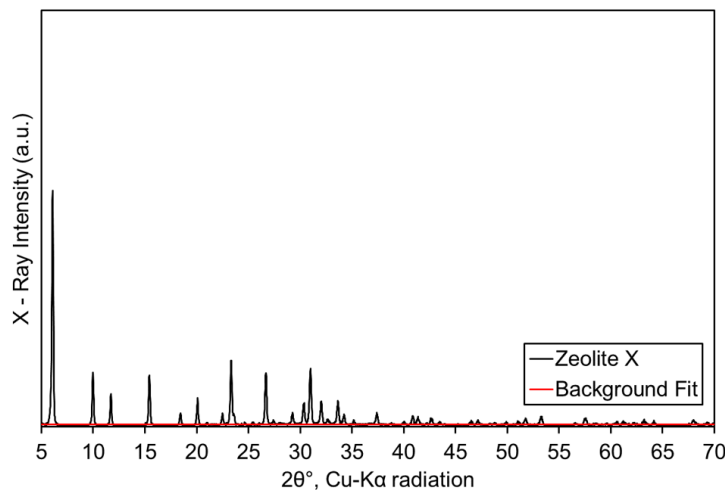


Figure B.1: Background fit obtained on zeolite X used for studying SAM dissolution

Upon obtaining the background, correction for sample displacement from holder was

set to be refined since there is some likelihood of the sample surface not being flush with the surface of the single crystal holder used. The structure to be refined was taken from the powder diffraction file (PDF) identified by MDI-JADE after the phase-match process. A hydrated, sodium exchanged Zeolite X with PDF #97-006-5500 was identified as the closest structure to the powder sample. Crystallographic information file associated with the PDF was obtained from Inorganic Crystal Structure Database (ICSD) for Rietveld refinement. Space group associated with the crystal structure is Fd-3Z (No. 203).

Within the crystal structure, the lattice parameter, crystal size and intensity scale were set to be refined. The lattice parameter had a value of 25.031 $\text{\AA}$  before refinement. A fundamental parameters approach, in-built within TOPAS was used for fitting peaks in the pattern. A pseudo-Voigt profile was also used but the fit quality did not change. Refining these parameters alone did not lead to a good fit, with discrepancies in peak intensities. Subsequently, the atomic coordinates and occupancy values were refined. The crystal structure had two unique silicon sites and one aluminum site which was shared with one of the silicon sites. The occupancy of the latter site, for silicon and aluminum separately could not be estimated since there is a difference of one electron between the two elements and leading to small changes in x-ray scattering. Fit was thus carried out by removing the aluminum site from the structure. One of the sodium sites was a special site, and was not refined. Other sites were refined as per rules laid out in the international tables of crystallography. An isotropic temperature factor in the refinement,  $B_{eq}$  was approximated to a fixed value of 1.5 (assuming bond lengths of 2.25 $\text{\AA}$ ). The pattern was subsequently simulated by setting the Na occupancies to zero, in Figure 7.3.

The temperature factor was fixed since it does not affect the fit significantly. The insensitivity of the temperature factor towards the diffraction pattern arises due to the large number of atomic positions in the unit cell (1534 atoms). The temperature factor leads to intensity discrepancies however, the occupancy factor outweighs the effect of the thermal atomic vibrations. A small decrease in occupancy leads to a large loss of atoms (and hence

electrons, which scatter x-rays) leading to larger changes in intensity values. This point is made clear by varying  $B_{eq}$  values in the refined structure and plotting the  $R_{wp}$  values, which characterizes the goodness-of-fit in TOPAS [136]. The fit quality barely changed, and was reflected in the small change in  $R_{wp}$  values, illustrated in Figure B.2.

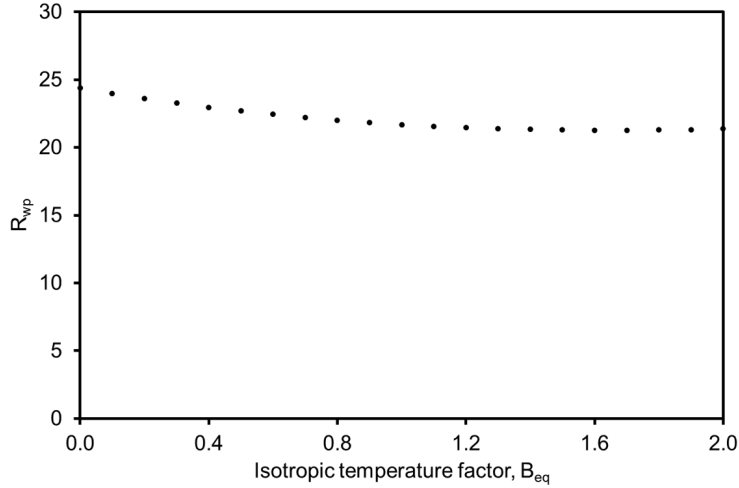


Figure B.2: Effect of changing isotropic temperature factor ( $B_{eq}$ ) on fit quality, represented by  $R_{wp}$

The first peak in the refined fit of zeolite X had issues with peak shape but could not be corrected through the means present in TOPAS. Apart from that, fit was seen to be good across the other  $2\theta$  values. The chemical plausibility of the refined structure is discussed further. Lattice parameter had reduced slightly, to  $24.951\text{\AA}$  after the refinement. Some of the atomic coordinates have shifted by less than  $0.05\text{\AA}$ . XRF data in Table 7.1 measured the atomic fraction of  $\frac{Si+Al}{Na}$  to be 2.52. In the Rietveld refinement, due to the exclusion of the aluminum site, the ratio of silicon to sodium atoms is the same as  $\frac{Si+Al}{Na}$ ; and the former value comes out to be 2.51. Given the close match to experimentally measured stoichiometry, small changes in lattice parameters and atomic coordinates, the structure can be considered to be chemically plausible. Since a good fit was obtained and the refined structure is chemically plausible, the quality of the Rietveld refinement was judged to be acceptable [137].

## Appendix C

### Alternate porosity measurements

Chapter 6 described the various issues concerning accuracy of porosity measurements as obtained by image analysis of SEM-BSE micrographs. Therefore, alternate porosity measurements were carried out, in an attempt to verify the accuracy of porosity measured through SEM imaging. The alternate method involves measurements of the bulk specific gravity (B) and absolute specific gravity (G). Bulk specific gravity is essentially the ratio of the mass of sample to the volume of sample (inclusive of pore volume and air voids). Absolute specific gravity is the ratio of mass of sample to the volume of solids present within the sample. Porosity of the sample is calculated by the Equation C.1.

$$\text{Porosity} = \left(1 - \frac{B}{G}\right) \times 100 \quad (\text{C.1})$$

Bulk specific gravity was measured by procedures laid out by ASTM C914, which involves coating the sample with wax of known density. Mass of the wax can be measured by weighing the sample before and after the coating. Subsequently, the volume of wax can be calculated by using its density. Total volume of the wax coated sample can be obtained by Archimedes principle, with the sample being immersed in methanol. Water is not used since the bulk density of the sample is less than 1, and therefore the wax-coated sample floats on water. Without the wax coating, methanol will always impregnate the sample and lead to inaccurate measurements of bulk density.

Absolute volume (or volume of solids) was measured by a gas (Helium) displacement pycnometer (AccuPyc 1330, Micromeritics), which relies on Boyle's law of ideal gases ( $PV = \text{constant}$ ; P - pressure, V - volume) for absolute volume measurements. This value was

used in conjunction with mass of the sample to yield absolute specific gravity.

Two different cylindrical samples, one with 0.5" dia, and 1" length and one with 0.25" dia and 0.75" lenght were used to perform the porosity measurements. PMMA molds were utilized for preparing these specimens. Samples were demolded after 24h and were maintained under sealed conditions before and after demolding. At the testing age, the samples were submerged in acetone-methanol (1:1 by volume) for 24h at moderate vacuum (20in Hg vacuum pressure). This step was followed by 30s of ultrasonication in fresh solvent to get rid of any loose particles adhering to the sample. This cycle of submerging in acetone-methanol and ultrasonication was repeated again. Subsequently, the samples were dried under vacuum for 24h, and then used for porosity measurements. However, there are two issues which leads to questionable porosity measurements, and they are described as follows.

The first issue is linked to the presence of air voids inside the sample. Metakaolin geopolymers of the composition used are exceedingly sticky, and it is very hard to remove entrapped air. Methods of consolidation used were: i) Tamping the sample with a micro-pipette while it is being vibrated and ii) subjecting the sample to vacuum (at 28in Hg vacuum pressure). Both these methods have inherent drawbacks. Severe leakage was observed when the samples were compacted by using the vibrating table. On the other hand, the exposure to vacuum leads to a loss of moisture from the surface, and the often the sample spills out of the mold while being kept under vacuum. Nevertheless, the vacuum was probably the only way to ensure that there are no air voids in the sample, and was used for the measurements reported in this appendix. Bulk specific gravity measurements for two MK-NaOH-5%zeolite X samples at 1d age came out to be  $0.886 \pm 0.01$ . Specific gravity for all samples range from 2-2.15. Therefore, porosity comes out to be in the range of 55-60%, compared to 30% reported from SEM image analysis. The reason behind this discrepancy remains unexplained, and further porosity measurements were not made.

The second issue is associated with the absolute specific gravity measurements derived

from the pycnometer. The samples can be used in the cylinder form as is, or can be crushed into a powder and then placed into the pycnometer. Values taken from both measurements do not fall on the line of equality, instead, the crushed absolute specific gravity always come out to be lesser than the specific gravity of the whole cylinder as shown in Figure C.1. The purpose of crushing is to ensure that the pores in the sample are open to helium intrusion, and therefore, absolute volume reported for the powdered sample should be lesser than that of the whole cylinder. Therefore, the specific gravity should be more for the powdered sample instead of lesser, as observed from Figure C.1. One possible reason is that the crushing action could have led to the loss of water, which resulted in the decrease in volume of solids.

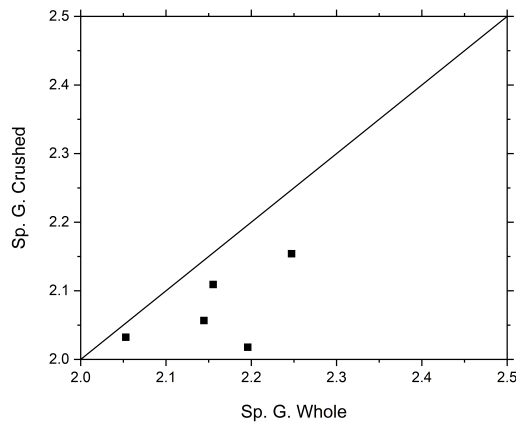


Figure C.1: Specific gravity of cylindrical sample vs. powder obtained by crushing the sample

Owing to these two issues, complete testing was not carried out on all the samples. Porosity from SEM image analysis appeared to be close to porosity values reported for similar metakaolin-sodium hydroxide mixes in literature. Therefore, it appears that there is some source of error in the alternate porosity measurements reported in this appendix.

## Appendix D

### Ultrasonic wave reflection measurements

Ultrasonic shear wave reflection (UWR) measurements were carried out to characterize any changes in hardening rate upon seeding in MK-NaOH geopolymers. The ultrasonic wave reflection technique is a setup developed in our laboratory based on the work carried out by Öztürk et al [138]. The setup utilized a 2.25MHz contact type, s-wave transducer connected to a pulser-receiver unit (P5077, Panametrics). The pulser-receiver was interfaced with a PC through a PCI-digitizer (NI5102, National Instruments). Geopolymer paste was poured in a high impact polystyrene (HIPS) container, with the transducer fixed to the bottom of the container by phenyl salicylate (which also acts as the couplant). The s-wave reflection coefficient at the interface between the paste and HIPS was monitored with time, to understand rate of hardening in the geopolymer paste. A description of the setup and its use in characterizing hardening rate in alkali-activated binders is presented elsewhere[24, 86, 139, 140]. However, UWR measurements for hardening rate yielded unexpected results. This appendix presents a description of these results and a probable cause behind the observations.

The working of the setup was verified by running s-wave UWR measurements on cement paste with w/c ratio of 0.44, shown in Figure D.1. The repeatability of the UWR measurements were observed to be of the same order as reported by Chung [141]. The induction period, as measured through isothermal calorimetry was also found to correlate well with the UWR data (shown in Figure D.2). Therefore, it is clear that the setup is in good working order, and issues from the measurement (if any) must be stemming from the sample being used.

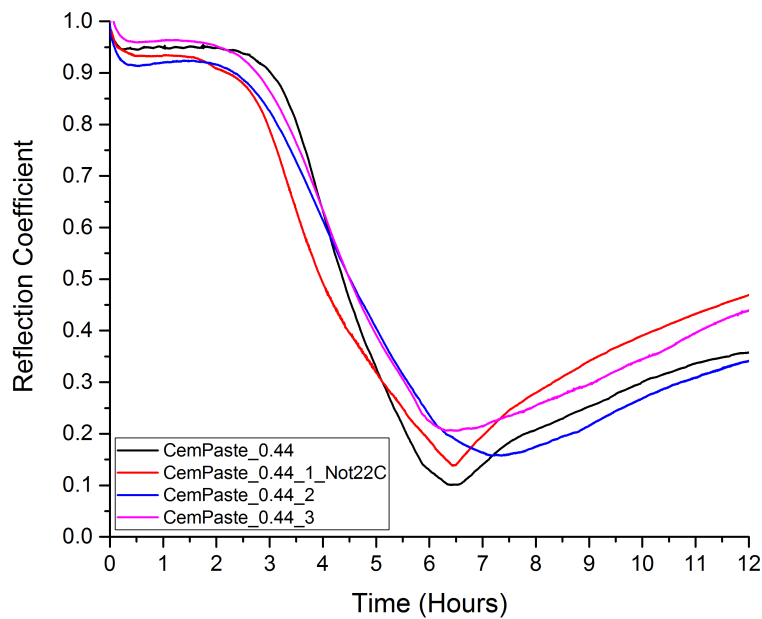


Figure D.1: Repeat measurements of cement paste ( $w/c = 0.44$ ) hardening, using s-wave UWR

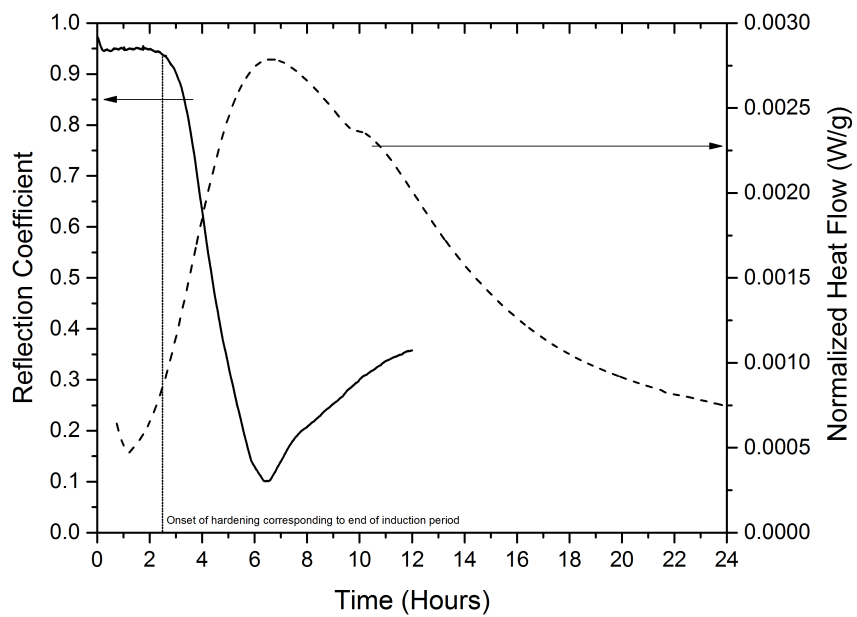


Figure D.2: UWR and isothermal calorimetry data of cement paste ( $w/c = 0.44$ ) at  $22^\circ\text{C}$ . The end of the induction period through UWR correlates well with the end of induction period as measured by isothermal calorimetry (indicated through the vertical dashed line)

Eight repeats of s-wave UWR measurements were performed on MK-NaOH geopolymers, as shown in Figure D.3. Reflectance coefficient of the interface between paste and HIPS container was monitored with time. One major issue with the dataset is the absolute lack of repeatability of any sort in the data. Another issue stems from the increase in s-wave reflectance coefficient between 0.5-1.0 hours, and the subsequent decrease of the reflectance coefficient. Hardening of binder leads to more and more s-waves entering the sample from HIPS container. Therefore, the reflectance coefficient should decrease throughout. In some cases, an abrupt increase in s-wave reflectance coefficient is reported, but this phenomenon is associated with debonding of paste from the HIPS container [24]. If the paste had debonded, then subsequent decrease in reflectance coefficient would not have been observed.

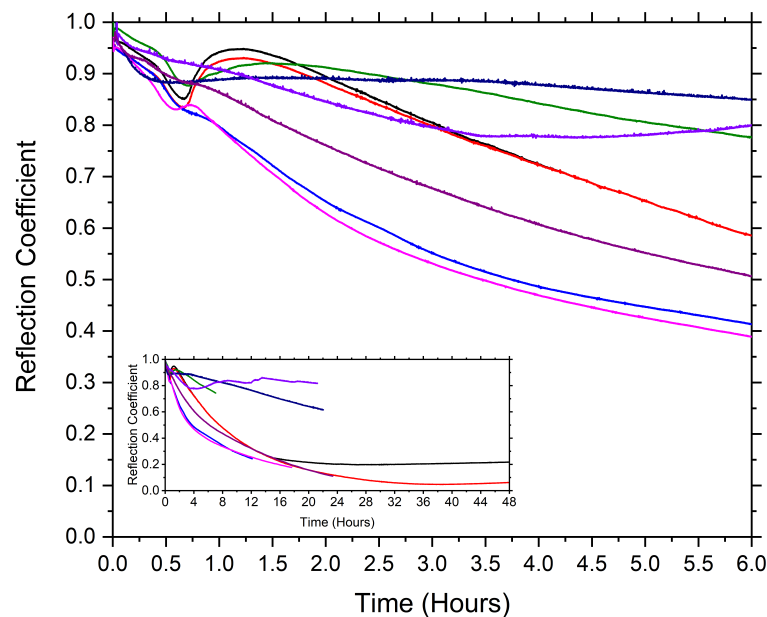


Figure D.3: s-wave UWR measurements of MK-NaOH geopolymer at 22°C

The probable reason behind this observation is hypothesized as follows. MK-NaOH geopolymers consist of dissolution of precursor, followed by growth through polycondensation reactions. Dissolution consumes water, while polycondensation releases

water [29], and this has been proved by separate studies using EPR [54] and NMR spectroscopy [29]. It is believed that this release of water probably interrupts the interface between the HIPS and geopolymer paste, and therefore, the UWR data collection is disturbed. As dissolution predominates at early age, the UWR data appears to be repeatable till  $\approx 0.5$ h but as polycondensation processes start dominating, the signal gets disturbed. Interestingly, water release was observable by NMR spectroscopy after 30-60 minutes from mixing for metakaolin-sodium hydroxide geopolymers [29]. This observation strengthens the hypothesis of water release being the disruptive phenomenon in UWR measurements.

Further proof behind the hypothesis is obtained by UWR measurements carried out with the s-wave transducer placed on the side of the HIPS container (shown in Figure D.4). A slight decrease in reflectance coefficient is observed till 30 minutes, following which no changes are observed at the interface. This shows that there is no contact with between the HIPS and the paste interface. When the transducer is placed at the bottom of the HIPS container, gravity can still ensure some transmission of ultrasonic waves into the sample, in the event that the interface is disturbed by water release. However, with the side interface, there is no chance of such gravity assisting in re-bonding of the paste-HIPS buffer interface. Therefore, debonding is observed. Further proof can also be drawn by placing two s-wave transducers on the same HIPS container for measuring two simultaneous UWR measurements on geopolymer paste. It is expected that the two locations will have different curves since the influence of water release on the interface between paste and HIPS is not going to be a spatially homogeneous process.

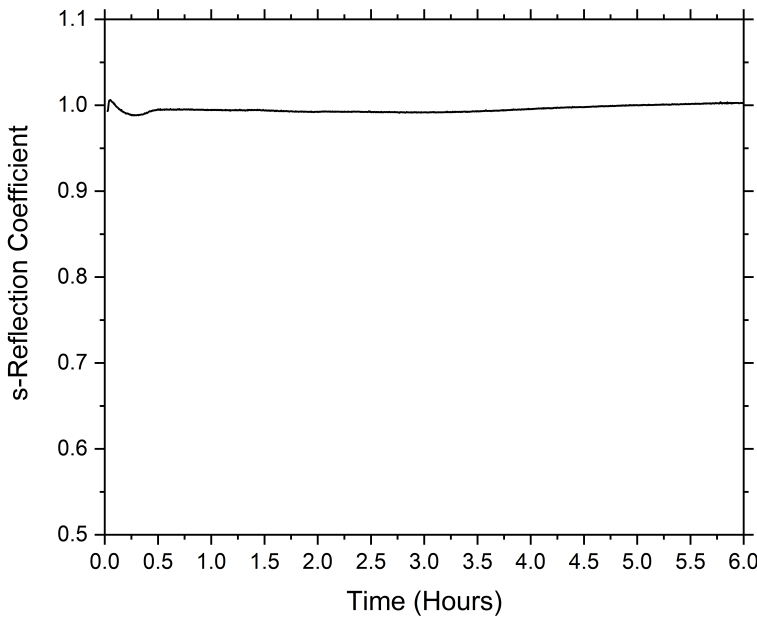


Figure D.4: s-wave UWR measurement of MK-NaOH geopolymer at the HIPS-geopolymer paste side interface, instead of the bottom measurements as shown earlier in Figures D.1 and D.3

Despite this explanation, questions maybe raised to as to how were UWR measurements carried out on the metakaolin geopolymers as reported by Chen et al [86]. The metakaolin geopolymer used had excessive soluble silica in the mix, which has been observed to slow down growth [38]. Experimentally, rate of heat release attributed to polycondensation is also observed to be very low (shown in Figure 4.3). Therefore, the rate of water release through polycondensation is expected to be very low (assuming that the rate of heat release is representative of polycondensation rate), owing to which the paste-HIPS interface is undisturbed. Consequently, no issues are observed during UWR measurements of high silica metakaolin geopolymers.

## Appendix E

### Research Output

The following presentations and publications were based on the work presented in this thesis. Two journal articles are being written, based on the work presented in Chapters 4 and 6.

- D. Sarbapalli and P. Mondal, “Effect of TiO<sub>2</sub> and ZnO nanopowders in metakaolin-sodium hydroxide geopolymers”, *Proceedings of 41st ICACC, Ceramic Engineering and Science Proceedings*, 38(3), 251-262, 2018
- S. Puligilla, D. Sarbapalli, and P. Mondal, “Effect of nucleation seeds in alkali-activated binders”, *International Conference on Advances in Construction Materials and Systems* (RILEM-ICACMS), Chennai, India, 2017
- D. Sarbapalli, X. Chen, L. Struble, and P. Mondal, “Salicylic acid-methanol extraction of aluminosilicate gel” (Manuscript under preparation)
- D. Sarbapalli, X. Chen, L. Struble and P. Mondal, ”Salicylic acid-methanol extraction of aluminosilicate gel”, *8th Advances in Cement-Based Materials*, ACerS, Atlanta, June 2017. (Oral presentation, delivered by P. Mondal)
- D. Sarbapalli, S. Puligilla and P. Mondal, “Nucleation seeding in alkali-activated binders”, at *7th Advances in Cement-Based Materials*, ACerS, Evanston, July 2016. (Poster presentation, presented by D. Sarbapalli)
- S. Puligilla, D. Sarbapalli and P. Mondal, “The effects of nano particle addition on the reaction mechanism of alkali activated fly ash-slag binders”, *American Concrete Institute (ACI) Convention*, Philadelphia, October 2016. (Oral Presentation, delivered by P. Mondal)

## References

- [1] John L Provis, Ana Fernández-Jiménez, Elie Kamseu, Cristina Leonelli, and Angel Palomo. Binder Chemistry–Low-Calcium Alkali-Activated Materials. In *Alkali Activated Materials*, pages 93–123. Springer, 2014.
- [2] John L Provis, Peter Duxson, Elena Kavalerova, Pavel V Krivenko, Zhihua Pan, Francisca Puertas, and Jannie SJ van Deventer. Historical aspects and overview. In *Alkali activated materials*, pages 11–57. Springer, 2014.
- [3] Pierre-Claude Aitcin. Cements of yesterday and today: concrete of tomorrow. *Cement and Concrete research*, 30(9):1349–1359, 2000.
- [4] P. Kumar Mehta and Paulo J M Monteiro. *Concrete: microstructure, properties, and materials*. 2006.
- [5] Donald Macphee and Ines Garcia-Lodeiro. Activation of aluminosilicates-some chemical considerations. In *Proceedings of Slag Valorisation Symposium*, pages 51–61, 2011.
- [6] Peter Duxson, John L Provis, Grant C Lukey, and Jannie SJ Van Deventer. The role of inorganic polymer technology in the development of ‘green concrete’. *Cement and Concrete Research*, 37(12):1590–1597, 2007.
- [7] John L Provis and Susan A Bernal. Geopolymers and related alkali-activated materials. *Annual Review of Materials Research*, 44:299–327, 2014.
- [8] Peter Duxson, Ana Fernández-Jiménez, John L Provis, Grant C Lukey, Angel Palomo, and Jannie SJ van Deventer. Geopolymer technology: the current state of the art. *Journal of materials science*, 42(9):2917–2933, 2007.

- [9] John L Provis. Geopolymers and other alkali activated materials: why, how, and what? *Materials and Structures*, 47(1-2):11–25, 2014.
- [10] John L Provis, Angel Palomo, and Caijun Shi. Advances in understanding alkali-activated materials. *Cement and Concrete Research*, 78:110–125, 2015.
- [11] Sravanthi Puligilla. *Understanding the role of Calcium on the reaction mechanism of geopolymer cements through addition of nucleation seeds*. PhD thesis, University of Illinois at Urbana Champaign, 2017.
- [12] Catherine A Rees, John L Provis, Grant C Lukey, and Jannie SJ van Deventer. The mechanism of geopolymer gel formation investigated through seeded nucleation. *Colloids and Surfaces A: Physicochemical and Engineering Aspects*, 318(1-3):97–105, 2008.
- [13] Ailar Hajimohammadi, John L Provis, and Jannie SJ Van Deventer. Time-resolved and spatially-resolved infrared spectroscopic observation of seeded nucleation controlling geopolymer gel formation. *Journal of colloid and interface science*, 357(2):384–392, 2011.
- [14] Jeffrey J Thomas, Hamlin M Jennings, and Jeffrey J Chen. Influence of nucleation seeding on the hydration mechanisms of tricalcium silicate and cement. *The Journal of Physical Chemistry C*, 113(11):4327–4334, 2009.
- [15] H Rahier, JF Denayer, and B Van Mele. Low-temperature synthesized aluminosilicate glasses: Part iv. modulated dsc study on the effect of particle size of metakaolinite on the production of inorganic polymer glasses. *Journal of Materials Science*, 38(14):3131–3136, 2003.
- [16] JL Provis and JSJ Van Deventer. Geopolymerisation kinetics. 2. reaction kinetic modelling. *Chemical Engineering Science*, 62(9):2318–2329, 2007.

- [17] JL Provis, SL Yong, and P Duxson. Nanostructure/microstructure of metakaolin geopolymers. In *Geopolymers*, pages 72–88. Elsevier, 2009.
- [18] Amal Jayapalan, Bo Lee, Sarah Fredrich, and Kimberly Kurtis. Influence of additions of anatase TiO<sub>2</sub> nanoparticles on early-age properties of cement-based materials. *Transportation Research Record: Journal of the Transportation Research Board*, (2141):41–46, 2010.
- [19] Peter Duxson, SethW Mallicoat, Grant Lukey, Waltraud Kriven, Jannie SJ van Deventer, et al. Microstructural Characterisation of Metakaolin-Based Geopolymers. *Advances in Ceramic Matrix Composites X, Volume 165*, pages 71–85, 2005.
- [20] Peter Duxson, John L Provis, Grant C Lukey, Seth W Mallicoat, Waltraud M Kriven, and Jannie SJ Van Deventer. Understanding the relationship between geopolymer composition, microstructure and mechanical properties. *Colloids and Surfaces A: Physicochemical and Engineering Aspects*, 269(1-3):47–58, 2005.
- [21] Pre De Silva, K Sagoe-Crenstil, and Vute Sirivivatnanon. Kinetics of geopolymerization: role of Al<sub>2</sub>O<sub>3</sub> and SiO<sub>2</sub>. *Cement and Concrete Research*, 37(4):512–518, 2007.
- [22] D Dimas, I Giannopoulou, and D Panias. Polymerization in sodium silicate solutions: a fundamental process in geopolymerization technology. *Journal of materials science*, 44(14):3719–3730, 2009.
- [23] Joseph Davidovits. Geopolymer cement. *A review*. *Geopolymer Institute, Technical papers*, 21:1–11, 2013.
- [24] Sravanthi Puligilla and Paramita Mondal. Role of slag in microstructural development and hardening of fly ash-slag geopolymer. *Cement and Concrete Research*, 43:70–80, 2013.

- [25] CK Yip and JSJ Van Deventer. Microanalysis of calcium silicate hydrate gel formed within a geopolymeric binder. *Journal of Materials Science*, 38(18):3851–3860, 2003.
- [26] Sravanthi Puligilla and Paramita Mondal. Co-existence of aluminosilicate and calcium silicate gel characterized through selective dissolution and FTIR spectral subtraction. *Cement and Concrete Research*, 70:39–49, 2015.
- [27] John L Provis. Introduction and scope. In *Alkali Activated Materials*, pages 1–9. Springer, 2014.
- [28] Xu Chen, Andre Sutrisno, Lingyang Zhu, and Leslie J Struble. Setting and nanostructural evolution of metakaolin geopolymers. *Journal of the American Ceramic Society*, 100(5):2285–2295, 2017.
- [29] L Weng and K Sagoe-Crentsil. Dissolution processes, hydrolysis and condensation reactions during geopolymer synthesis: Part I—Low Si/Al ratio systems. *Journal of Materials Science*, 42(9):2997–3006, 2007.
- [30] Della M Roy. Alkali-activated cements opportunities and challenges. *Cement and Concrete Research*, 29(2):249–254, 1999.
- [31] J. Davidovits. Mineral polymers and methods of making them, September 14 1982. US Patent 4,349,386.
- [32] H Rahier, B Van Mele, M Biesemans, J Wastiels, and X Wu. Low-temperature synthesized aluminosilicate glasses: Part i. low-temperature reaction stoichiometry and structure of a model compound. *Journal of Materials Science*, 31(1):71–79, 1996.
- [33] H Rahier, B VanMele, J Wastiels, et al. Low-temperature synthesized aluminosilicate glasses: Part ii. rheological transformations during low-temperature cure and high-temperature properties of a model-compound. *Journal of Materials Science*, 31(1):80–85, 1996.

- [34] H Rahier, W Simons, B Van Mele, and M Biesemans. Low-temperature synthesized aluminosilicate glasses: Part iii. influence of the composition of the silicate solution on production, structure and properties. *Journal of Materials Science*, 32(9):2237–2247, 1997.
- [35] Ralph K Iler. *The chemistry of silica: solubility, polymerization, colloid and surface properties, and biochemistry*. Wiley-Interscience, 1979.
- [36] Richard G Jones and Union internationale de chimie pure et appliquée. Polymer Division. *Compendium of Polymer Terminology and Nomenclature: IUPAC Recommendations, 2008*. Royal Society of Chemistry Cambridge, 2009.
- [37] E Lippmaa, M Mägi, A Samoson, M Tarmak, and G Engelhardt. Investigation of the structure of zeolites by solid-state high-resolution silicon-29 NMR spectroscopy. *Journal of the American Chemical Society*, 103(17):4992–4996, 1981.
- [38] Gillian Harvey and Lesley S Dent Glasser. Structure and properties of aluminosilicate solutions and gels. ACS Publications, 1989.
- [39] Lesley S Dent Glasser and Eric E Lachowski. Silicate species in solution. Part 1. Experimental observations. *Journal of the Chemical Society, Dalton Transactions*, (3):393–398, 1980.
- [40] John L Provis, Peter Duxson, Grant C Lukey, Frances Separovic, Waltraud M Kriven, and Jannie SJ Van Deventer. Modeling speciation in highly concentrated alkaline silicate solutions. *Industrial & engineering chemistry research*, 44(23):8899–8908, 2005.
- [41] T Antonić, A Čižmek, and B Subotić. Dissolution of amorphous aluminosilicate zeolite precursors in alkaline solutions. Part 2.—Mechanism of the dissolution. *Journal of the Chemical Society, Faraday Transactions*, 90(13):1973–1977, 1994.
- [42] Michael W Grutzeck and Darryl D Siemer. Zeolites synthesized from class F fly ash and

sodium aluminate slurry. *Journal of the American Ceramic Society*, 80(9):2449–2453, 1997.

- [43] Ana Fernández-Jiménez, A Palomo, and M Criado. Microstructure development of alkali-activated fly ash cement: a descriptive model. *Cement and concrete research*, 35(6):1204–1209, 2005.
- [44] P Duxson, GC Lukey, F Separovic, and JSJ Van Deventer. Effect of alkali cations on aluminum incorporation in geopolymeric gels. *Industrial & Engineering Chemistry Research*, 44(4):832–839, 2005.
- [45] Ailar Hajimohammadi and Jannie SJ van Deventer. Dissolution behaviour of source materials for synthesis of geopolymer binders: a kinetic approach. *International Journal of Mineral Processing*, 153:80–86, 2016.
- [46] Thomas W Swaddle. Silicate complexes of aluminum (III) in aqueous systems. *Coordination Chemistry Reviews*, 219:665–686, 2001.
- [47] Peter Duxson, John L Provis, Grant C Lukey, Frances Separovic, and Jannie SJ van Deventer.  $^{29}\text{Si}$  nmr study of structural ordering in aluminosilicate geopolymer gels. *Langmuir*, 21(7):3028–3036, 2005.
- [48] J Faimon. Oscillatory silicon and aluminum aqueous concentrations during experimental aluminosilicate weathering. *Geochimica et cosmochimica acta*, 60(15):2901–2907, 1996.
- [49] John L Provis and Jannie SJ van Deventer. Geopolymerisation kinetics. 1. In situ energy-dispersive X-ray diffractometry. *Chemical Engineering Science*, 62(9):2309–2317, 2007.
- [50] Zuhua Zhang, Hao Wang, John L Provis, Frank Bullen, Andrew Reid, and Yingcan Zhu. Quantitative kinetic and structural analysis of geopolymers. Part 1. The activation of metakaolin with sodium hydroxide. *Thermochimica acta*, 539:23–33, 2012.

- [51] Zuhua Zhang, John L Provis, Hao Wang, Frank Bullen, and Andrew Reid. Quantitative kinetic and structural analysis of geopolymers. Part 2. Thermodynamics of sodium silicate activation of metakaolin. *Thermochimica acta*, 565:163–171, 2013.
- [52] ML Granizo, MT Blanco-Varela, and A Palomo. Influence of the starting kaolin on alkali-activated materials based on metakaolin. study of the reaction parameters by isothermal conduction calorimetry. *Journal of materials science*, 35(24):6309–6315, 2000.
- [53] ML Granizo and MT Blanco. Alkaline activation of metakaolin an isothermal conduction calorimetry study. *Journal of thermal analysis and calorimetry*, 52(3):957–965, 1998.
- [54] Prune Steins, Arnaud Poulesquen, Olivier Diat, and Fabien Frizon. Structural evolution during geopolymerization from an early age to consolidated material. *Langmuir*, 28(22):8502–8510, 2012.
- [55] SA Jefferis and A Sheikh Bahai. Investigation of syneresis in silicate-aluminate grouts. *Geotechnique*, 45(1):131–140, 1995.
- [56] Michael R North and Thomas W Swaddle. Kinetics of silicate exchange in alkaline aluminosilicate solutions. *Inorganic chemistry*, 39(12):2661–2665, 2000.
- [57] Luqian Weng, Kwesi Sagoe-Crentsil, Trevor Brown, and Shenhua Song. Effects of aluminates on the formation of geopolymers. *Materials Science and Engineering: B*, 117(2):163–168, 2005.
- [58] Ailar Hajimohammadi, John L Provis, and Jannie SJ Van Deventer. Effect of alumina release rate on the mechanism of geopolymer gel formation. *Chemistry of Materials*, 22(18):5199–5208, 2010.
- [59] Ailar Hajimohammadi, John L Provis, and Jannie SJ van Deventer. The effect of silica

availability on the mechanism of geopolymserisation. *Cement and Concrete Research*, 41(3):210–216, 2011.

- [60] Luc Nicoleau. The acceleration of cement hydration by seeding: influence of the cement mineralogy. *ZKG international*, 1:40–49, 2013.
- [61] Feraidon F Ataie, Maria CG Juenger, Sarah C Taylor-Lange, and Kyle A Riding. Comparison of the retarding mechanisms of zinc oxide and sucrose on cement hydration and interactions with supplementary cementitious materials. *Cement and Concrete Research*, 72:128–136, 2015.
- [62] Ryan O’Hayre. *Materials Kinetics Fundamentals*. John Wiley & Sons, 2015.
- [63] Taijiro Sato and Fatoumata Diallo. Seeding effect of nano-CaCO<sub>3</sub> on the hydration of tricalcium silicate. *Transportation Research Record: Journal of the Transportation Research Board*, (2141):61–67, 2010.
- [64] Jeffrey J Thomas. A new approach to modeling the nucleation and growth kinetics of tricalcium silicate hydration. *Journal of the American Ceramic Society*, 90(10):3282–3288, 2007.
- [65] Gerrit Land and Dietmar Stephan. Controlling cement hydration with nanoparticles. *Cement and Concrete Composites*, 57:64–67, 2015.
- [66] Rouhollah Alizadeh, Laila Raki, Jon M Makar, James J Beaudoin, and Igor Moudrakovski. Hydration of tricalcium silicate in the presence of synthetic calcium-silicate-hydrate. *Journal of Materials Chemistry*, 19(42):7937–7946, 2009.
- [67] Shiho Kawashima, Pengkun Hou, David J Corr, and Surendra P Shah. Modification of cement-based materials with nanoparticles. *Cement and Concrete Composites*, 36:8–15, 2013.

- [68] Matthieu Horgnies, Lingjie Fei, Raquel Arroyo, Jeffrey J Chen, and Ellis M Gartner. The effects of seeding C<sub>3</sub>S pastes with afwillite. *Cement and Concrete Research*, 89:145–157, 2016.
- [69] Brian C Smith. *Fundamentals of Fourier transform infrared spectroscopy*. CRC press, 2011.
- [70] Joseph I Goldstein, Dale E Newbury, Joseph R Michael, Nicholas WM Ritchie, John Henry J Scott, and David C Joy. *Scanning electron microscopy and X-ray microanalysis*. Springer, 2003.
- [71] Denny A Jones. *Principles and prevention of corrosion*. Macmillan, 1992.
- [72] Mija H Hubler, Jeffrey J Thomas, and Hamlin M Jennings. Influence of nucleation seeding on the hydration kinetics and compressive strength of alkali activated slag paste. *Cement and Concrete Research*, 41(8):842–846, 2011.
- [73] Shao-Dong Wang and Karen L Scrivener. Hydration products of alkali activated slag cement. *Cement and Concrete Research*, 25(3):561–571, 1995.
- [74] Bi-Zeng Zhan, Mary Anne White, Michael Lumsden, Jason Mueller-Neuhaus, Katherine N Robertson, T Stanley Cameron, and Michael Ghargouri. Control of particle size and surface properties of crystals of NaX zeolite. *Chemistry of Materials*, 14(9):3636–3642, 2002.
- [75] Mahdi Ansari, Abdolreza Aroujalian, Ahmadreza Raisi, Bahram Dabir, and Mahdi Fathizadeh. Preparation and characterization of nano-NaX zeolite by microwave assisted hydrothermal method. *Advanced Powder Technology*, 25(2):722–727, 2014.
- [76] Xu Zhang, Dingxing Tang, and Guojun Jiang. Synthesis of zeolite NaA at room temperature: The effect of synthesis parameters on crystal size and its size distribution. *Advanced Powder Technology*, 24(3):689–696, 2013.

- [77] Jacek Klinowski, Subramaniam Ramdas, John M Thomas, Colin A Fyfe, and J Steven Hartman. A re-examination of Si, Al ordering in zeolites NaX and NaY. *Journal of the Chemical Society, Faraday Transactions 2: Molecular and Chemical Physics*, 78(7):1025–1050, 1982.
- [78] Caustic soda solution NaOH 50%, Jul 2016. [Online; accessed 18. Feb. 2018].
- [79] Piyush Chaunsali. *Early-age hydration and volume change of calcium sulfoaluminate cement-based binders*. PhD thesis, University of Illinois at Urbana-Champaign, 2015.
- [80] BD Cullity and SR Stock. *Elements of X-ray Diffraction*. Pearson Education Limited, 3rd ed. edition, 2001.
- [81] M Król, J Minkiewicz, and W Mozgawa. IR spectroscopy studies of zeolites in geopolymeric materials derived from kaolinite. *Journal of Molecular Structure*, 1126:200–206, 2016.
- [82] Kenneth JD MacKenzie and Mark E Smith. *Multinuclear solid-state nuclear magnetic resonance of inorganic materials*, volume 6. Elsevier, 2002.
- [83] Seymour Lowell, Joan E Shields, Martin A Thomas, and Matthias Thommes. *Characterization of porous solids and powders: surface area, pore size and density*, volume 16. Springer Science & Business Media, 2012.
- [84] John L Provis, Grant C Lukey, and Jannie SJ van Deventer. Do geopolymers actually contain nanocrystalline zeolites? a reexamination of existing results. *Chemistry of Materials*, 17(12):3075–3085, 2005.
- [85] Maria Luz Granizo, Santiago Alonso, Maria T Blanco-Varela, and Angel Palomo. Alkaline activation of metakaolin: effect of calcium hydroxide in the products of reaction. *Journal of the American Ceramic Society*, 85(1):225–231, 2002.
- [86] Xu Chen, Amr Meawad, and Leslie J Struble. Method to stop geopolymer reaction. *Journal of the American Ceramic Society*, 97(10):3270–3275, 2014.

- [87] David Feng, Hui Tan, and JSJ Van Deventer. Ultrasound enhanced geopolymersation. *Journal of materials science*, 39(2):571–580, 2004.
- [88] Ankica Čimek, Ljepša Komunjer, Boris Subotić, Marija Široki, and Sanda Rončević. Kinetics of zeolite dissolution: Part 1. Dissolution of zeolite A in hot sodium hydroxide. *Zeolites*, 11(3):258–264, 1991.
- [89] Ankica Čizmek, Ljepša Komunjer, Boris Subotić, Marija Široki, and Sanda Rončević. Kinetics of zeolite dissolution. Part 2. Dissolution of zeolite X in hot sodium hydroxide solutions. *Zeolites*, 11(8):810–815, 1991.
- [90] Brant Walkley, Rackel San Nicolas, Marc-Antoine Sani, John D Gehman, Jannie SJ van Deventer, and John L Provis. Phase evolution of  $\text{Na}_2\text{O}-\text{Al}_2\text{O}_3-\text{SiO}_2-\text{H}_2\text{O}$  gels in synthetic aluminosilicate binders. *Dalton Transactions*, 45(13):5521–5535, 2016.
- [91] Prannoy Suraneni and Robert J Flatt. Micro-reactors for studying mineral reactivity. *Proceedings of the 14th EMABM*, 2013.
- [92] Prannoy Suraneni and Robert J Flatt. Micro-reactors to study alite hydration. *Journal of the American Ceramic Society*, 98(5):1634–1641, 2015.
- [93] Brant Walkley, Rackel San Nicolas, Marc-Antoine Sani, John D Gehman, Jannie SJ van Deventer, and John L Provis. Synthesis of stoichiometrically controlled reactive aluminosilicate and calcium-aluminosilicate powders. *Powder Technology*, 297:17–33, 2016.
- [94] Paul Wencil Brown, James Pommersheim, and Geoffrey Frohnsdorff. A kinetic model for the hydration of tricalcium silicate. *Cement and Concrete Research*, 15(1):35–41, 1985.
- [95] Jeffrey J Thomas and Hamlin M Jennings. Effects of d<sub>2</sub>O and mixing on the early hydration kinetics of tricalcium silicate. *Chemistry of materials*, 11(7):1907–1914, 1999.

- [96] Alessio Damasceni, Luigi Dei, Emiliano Fratini, Francesca Ridi, Sow-Hsin Chen, and Piero Baglioni. A novel approach based on differential scanning calorimetry applied to the study of tricalcium silicate hydration kinetics. *The Journal of Physical Chemistry B*, 106(44):11572–11578, 2002.
- [97] Shashank Bishnoi and Karen L Scrivener. Studying nucleation and growth kinetics of alite hydration using  $\mu$ ic. *Cement and Concrete Research*, 39(10):849–860, 2009.
- [98] Peter Hewlett. *Lea's chemistry of cement and concrete*. Elsevier, 2003.
- [99] Robert L Day and Bryan K Marsh. Measurement of porosity in blended cement pastes. *Cement and Concrete Research*, 18(1):63–73, 1988.
- [100] Karen L Scrivener. The use of backscattered electron microscopy and image analysis to study the porosity of cement paste. *MRS Online Proceedings Library Archive*, 137, 1988.
- [101] N Buenfeld. Permeability of normal and lightweight mortars-discussion. *Magazine of Concrete Research*, 38(134):51–52, 1986.
- [102] Brian K Marsh, Robert L Day, and DG Bonner. Pore structure characteristics affecting the permeability of cement paste containing fly ash. *Cement and Concrete Research*, 15(6):1027–1038, 1985.
- [103] Sidney Diamond. Mercury porosimetry: an inappropriate method for the measurement of pore size distributions in cement-based materials. *Cement and concrete research*, 30(10):1517–1525, 2000.
- [104] Bhagwanjee Jha and Devendra Narain Singh. *Basics of Zeolites*, pages 5–31. Springer Singapore, Singapore, 2016.
- [105] C230/C230M-14 Standard Specification for Flow Table for Use in Tests of Hydraulic Cement, 2014.

- [106] M Luz Granizo, María Teresa Blanco-Varela, and Sagrario Martínez-Ramírez. Alkali activation of metakaolins: parameters affecting mechanical, structural and microstructural properties. *Journal of Materials Science*, 42(9):2934–2943, 2007.
- [107] Daniel LY Kong, Jay G Sanjayan, and Kwesi Sagoe-Crentsil. Comparative performance of geopolymers made with metakaolin and fly ash after exposure to elevated temperatures. *Cement and Concrete Research*, 37(12):1583–1589, 2007.
- [108] A Palomo, Maria Teresa Blanco-Varela, ML Granizo, F Puertas, T Vazquez, and MW Grutzeck. Chemical stability of cementitious materials based on metakaolin. *Cement and Concrete Research*, 29(7):997–1004, 1999.
- [109] Robert W Thompson. Recent advances in the understanding of zeolite synthesis. In *Synthesis*, pages 1–33. Springer, 1998.
- [110] Juliusz Warzywoda and Robert W Thompson. Synthesis of zeolite a in the na/k system and the effect of seeding. *Zeolites*, 11(6):577–582, 1991.
- [111] Robert D Edelman, Dinesh V Kudalkar, Tjendrawani Ong, Juliusz Warzywoda, and Robert W Thompson. Crystallization phenomena in seeded zeolite syntheses. *Zeolites*, 9(6):496–502, 1989.
- [112] Sylvie Gonthier, Leszek Gora, Ipek Güray, and Robert W Thompson. Further comments on the role of autocatalytic nucleation in hydrothermal zeolite syntheses. *Zeolites*, 13(6):414–418, 1993.
- [113] Robert W Thompson and Alan Dyer. Nucleation of zeolite naa crystals in hydrothermal systems. *Zeolites*, 5(5):302–308, 1985.
- [114] George T Kerr. Chemistry of crystalline aluminosilicates. I. Factors affecting the formation of zeolite A. *The Journal of Physical Chemistry*, 70(4):1047–1050, 1966.

- [115] Colin S Cundy and Paul A Cox. The hydrothermal synthesis of zeolites: history and development from the earliest days to the present time. *Chemical Reviews*, 103(3):663–702, 2003.
- [116] WA Klemm and J Skalny. Selective dissolution of clinker minerals and its applications. *XII Conference on silicate Industry and silicate science, Technical Report, Budapest*, pages 77–32, 1977.
- [117] Paul Stutzman. Guide for X-Ray Powder Diffraction Analysis of Portland Cement and Clinker. Technical report, Building and Fire Research Laboratory, National Institute of Standards and Technology, Gaithersburg, 1996.
- [118] L Hjorth and K-G Lauren. Belite in Portland cement. *Cement and Concrete Research*, 1(1):27–40, 1971.
- [119] Karen Luke and Fredrik P Glasser. Selective dissolution of hydrated blast furnace slag cements. *Cement and Concrete Research*, 17(2):273–282, 1987.
- [120] A Palomo, A Fernández-Jiménez, G Kovalchuk, LM Ordoñez, and MC Naranjo. OPC-fly ash cementitious systems: study of gel binders produced during alkaline hydration. *Journal of Materials Science*, 42(9):2958–2966, 2007.
- [121] Ines García-Lodeiro, A Fernández-Jiménez, M Teresa Blanco, and Angel Palomo. FTIR study of the sol-gel synthesis of cementitious gels: C-S-H and N-A-S-H. *Journal of Sol-Gel Science and Technology*, 45(1):63–72, 2008.
- [122] Xu Chen, Andre Sutrisno, and Leslie J Struble. Effects of calcium on setting mechanism of metakaolin-based geopolymers. *Journal of the American Ceramic Society*, 101(2):957–968, 2018.
- [123] N Shigemoto, S Sugiyama, H Hayashi, and K Miyaura. Characterization of Na-X, Na-A, and coal fly ash zeolites and their amorphous precursors by IR, MAS NMR and XPS. *Journal of materials science*, 30(22):5777–5783, 1995.

- [124] Catherine Anne Rees. *Mechanisms and kinetics of gel formation in geopolymers*. PhD thesis, University of Melbourne, 2007.
- [125] Ryan L Hartman and H Scott Fogler. Understanding the dissolution of zeolites. *Langmuir*, 23(10):5477–5484, 2007.
- [126] William M Haynes. *CRC handbook of chemistry and physics*. CRC press, 2014.
- [127] Avelino Corma. Inorganic solid acids and their use in acid-catalyzed hydrocarbon reactions. *Chemical Reviews*, 95(3):559–614, 1995.
- [128] RA Van Santen. Theory of brønsted acidity in zeolites. In *Studies in Surface Science and Catalysis*, volume 85, pages 273–294. Elsevier, 1994.
- [129] Marek Sierka, Uwe Eichler, Jerzy Datka, and Joachim Sauer. Heterogeneity of brønsted acidic sites in faujasite type zeolites due to aluminum content and framework structure. *The Journal of Physical Chemistry B*, 102(33):6397–6404, 1998.
- [130] George T Kerr. Chemistry of crystalline aluminosilicates. v. preparation of aluminum-deficient faujasites. *The Journal of Physical Chemistry*, 72(7):2594–2596, 1968.
- [131] Minas R Apelian, Anthony S Fung, Gordon J Kennedy, and Thomas F Degnan. Dealumination of zeolite  $\beta$  via dicarboxylic acid treatment. *The Journal of Physical Chemistry*, 100(41):16577–16583, 1996.
- [132] Jerzy Datka, Waclaw Kolidziejksi, Jacek Klinowski, and Bogdan Sulikowski. Dealumination of zeolite Y by H 4 EDTA. *Catalysis letters*, 19(2-3):159–165, 1993.
- [133] Fernando Secco and Marcella Venturini. Mechanism of complex formation. reaction between aluminum and salicylate ions. *Inorganic Chemistry*, 14(8):1978–1981, 1975.
- [134] Fabien Thomas, Armand Masion, Jean Yves Bottero, James Rouiller, Frederic Montigny, and Francine Genevrier. Aluminum (III) speciation with hydroxy

carboxylic acids. Aluminum-27 NMR study. *Environmental science & technology*, 27(12):2511–2516, 1993.

[135] Prannoy Suraneni. *Micro-reactors to study hydration of cementitious materials*. PhD thesis, 2015.

[136] Topas 4.2 technical reference, 2009.

[137] Brian H Toby. R factors in Rietveld analysis: how good is good enough? *Powder diffraction*, 21(1):67–70, 2006.

[138] T Öztürk, J Rapoport, JS Popovics, and SP Shah. Monitoring the setting and hardening of cement-based materials with ultrasound. *Concrete Science and Engineering*, 1(2):83–91, 1999.

[139] Prannoy Suraneni, Sravanthi Puligilla, Eric H Kim, Xu Chen, Leslie J Struble, and Paramita Mondal. Monitoring setting of geopolymers. *Advances in Civil Engineering Materials*, 3(1):177–192, 2014.

[140] Sravanthi Puligilla and Paramita Mondal. Microstructural changes responsible for hardening of fly ash–slag geopolymers studied through infrared spectroscopy. In *Geopolymer Binder Systems*. ASTM International, 2013.

[141] Chul-Woo Chung. *Ultrasonic wave reflection measurements on stiffening and setting of cement paste*. PhD thesis, University of Illinois at Urbana-Champaign, 2010.